

# Constraining tensor-to-scalar ratio based on VLBI observations: PGWs induced-incoherence approach

F. S. Arani,<sup>a,b,c</sup> M. Bagheri Harouni<sup>a,d</sup> Brahim Lamine<sup>b,c,1</sup> Alain Blanchard<sup>b,c</sup>

<sup>a</sup>Department of Physics, University of Isfahan, Hezar Jerib Str., Isfahan 81746-73441, Iran

<sup>b</sup>Université de Toulouse, UPS-OMP, IRAP, F-31400 Toulouse, France

<sup>c</sup>CNRS, IRAP, 14 avenue Edouard Belin, F-31400 Toulouse, France

<sup>d</sup>Quantum Optics Group, Department of Physics, University of Isfahan, Hezar Jerib Str., Isfahan 81746-73441, Iran

E-mail: [fshojaei@irap.omp.eu](mailto:fshojaei@irap.omp.eu), [m.bagheri@sci.ui.ac.ir](mailto:m.bagheri@sci.ui.ac.ir), [brahim.lamine@irap.omp.eu](mailto:brahim.lamine@irap.omp.eu)

**Abstract.** In this study, we show that the background of primordial gravitational waves (PGWs) predicted by the inflationary scenario induce a decrease of the spatial coherence length of an electromagnetic field propagating over cosmological distances, leading the van Citter-Zernike correlations to eventually be unobservable, an affect called as blurring. Since this spatial correlation is actually observed in VLBI measurements of distant quasars, it imposes a constraint on the level of the primordial gravitational waves background. In this paper, we precisely evaluate this blurring effect by considering the primordial gravitational waves background to be in the so-called two-mode squeezed state, which is the standard quantum state predicted by the simplest scenario of inflation. We then exploit a sample of compact radio quasars located at redshift range  $0.46 \leq z \leq 2.73$  observed by very long baseline interferometry (VLBI) means. These quasars constitute a standard ruler and the angular size-distance  $\theta - z$  relation is determined thanks to the measurement of their spatial coherence. These spatial coherence observations set an upper limit on the squeezing parameters of the PGWs background, which turns into an upper limit for the tensor-to-scalar ratio  $r_{k_0}$ . One finds  $r_{k_0} < 10^{-7}$ , five orders of magnitude better than present constraints on this parameter with the CMB. This result is nevertheless compatible with the possible detection of a cosmic background by the pulsar timing array measurement. Further issues and caveats that potentially affect the results are reviewed. In particular, the possible effect of quantum-to-classical transition of PGWs is discussed. Ultimately, we promote the idea of using high-precision VLBI measurement of angular size-redshift of distant sources as a new possible way of constraining the background of primordial tensor perturbations.

---

<sup>1</sup>Corresponding author.

---

## Contents

<b>1</b>	<b>Introduction</b>	<b>1</b>
<b>2</b>	<b>PGWs in expansionary Universe</b>	<b>3</b>
2.1	Expansionary Universe	3
2.2	PGWs amplification in expanding Universe	4
2.3	Quantum normalization condition (QNC)	8
<b>3</b>	<b>Quantum mechanical EM-GWs interaction</b>	<b>9</b>
3.1	Hamiltonian formalism for EM-GWs interaction in flat spacetime	9
3.2	Heisenberg equation of the EM field in the presence of GWs	11
<b>4</b>	<b>Loss of spatial coherence induced by two-mode squeezed PGWs</b>	<b>14</b>
4.1	Spatial correlations in the presence of GWs	14
4.1.1	Configuration of a VLBI-type system	14
4.1.2	Equal-time first-order degree of coherence $g^{(1)}(\mathbf{x}_1, t; \mathbf{x}_2, t)$	15
4.2	First-order degree of coherence in the presence of PGWs in two-mode squeezed state	17
4.2.1	Contribution of vacuum fluctuations of GWs	19
4.2.2	Contribution of gravitons in TS state	19
4.3	Characterization of different length-scales $\xi^{\text{vac}}(z)$ , $\delta^{\text{vac}}(z)$ and $\xi^{\text{ts}}(z)$	20
<b>5</b>	<b>Implication of PGWs background on VLBI measurements</b>	<b>21</b>
5.1	van Citter-Zernike theorem and Very Long Baseline Interferometry (VLBI)	22
5.2	The visibility $\mathcal{V}(\mathbf{x}_P, t)$ in the presence of GWs and definition of incoherence parameter $\alpha^{\text{ts}}(z)$	23
5.3	VLBI measurement of the angular size of standard ruler	24
5.4	VLBI constraint on tensor-to-scalar ratio $r_{k_0}$	26
<b>6</b>	<b>Further discussion and results</b>	<b>28</b>
6.1	Implications for the slow-roll framework	28
6.2	Comparison between different quantum states of PGWs and possible quantum-to-classical transition issue	30
<b>7</b>	<b>Summary and conclusion</b>	<b>30</b>
<b>8</b>	<b>Supplementary materials</b>	<b>31</b>
<b>A</b>	<b>PGWs spectrum and related parameters</b>	<b>31</b>
A.1	Increase parameters $\zeta_E, \zeta_2, \zeta_s, \zeta_1$	31
A.2	Spectral amplitude of PGWs	32
A.3	Characteristic wave numbers $K_E, K_H, K_2, K_s$ and $K_1$	33

<b>B Preliminaries for evaluation of <math>g_{\text{ts}}^{(1)}(\mathbf{x}_1, t, \mathbf{x}_2, t)</math></b>	<b>34</b>
B.1 Evaluation of the integral $\int d^3\mathbf{K} \kappa_\gamma^2(\mathbf{K}, \mathbf{k})$	34
B.2 $Kd_{12} \ll 1$ approximation	35
B.3 Expression of the time of flight $t$ versus redshift $z$	36
<b>C Mutual intensity of a planar source in the presence of PGWs</b>	<b>36</b>
<b>D Loss of spatial correlations induced by GWs in vacuum, thermal and squeezed state</b>	<b>37</b>
D.1 Loss of spatial correlations induced by quantum fluctuations of GWs	37
D.2 Loss of spatial correlations induced by thermal gravitons	38
D.3 Loss of spatial correlations induced by squeezed state	40

---

## 1 Introduction

Interferometric methods have found vast applications in testing gravity either at the classical or quantum level. Starting from the famous Michelson-Morley interferometer to rule out the motion through “aether”, light interferometry is now routinely used as a crucial technique to detect the tiniest effects of gravitational waves (GWs) with an incredible precision [1–5]. Whether these ripples in the spacetime obey quantum mechanical rules at a fundamental scale, say the Planck scale, is an open question and we lack any direct observational evidence in favor of that [6, 7].

It is believed that space and time, when viewed at Planck scales, form a foam-like structure due to quantum fluctuations of the vacuum metric tensor of spacetime [8–10]. Searching for Planck-scale quantum features of spacetime is an old quest, and many interferometric schemes based on the phase properties of electromagnetic (EM) radiation of distant objects have been proposed to inquire it [11–16]. For instance, the phase interferometric approach early introduced in [12] inspects the Planck-scale physics through the spacetime foam-induced *phase incoherence* of light emitted from distant objects. In fact, it has been perceived that accumulation of tiny phase-incoherence during the long journey of light through the quantum fluctuations of the vacuum spacetime leads to loss of the phase of radiation at large distances. This approach was elaborated in [13] to rule out, or put stringent limits, on some Planck-scale phenomenological models, by evidence of the diffraction pattern from the Hubble Space Telescope observations of SN 1994D at  $z = 5.34$ .

However, further studies [17] declared that such effects “are far below what is required in this approach to shed light on the foaminess of spacetime”. Moreover, it turned out that “propagation of spatial correlations is governed by the van Citter-Zernike theorem [18], and spatial correlations are immune to any underlying fuzzy Planck scale”, hence the Planck scale still remains inaccessible to interferometer detection with present technology [19]. Albeit, this result leaves the room for quantum gravitational effects of length-scales much larger than the Planck length.

One important example is the relic background of quantum tensor perturbations naturally generated by the pumping engine of inflation. At the heart of cosmology, the inflationary scenario predicts that quantum fluctuations of the gravitational field present at the very early Universe have evolved and been amplified during the successive expansion of the Universe, and constitute a stochastic background of primordial gravitational waves (PGWs) today [20–32]. Due to its specific generating mechanism, PGWs spectrum span a full range of frequencies,

corresponding to wavelengths much larger than the Planck scale. Thereupon, the quest for PGWs has made one of the main targets of today’s and upcoming GWs detectors in different frequency bands: LIGO [33], Advanced LIGO [34, 35], VIRGO [36, 37], GEO [38, 39], AIGO [40, 41], LCGT [42], ET [43, 44] aiming at the frequency range ( $10^2 - 10^3$ ) Hz; the space interferometers, such as the future LISA [45, 46] which is sensitive in the frequency range ( $10^{-4} - 10^{-1}$ ) Hz, BBO [47–49] and DECIGO [50, 51] both sensitive in frequency range (0.1–10) Hz; and the pulsar timing arrays, including PPTA [52–54] and the planned SKA [55] working in frequency window ( $10^{-9} - 10^{-6}$ ) Hz. Besides, there are potential proposals able to detect the very-high-frequency part of PGWs, among which are the waveguide detector [56–59], the proposed gaussian maser beam detector around GHz [60–62], and the 100 MHz detector [63]. Moreover, the very low frequency portion of PGWs contribute to the anisotropy and polarization of cosmic microwave background (CMB) [64–70], yielding a magnetic-type polarization of CMB as a distinguished signal of PGWs, which would possibly be sensed by means of WMAP [71–75], Planck [76, 77], liteBIRD [78], the ground-based ACTPol [79] and the proposed CMBpol [80]. Detection of PGWs would not only confirm the inflationary scenario but also validate the quantum description of gravity at scales much larger than the Planck length.

In the present study, we introduce a new schema to search for the unique imprints of the PGWs on the spatial correlations of EM emission from furthest objects, and show how high-precision measurements of the angular size  $\theta$  of distant objects using Very Long Baseline Interferometers (VLBI) can exert constraints on PGWs. The VLBI imaging technique takes advantage of the largest possible baselines (from several meters to thousands of kilometers) to precisely determine the location and fine structure of astronomical sources including Active Galactic Nuclei (AGNs) [81–85]. In a typical VLBI experiment, the incoming radiation of a distant source is collected by two or more spatially-separated telescopes (see Fig. 2). Existence of spatial correlations throughout the projected baseline of the interferometer leads to the appearance of interference pattern (non-vanishing visibility), which is used to determine the geometrical properties of the object, such as its angular diameter.

Noticeably, VLBI imaging has found great attention in constraining cosmology. For instance, the Event Horizon Telescope (EHT) which is a VLBI array imaging supermassive black holes (SMBHs) on event horizon scales, allows tests of deviation from general relativity by performing high precision measurements of the Kerr metric [86, 87]. Moreover, the Megamaser Cosmology Project (MCP) which is based on the VLBI sub-milliarcsecond angular mapping of compact objects, has provided an independent laboratory to constrain the Hubble constant,  $H_0$ , in parallel to other surveys such as CMB [88], likewise putting updated constraints on the mass of SMBHs [89]. In particular, capability of VLBI method in accurate measurement of the angular size-redshift  $\theta - z$  of intermediate-luminosity radio quasars has led to specify AGNs as astrophysical standard rulers with intrinsic size  $\ell_m \sim 11.03$  pc, that can be used to constrain cosmological parameters [90–92]. Recently, capability of the stellar interferometry as a potential tool to detect GWs in the lower frequency range ( $10^{-6} - 10^{-4}$ ) Hz is investigated [93]. However, to our best knowledge, VLBI measurements of the angular size-redshift has not yet been used to constrain the background of PGWs. Here, we promote the idea of employing stellar interferometric methods to constrain the underlying gravitational background of PGWs. We show how VLBI measurements of the angular size-redshift may put new constraint on the inflationary parameters, in particular the tensor-to-scalar ratio  $r_{k_0}$ .

It is worth mentioning that, in the literature there are numerous schema that focus on graviton-induced *decoherence* (GID) of light [94, 95] or particles [96, 97]. As a matter of fact,

due to negligibly small coupling strength between gravity and radiation or matter fields, one usually needs a huge interaction time to observe the GID effect, provided that the system is completely isolated from other environmental effects that may lead to decoherence. In contrast, spatial correlations of a source are known to be immune to the typical environment induced-decoherence. In particular, van Citter-Zernike theorem implies that correlation length of initially spatial-incoherent sources grow with distance [18]. However, we show that PGWs background acts as a competitive mechanism that tends to reduce spatial correlation length. Hence, sources with cosmological distances that have had enough time to interact with the underlying gravitational background seem proper candidates to explore the underlying quantum gravitational effects.

The paper is organized as follows. Sec. 2 provides a brief introduction about the expansionary Universe, the generation of two-mode squeezed PGWs from vacuum fluctuations and definition of the related quantities of PGWs. In Sec. 3, a self-contained investigation of the EM-GWs interaction at quantum level is included, followed by solving the Heisenberg equations of motion of the EM field. This will help us investigate the two-point correlation function of the EM radiation in Sec. 4, where the loss of correlations induced by two-mode squeezed PGWs is evaluated and characteristic length-scales are defined. Sec. 5 is devoted to definition of the visibility and the coherence criteria that can be established with the help of current VLBI measurements. Eventually, we assess the coherence criteria based on the  $\theta - z$  measurement of a set of compact radio-quasars, which are suggested as standard rulers, and try to constrain the underlying PGWs background based on that. We in particular demonstrate interesting constraint on the tensor-to-scalar ratio  $r_{k_0}$ . In Sec. 6, further possible topics and caveats that can be addressed within the present method are discussed, followed by a summary and conclusion in Sec. 7. A complete supplementary material containing the details of the derivation of the equations and its subtleties is provided in Apps. A-D. Throughout the paper, we explicitly write  $c$ ,  $\hbar$  and  $G$  in all equations.

## 2 PGWs in expansionary Universe

### 2.1 Expansionary Universe

The spatially flat expanding Universe is often described by the Friedmann–Lemaître–Robertson–Walker (FLRW) metric and assumes a power-law scale factor  $a(\eta) \propto \eta^\alpha$ , where  $\eta$  is the conformal time. Each successive expanding stage is specified with a different index  $\alpha$ . The whole expansion history can be described by [98]

$$a(\eta) = \begin{cases} \ell_0 |\eta|^{1+\beta} & , \quad -\infty \leq \eta \leq \eta_1 \\ a_z (\eta - \eta_p)^{1+\beta_s} & , \quad \eta_1 \leq \eta \leq \eta_s \\ a_e (\eta - \eta_e) & , \quad \eta_s \leq \eta \leq \eta_2 \\ a_m (\eta - \eta_m)^2 & , \quad \eta_2 \leq \eta \leq \eta_E \\ \ell_H |\eta - \eta_a|^{-\gamma} & , \quad \eta_E \leq \eta \leq \eta_H \end{cases} \quad (2.1)$$

where  $\eta_H$  is the conformal time today and  $a(\eta)$  has the dimensionality of length [98, 99].

Usually the inflation index  $\beta$  is related to the scalar spectral index of primordial perturbations according to  $n_s = 2\beta + 5$  [23, 100, 101]. Basically,  $n_s$  is a parameter introduced under the assumption that scalar perturbation spectrum obeys a power-law behaviour near the pivot scale  $k_0$ , with  $n_s = 1$  referred to Harrison-Zeldovich spectrum. The *Planck2018*

release favor  $n_s \simeq 0.9649 \pm 0.0044$  [102], corresponding to  $\beta \simeq -2.018 \pm 0.0022$ . However, the exact relation between  $\beta$  and  $n_s$  depends crucially on the specific inflationary potential through the (first order) slow-roll parameter  $\epsilon_V$  (see Sec. 6.1). In this study, we consider  $\beta$  as a free parameter of the model. However, for the sake of illustration we mostly take  $\beta = -2.0$ .

The parameter  $\beta_s$  describes the expansion during the reheating stage starting right after the end of inflation, and may be related to the equation of state (EoS) parameter during the reheating stage,  $w_{reh}$ , and to inflationary model parameters. In the literature, usually  $\beta_s = 1$  is chosen, which may correspond to a quadratic inflation potential with EoS parameter  $w_{reh} = 0$  [99, 103]. As discussed in App. (A.3),  $\beta_s$  affects only the high-frequency part of the PGWs spectrum, which will leave a negligible effect on incoherence of the EM field that we study in this paper. Hence we mostly adopt the value  $\beta_s = 1$  in our investigations.

The parameter  $\gamma$  determines the late expansion of the Universe governed by dark energy  $\Lambda$ . Throughout later numerical investigations, we take  $\gamma = 1$  which would correspond to a pure de Sitter acceleration phase [104]. On the other hand, the present scale factor is conveniently chosen  $a(\eta_H) = \ell_H$ , so that the condition  $|\eta_H - \eta_a| = 1$  turns out [104]. The constant  $\ell_H$  is determined by  $\ell_H = \gamma/H_0$  as a result of Eq. (2.1). Here,  $H_0 = 67.4 \text{ km s}^{-1} \text{ Mpc}^{-1}$  is the present Hubble constant [105].

Considering  $\beta$  and  $\beta_s$  as free parameters, there remain 12 constants in Eq. (2.1), 8 of which are reduced by the continuity of  $a(\eta)$  and its derivative at four jointing points  $\eta_1, \eta_s, \eta_2$  and  $\eta_E$ , resulting in 4 independent parameters. One usually expresses these 4 parameters in terms of increase of the scale factor during various stages, namely,  $\zeta_1 \equiv a(\eta_s)/a(\eta_1)$ ,  $\zeta_s \equiv a(\eta_2)/a(\eta_s)$ ,  $\zeta_2 \equiv a(\eta_E)/a(\eta_2)$ , and  $\zeta_E \equiv a(\eta_H)/a(\eta_E)$ . For the accelerating stage in the simple  $\Lambda$ CDM model, one has  $\zeta_E = 1 + z_E \sim 1.33$ , where  $z_E$  is the redshift when the accelerating stage begins. For the matter-dominated stage one has  $\zeta_2 = (1 + z_{eq})\zeta_E^{-1} \sim 2547$  with  $z_{eq} = 3387$  [105] being the redshift at matter-radiation equality (see App. A.3). The increase of scale factor during the reheating and radiation-dominated stages, namely  $\zeta_1$  and  $\zeta_s$ , generally depend on the reheating temperature  $T_{reh}$  at which the radiation stage begins (see Appendix A for details). Big Bang Nucleosynthesis (BBN) and the energy scale at the end of inflation put lower and upper bounds on  $T_{reh}$  as  $T_{reh} \geq 10 \text{ MeV}$  and  $T_{reh} \leq 10^{16} \text{ GeV}$ , respectively [106]. However, the CMB data modify the lower bound on the reheating temperature  $T_{reh} \geq 6 \times 10^3 \text{ GeV}$  [106], and gravitinos generation has given the upper bound  $T_{reh} \leq 10^7 \text{ GeV}$  [107]. As discussed in App. A.3,  $T_{reh}$  does not play significant role in incoherence of the EM field, since it only changes the high-frequency part of the PGWs spectrum (see Fig. 1). However, the value of  $T_{reh}$  could affect the range of other parameters, including  $\beta, \beta_s, \zeta_1$ , when considering specific inflationary scenarios (see [108] for example). In this paper, we mainly adopt  $T_{reh} = 10^8 \text{ GeV}$  for the sake of illustration. The specific  $T_{reh}$ -dependence of  $\zeta_s$  is determined by Eq. (A.3), though  $\zeta_1$  is usually regarded as a free parameter. So far, four parameters ( $\beta, \beta_s, T_{reh}, \zeta_1$ ) determine the expansion of the Universe. The introduction of primordial perturbations adds extra degrees of freedom, namely the scalar and tensor power spectrum,  $A_{s,T}$ , and the scalar and tensor spectral indices,  $n_{s,T}$ , at some pivot scale  $k_0$ , among which we only treat  $A_T$  (or equivalently the tensor-to-scalar ratio  $r_{k_0}$ ) as free parameter and use the current constraints on  $A_s$  and  $n_s$  made by *Planck2018* observations (see Sec. 2.3).

## 2.2 PGWs amplification in expanding Universe

Inflationary-generated PGWs originate from tensor perturbations of the FLRW metric during the inflationary era. Started from vacuum state, they have been amplified during the



course of expansion of the Universe. The super-adiabatic amplification leads vacuum tensor perturbations to evolve into two-mode squeezed (TS) state with enormously large number of gravitons [109, 110]. Dynamics of the tensorial perturbations is governed by the perturbed Hilbert-Einstein action in FLRW Universe [111]

$$S[h_{ij}] \simeq \frac{M_{\text{Pl}}^2 c^2}{8\hbar} \int d\eta d^3\mathbf{x} a^2(\eta) \left( h^{ij'} h'_{ij} - \partial^k h^{ij} \partial_k h_{ij} \right), \quad (2.2)$$

where  $M_{\text{Pl}}^2 = \hbar c / (8\pi G)$  is the reduced Planck mass. Here, ' denotes derivative with respect to conformal time  $\eta$ , and spatial indices are raised and lowered with the help of the unit tensor  $\delta_{ij}$ , assuming the metric signature  $(-, +, +, +)$ . To decouple time and spatial variables, it is convenient to introduce the Fourier transform of the metric perturbation  $h_{ij}(\mathbf{x}, \eta)$  by

$$h_{ij}(\mathbf{x}, \eta) = \frac{\sqrt{2\hbar}}{M_{\text{Pl}} c} \sum_{\gamma=+, \times} \int_{\mathbf{K} \in \mathbb{R}^3} \frac{d^3\mathbf{K}}{(2\pi)^{3/2}} e_{ij}^\gamma(\hat{\mathbf{K}}) h_{\mathbf{K}}^\gamma(\eta) e^{i\mathbf{k}\cdot\mathbf{x}}, \quad (2.3)$$

where  $\mathbf{K} = K\hat{\mathbf{K}}$  denotes the comoving wave vector,  $e_{ij}^\gamma(\hat{\mathbf{K}})$  stands for the polarization tensor and  $\gamma = +, \times$  represents the polarization state of tensor perturbations. Since the tensor field  $h_{ij}(\mathbf{x}, \eta)$  is real, one has  $e_{ij}^\gamma(\hat{\mathbf{K}}) = e_{ij}^{\gamma*}(\hat{\mathbf{K}})$  and  $h_{-\mathbf{K}}^\gamma(\eta) = h_{\mathbf{K}}^{\gamma*}(\eta)$ . This property implies that, in the Fourier space, all degrees of freedom are not independent, since the metric perturbation  $h_{ij}(\mathbf{x}, \eta)$  is a real quantity while  $h_{\mathbf{K}}^\gamma(\eta)$  is complex. Note that, throughout the paper, we shall use upper-case letters  $K = (\Omega_K/c, \mathbf{K})$  to represent the four-momentum of GWs, while lower-case letters  $k = (\omega/c, \mathbf{k})$  will be used to represent the four-momentum of the EM field. The polarization tensor  $e_{ij}^\gamma(\hat{\mathbf{K}})$  fulfills the following conditions

$$K^i e_{ij}^\gamma(\hat{\mathbf{K}}) = 0 \quad , \quad e_{ii}^\gamma(\hat{\mathbf{K}}) = 0 \quad \text{and} \quad e_{ij}^{\gamma*}(\hat{\mathbf{K}}) e_{ij}'(\hat{\mathbf{K}}) = 2\delta_{\gamma\gamma'}. \quad (2.4)$$

Additionally, the two independent polarization states  $\gamma = +, \times$  can be expressed in terms of two unit vectors  $(\hat{\mathbf{n}}, \hat{\mathbf{m}})$  orthogonal to the propagation direction  $\hat{\mathbf{K}}$  and to each other. In terms of the Euler's angles  $(\Theta_K, \Phi_K)$ , one may specify  $(\hat{\mathbf{K}}, \hat{\mathbf{n}}, \hat{\mathbf{m}})$  by

$$\hat{\mathbf{K}} = \begin{pmatrix} \sin \Theta_K \cos \Phi_K \\ \sin \Theta_K \sin \Phi_K \\ \cos \Theta_K \end{pmatrix}, \quad \hat{\mathbf{n}} = \begin{pmatrix} \cos \Theta_K \cos \Phi_K \\ \cos \Theta_K \sin \Phi_K \\ -\sin \Theta_K \end{pmatrix}, \quad \hat{\mathbf{m}} = \begin{pmatrix} -\sin \Phi_K \\ \cos \Phi_K \\ 0 \end{pmatrix}, \quad (2.5)$$

and the polarization tensors are written as [32]

$$\begin{cases} \hat{e}_{ij}^+[\hat{\mathbf{K}}] = \hat{n}_i \hat{n}_j - \hat{m}_i \hat{m}_j, \\ \hat{e}_{ij}^\times[\hat{\mathbf{K}}] = \hat{m}_i \hat{n}_j + \hat{n}_i \hat{m}_j, \end{cases} \quad (2.6)$$

which satisfy Eq. (2.4). Inserting the field expansion Eq. (2.3) into the action Eq. (2.2) and taking variation with respect to the Fourier field amplitude  $h_{\mathbf{K}}^\gamma(\eta)$  determines dynamics of the tensor perturbations inside the expanding Universe according to

$$h_{\mathbf{K}}^{\gamma''}(\eta) + 2\mathcal{H}(\eta) h_{\mathbf{K}}^{\gamma'}(\eta) + K^2 h_{\mathbf{K}}^\gamma(\eta) = 0, \quad (2.7)$$

where  $\mathcal{H}(\eta) \equiv \frac{a'(\eta)}{a(\eta)}$  is the comoving Hubble parameter. Eq. (2.7) can be solved for a given  $a(\eta)$ . This procedure has been extensively studied in the literature to obtain analytical expression for the tensor perturbations (for instance see [112]). Specially, the solution of

Eq. (2.7) in two asymptotic regimes are interesting:  $K \gg 2\pi\mathcal{H}$  and  $K \ll 2\pi\mathcal{H}$ , corresponding to short-wavelength (sub-Hubble) and long-wavelength (super-Hubble) regimes, respectively. In the former case, the amplitude of the wave experiences a decay as  $h_{\mathbf{K}}^\gamma(\eta) \propto 1/a(\eta)$ , while in the latter case, the amplitude stays constant during the whole long-wavelength regime [22]. However, here we are specially interested in quantization of tensor perturbations during the long-wavelength regime. For our discussion, we chose the formalism and notation that is previously introduced for quantization of scalar perturbations in [109, 110]. Following the same procedure that is presented in details in [110], one ends up with the following Hamiltonian governing the evolution of tensor perturbations

$$\hat{H} = \hbar \sum_{\gamma=+, \times} \int_{\mathbf{K} \in \mathfrak{R}^{3+}} d^3\mathbf{K} \left[ K(\hat{b}_{\mathbf{K},\gamma} \hat{b}_{\mathbf{K},\gamma}^\dagger + \hat{b}_{-\mathbf{K},\gamma} \hat{b}_{-\mathbf{K},\gamma}^\dagger) - i \frac{a'}{a} (\hat{b}_{\mathbf{K},\gamma} \hat{b}_{-\mathbf{K},\gamma} - \hat{b}_{\mathbf{K},\gamma}^\dagger \hat{b}_{-\mathbf{K},\gamma}^\dagger) \right]. \quad (2.8)$$

Here,  $(\hat{b}_{\mathbf{K},\gamma}, \hat{b}_{\mathbf{K},\gamma}^\dagger)$  denote the bosonic operators of mode  $(\mathbf{K}, \gamma)$  of tensor perturbations. The advantage of using half Fourier space is that opposite momenta in  $\mathbf{K} \in \mathfrak{R}^{3+}$  are independent and their corresponding operators commute. Hamiltonian Eq. (2.8) is the generator of the two-mode squeezed states as previously investigated in the context of quantum optics [113, 114]. Thus, interaction with the pumping field of the expanding Universe leads the vacuum of tensor perturbations get energy and evolve into two-mode squeezed state [22, 109, 110]. For our later use in subsequent sections, here we adopt the Schrödinger picture. Thus, the quantum field operator of tensor perturbations at all times is determined by its initial value, i.e.,

$$\begin{aligned} \hat{h}_{ij}(\mathbf{x}, \eta_{\text{ini}}) = \mathcal{C} \sum_{\gamma=+, \times} \int_{\mathbf{K} \in \mathfrak{R}^{3+}} \frac{d^3\mathbf{K}}{(2\pi)^{3/2}} \frac{e_{ij}^\gamma(\hat{\mathbf{K}})}{\sqrt{2\Omega_K}} \left\{ \left( \hat{b}_{\mathbf{K},\gamma}(\eta_{\text{ini}}) + \hat{b}_{-\mathbf{K},\gamma}^\dagger(\eta_{\text{ini}}) \right) e^{i\mathbf{K}\cdot\mathbf{x}} \right. \\ \left. + \left( \hat{b}_{\mathbf{K},\gamma}^\dagger(\eta_{\text{ini}}) + \hat{b}_{-\mathbf{K},\gamma}(\eta_{\text{ini}}) \right) e^{-i\mathbf{K}\cdot\mathbf{x}} \right\}, \end{aligned} \quad (2.9)$$

where  $\mathcal{C} = \sqrt{16\pi c \ell_{\text{Pl}}}$ , and  $\eta_{\text{ini}}$  denotes some initial time during the inflationary epoch, before the initiation of super-adiabatic amplification. The quantum state of inflationary-generated PGWs at a given conformal time  $\eta$ , governed by the Hamiltonian Eq. (2.8), turns out to be given by

$$|\text{TS}(\eta)\rangle \equiv \prod_{\mathbf{K} \in \mathfrak{R}^{3+}} \hat{S}_{\mathbf{K}}(\zeta_K(\eta)) \hat{R}_{\mathbf{K}}(\theta_K(\eta)) |0_{\mathbf{K}}, 0_{-\mathbf{K}}\rangle, \quad (2.10)$$

which is basically a two-mode squeezed state (hereafter denoted by TS state). Here, due to the fact that the opposite momenta are not independent degrees of freedom, the multiplication is taken over half Fourier space  $\mathbf{K} \in \mathfrak{R}^{3+}$ . The two-mode squeezing operator  $\hat{S}_{\mathbf{K}}(\zeta_K(\eta))$  and the rotation operator  $\hat{R}_{\mathbf{K}}(\theta_K(\eta))$  are defined by (see [110] for details)

$$\begin{aligned} \hat{S}_{\mathbf{K}}(\zeta_K(\eta)) &\equiv \exp \left[ \zeta_K^*(\eta) \hat{b}_{-\mathbf{K}} \hat{b}_{\mathbf{K}} - \zeta_K(\eta) \hat{b}_{\mathbf{K}}^\dagger \hat{b}_{-\mathbf{K}}^\dagger \right], \\ \hat{R}_{\mathbf{K}}(\theta_K(\eta)) &\equiv \exp \left[ -i\theta_K(\eta) \left( \hat{b}_{\mathbf{K}}^\dagger \hat{b}_{\mathbf{K}} + \hat{b}_{-\mathbf{K}}^\dagger \hat{b}_{-\mathbf{K}} \right) \right], \end{aligned} \quad (2.11)$$

where the squeezing parameter is defined by  $\zeta_K(\eta) \equiv r_K(\eta) e^{2i\phi_K(\eta)}$  with  $(r_K, \phi_K)$  being the squeezing amplitude and angle, respectively, and the rotation angle is defined by  $\theta_K(\eta)$ . Also note that, we shall use the symbol  $r_K$  to represent the squeezing amplitude of the PGWs



mode  $K$ , while the symbol  $r_{k_0}$  is reserved for the tensor-to-scalar ratio at the pivot scale  $k_0$ . The evolution of the squeezing and rotation parameters are determined by [110]

$$\begin{aligned}\frac{dr_K}{d\eta} &= \frac{a'}{a} \cos(2\phi_K), \\ \frac{d\phi_K}{d\eta} &= -K - \frac{a'}{a} \coth(2r_K) \sin(2\phi_K), \\ \frac{d\theta_K}{d\eta} &= -K - \frac{a'}{a} \tanh(2r_K) \sin(2\phi_K).\end{aligned}\tag{2.12}$$

Note that, equation of motion for the squeezing parameters  $(r_K(\eta), \phi_K(\eta))$  are decoupled from the rotation angle  $\theta_K(\eta)$ , and the latter can be determined once  $(r_K(\eta), \phi_K(\eta))$  are determined. Indeed, one may see from Eq. (2.12) that  $\hat{R}_{\mathbf{K}}(\theta_K(\eta))|0_{\mathbf{K}}, 0_{-\mathbf{K}}\rangle = |0_{\mathbf{K}}, 0_{-\mathbf{K}}\rangle$ , which means that the variable  $\theta_K$  is not involved in the dynamics of perturbations, as it should by invariance under rotation.

Equivalently, the three parameters  $(r_K, \phi_K, \theta_K)$  may be represented by two complex variables  $(u_K(\eta), v_K(\eta))$  defined by [109, 110]

$$\begin{aligned}u_K(\eta) &\equiv e^{i\theta_K(\eta)} \cosh r_K(\eta), \\ v_K(\eta) &\equiv e^{-i\theta_K(\eta)+2i\phi_K(\eta)} \sinh r_K(\eta),\end{aligned}\tag{2.13}$$

which satisfy the normalization  $|u_K(\eta)|^2 - |v_K(\eta)|^2 = 1$ . The use of  $(u_K(\eta), v_K(\eta))$  is most favoured in the literature, specially when investigating quantum features of cosmological perturbations [115]. In the present study, we use these two sets of parameters interchangeably.

In the following, we consider the approximate solution to the system of equations (2.12) in the super-Hubble regime  $K \ll 2\pi\mathcal{H}$ , when the mode  $K$  has been amplified sufficiently and the squeezing amplitude is high so that  $r_K \gg 1$ . The equations (2.12) in the long wavelength regime  $K \ll 2\pi\mathcal{H}$  can be approximated by

$$\begin{aligned}r'_K(\eta) &= \frac{a'}{a} \cos(2\phi_K), \\ \phi'_K(\eta) &= -\frac{a'}{a} \coth(2r_K) \sin(2\phi_K)\end{aligned}\tag{2.14}$$

For super-Hubble scales, the squeezing amplitude  $r_K$  is very large, so that  $\coth(2r_K) \rightarrow 1$ . Hence, the equation for  $\phi_K$  yields the following solution

$$\phi'_K(\eta) = -\frac{a'}{a} \sin(2\phi_K) \quad \Rightarrow \quad \tan(\phi_K) \propto \frac{1}{a^2(\eta)},\tag{2.15}$$

which implies  $\tan(\phi_K) \rightarrow 0$  during the long-wavelength regime. The squeezing angle  $\phi_K$  tends to either values 0 or  $\pi$ , both resulting in  $\cos(2\phi_K) \rightarrow 1$ . Hence the equation of motion for  $r_K(\eta)$  reduces to  $r'_K(\eta) = a'/a$  with the simple solution  $r_K(\eta) = \ln a(\eta)/a_*(K)$ , where  $a_*(K) \equiv a(\eta_*(K))$  denote the value of the scale factor at the initial moment of horizon-crossing,  $\eta_*(K)$ , when the long-wavelength regime initiates for a given mode  $K$ . The initial value for  $r_K$  is chosen as  $r_K(\eta_*) = 0$ . If one denoted by  $\eta_{**}(K)$  the time when the mode leaves the long-wavelength regime and re-enters the Hubble horizon and  $K \geq 2\pi\mathcal{H}$ , the final value of the squeezing amplitude is determined by

$$e^{r_K} = \frac{a_{**}(K)}{a_*(K)},\tag{2.16}$$

where  $a_{**}(K) = a(\eta_{**}(K))$  denotes the value of scale factor when the mode re-enters the horizon (see [22] for more details). Considering the model of successive expansion of the Universe introduced in Sec. 2.1, one may show that the squeezing factor at present,  $e^{r_K(\eta_H)}$ , is related to the present spectral amplitude  $h(K, \eta_H)$  according to  $e^{r_K(\eta_H)} = \frac{1}{8\sqrt{\pi}\gamma} \frac{\ell_H}{\ell_{\text{Pl}}} \left(\frac{K_H}{K}\right) h(K, \eta_H)$ , and is given by (see App. A.2)

$$e^{r_K(\eta_H)} = \frac{1}{8\sqrt{\pi}} \frac{\ell_H}{\ell_{\text{Pl}}} \left(\frac{K_H}{K}\right) \begin{cases} A \left(\frac{K}{K_H}\right)^{2+\beta} & , \quad K \leq K_E \\ A \left(\frac{K}{K_H}\right)^{\beta-1} \frac{1}{(1+z_E)^3} & , \quad K_E \leq K \leq K_H \\ A \left(\frac{K}{K_H}\right)^{\beta} \frac{1}{(1+z_E)^3} & , \quad K_H \leq K \leq K_2 \\ A \left(\frac{K}{K_H}\right)^{1+\beta} \left(\frac{K_H}{K_2}\right) \frac{1}{(1+z_E)^3} & , \quad K_2 \leq K \leq K_s \\ A \left(\frac{K}{K_H}\right)^{1+\beta-\beta_s} \left(\frac{K_s}{K_H}\right) \left(\frac{K_H}{K_2}\right) \frac{1}{(1+z_E)^3} & , \quad K_s \leq K \leq K_1 \end{cases} \quad (2.17)$$

where the characteristic wave numbers  $K_E, K_H, K_2, K_s$  and  $K_1$  are determined once the increase parameters  $\zeta_1, \zeta_s, \zeta_2$  and  $\zeta_E$  are fixed (see App. A.3). The coefficient  $A$  determines the initial perturbation amplitude that can be assessed by theoretical or observational normalization conditions, as discussed below.

### 2.3 Quantum normalization condition (QNC)

In the CMB literature, it is convenient to express the contribution of tensor perturbations around the pivot scale  $k_0$  in terms of the so-called tensor-to-scalar ratio,  $r_{k_0} \equiv \frac{A_T(k_0)}{A_s(k_0)}$  with  $A_{T,s}(k_0)$  being the tensor and scalar power spectrum at the pivot scale  $k_0$ , respectively. We remind that throughout the paper, the pivot scale is exceptionally denoted by  $k_0$  and the symbol  $r_{k_0}$  is reserved for the tensor-to-scalar ratio, not to be confused with the squeezing amplitude  $r_K$ . We shall take  $k_0 = 0.002 \text{ Mpc}^{-1}$  in our calculations [105]. The perturbation field  $h_{ij}$  at initial moment (that is to say before exiting the horizon during the inflationary era) can be treated as a quantum field in its vacuum state, possessing half energy quanta  $\frac{1}{2}\hbar\Omega_K$  in each mode  $K$ . This assumption imposes a criteria on the initial amplitude  $A$ , called the quantum normalization condition (QNC) [22, 98, 116], which translate into a condition on the tensor-to-scalar ratio  $r_{k_0}$ . As a result of QNC, it can be shown that one ends up with the following theoretical constraint between the previously discussed parameters ( $\beta, \beta_s, T_{\text{reh}}, \zeta_1, r_{k_0}$ ) [98],

$$A = \sqrt{A_s r_{k_0}} \left(\frac{K_H}{k_0}\right)^{\beta} \zeta_E^{\frac{2+\gamma}{\gamma}} = 8\sqrt{\pi} \left(\frac{\ell_{\text{Pl}} H_0}{c}\right) \gamma^{-(2+\beta)} \zeta_1^{\frac{\beta_s-\beta}{1+\beta_s}} \zeta_s^{-\beta} \zeta_2^{\frac{1-\beta}{2}} \zeta_E^{1+\frac{1+\beta}{\gamma}} \quad (2.18)$$

Upper bounds  $A_s \lesssim 2.1 \times 10^{-9}$  and  $r_{k_0} < 0.056$  have been obtained by *Planck2018* using TTTEEE + lowE + lensing + BAO [117]. Taking  $r_{k_0}$  as free parameter, one may convert Eq. (2.18) to express  $\zeta_1$  in terms of the other parameters, namely

$$\zeta_1(\beta, \beta_s, \zeta_s, r_{k_0}) = \left[ \frac{c(A_s(k_0)r_{k_0})^{1/2}}{8\sqrt{\pi}\ell_{\text{Pl}}H_0} \left(\frac{K_H}{k_0}\right)^{\beta} \gamma^{2+\beta} \zeta_s^{\beta} \zeta_2^{\frac{\beta-1}{2}} \zeta_E^{\frac{1-\beta}{\gamma}} \right]^{\frac{1+\beta_s}{\beta_s-\beta}}, \quad (2.19)$$

and the expansionary model Eq. (2.1) is fully described by four independent parameters ( $\beta, \beta_s, T_{\text{reh}}, r_{k_0}$ ). The spectral amplitude  $h(K, \eta_H)$  and the corresponding squeezing factor

$e^{r\kappa(\eta_H)}$  are shown in figure 1 panel (a) and panel (b), respectively, for different values of the parameters  $(\beta, \beta_s, T_{\text{reh}}, r_{k_0})$  (see App. A.2). It can be seen that changing the reheating parameters  $\beta_s$  and  $T_{\text{reh}}$  changes only the high-frequency part of the spectrum, i.e.  $K_s < K < K_1$ , which contain only small amount squeezing, with respect to the ultra-low frequency part. On the other hand, changing  $\beta$  and  $r_{k_0}$  affect almost the whole frequency range of the spectrum.

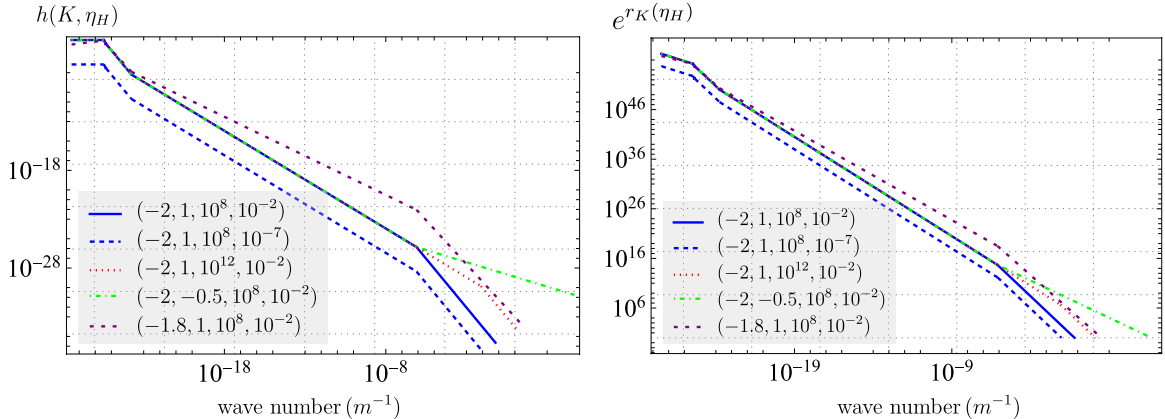


**Figure 1.** Panel (a): today PGWs spectral amplitude  $h(K, \eta_H)$  and panel (b): the corresponding squeezing factor  $e^{r\kappa(\eta_H)}$ , versus the physical wave number  $0.01K_E \leq K \leq K_1$  for different values of the parameters  $(\beta, \beta_s, T_{\text{reh}}/\text{GeV}, r_{k_0})$ .

### 3 Quantum mechanical EM-GWs interaction

After reviewing the generation of PGWs in TS state in expanding Universe, in this section we include a self-contained investigation of EM-GWs interaction at the quantum level, where we derive and solve Heisenberg equation governing a single-mode EM field propagating through a quantum background of GWs. This step helps us investigate the Glauber's correlation functions of the EM field in the presence of such quantum background, in next sections.

#### 3.1 Hamiltonian formalism for EM-GWs interaction in flat spacetime

The imprint of GWs on light is comprehensively studied in the literature, either at classical [32] or quantum level [94, 95, 118, 119]. In the following, we proceed by adopting the formalism presented in [95]. For practical purposes, it seems natural to consider a situation that a single-mode EM field, possessing wave vector  $\mathbf{k}$  and frequency  $\omega_k$ , propagates through the flat Minkowski spacetime and interacts with tensor perturbations  $h_{ij}(\mathbf{x}, t)$ . Quantum mechanical interaction of a continuum of GWs with a single-mode EM field, in the adiabatic approximation where  $\omega_k \ll \Omega_K$ , can be described by the following total Hamiltonian [95]

$$\hat{H}_{\text{tot}} = \hat{H}_{\text{em}}^{(0)} + \hat{H}_{\text{GWs}}^{(0)} + \hat{H}_{\text{int}}(\mathbf{x}, t). \quad (3.1)$$

Here,  $\hat{H}_{\text{em}}^{(0)}$  and  $\hat{H}_{\text{GWs}}^{(0)}$  account for free evolution of each sub-system, according to

$$\begin{aligned} \hat{H}_{\text{em}}^{(0)} &= \hbar\omega_k \hat{a}_{\mathbf{k}}^\dagger \hat{a}_{\mathbf{k}}, \\ \hat{H}_{\text{GWs}}^{(0)} &= \sum_{\gamma=+, \times} \int d^3\mathbf{K} \hbar\Omega_K \hat{b}_{K, \gamma}^\dagger \hat{b}_{K, \gamma}, \end{aligned} \quad (3.2)$$

where  $(\hat{a}_{\mathbf{k}}, \hat{a}_{\mathbf{k}}^\dagger)$  are the ladder operators of the EM field satisfying the usual bosonic commutation relation  $[\hat{a}_{\mathbf{k}}, \hat{a}_{\mathbf{k}'}^\dagger] = \delta^{(3)}(\mathbf{k} - \mathbf{k}')$ . The interaction Hamiltonian is determined by (see [95] for details)

$$\hat{H}_{\text{int}}(\mathbf{x}, t) = -\frac{1}{2}\hbar\omega_k \left( \hat{a}_{\mathbf{k}}^\dagger \hat{a}_{\mathbf{k}} \hat{h}_{ij}(\mathbf{x}, t) \right) k_i k_j. \quad (3.3)$$

which describes the interaction between a single-mode EM field with a generic GWs background. The spatio-temporal dependence of the interaction Hamiltonian stems from the spatio-temporal dependence of GWs field  $\hat{h}_{ij}(\mathbf{x}, t)$ . Quantization of GWs in flat spacetime gives rise to the following expression for the field operator [95]

$$\hat{h}_{ij}(\mathbf{x}, t) = \mathcal{C} \sum_{\gamma=+, \times} \int \frac{d^3\mathbf{K}}{(2\pi)^{3/2}} \frac{e_{ij}^\gamma[\hat{K}]}{\sqrt{2\Omega_K}} \left( \hat{b}_{\mathbf{K}, \gamma} e^{-i(\Omega t - \mathbf{K} \cdot \mathbf{r})} + \hat{b}_{\mathbf{K}, \gamma}^\dagger e^{i(\Omega t - \mathbf{K} \cdot \mathbf{r})} \right), \quad (3.4)$$

where  $\mathcal{C} = \sqrt{16\pi c l_{\text{Pl}}}$  as in Eq. (2.9). The explicit time-dependence in Eq. (3.4) implies that the field operator  $\hat{h}_{ij}(\mathbf{x}, t)$ , as well as the interaction Hamiltonian Eq. (3.3), are basically written in the *Heisenberg picture* where free time evolution of the ladder operators,  $\hat{b}_{\mathbf{K}, \gamma}(t) = \hat{b}_{\mathbf{K}, \gamma} e^{-i\Omega_K t}$  and  $\hat{b}_{\mathbf{K}, \gamma}^\dagger(t) = \hat{b}_{\mathbf{K}, \gamma}^\dagger e^{i\Omega_K t}$ , are explicitly written. The Hamiltonian in the Schrödinger picture is achieved by disregarding the time evolution of the field operators. Substitution of Eq. (3.4) into the interaction Hamiltonian Eq. (3.3) and disregarding time-dependence of the field operators results in the following expression for the interaction Hamiltonian in the *Schrödinger picture*

$$\begin{aligned} \hat{H}_{\text{int}}^{(S)}(\mathbf{x})/\hbar &= -\frac{1}{2} \left( \frac{\hbar\omega_k}{E_{\text{Pl}}} \right) \frac{\sqrt{16\pi c^3}}{(2\pi)^{3/2}} \sum_{\gamma=+, \times} \int d^3\mathbf{K} \frac{F_\gamma(\hat{\mathbf{K}}, \hat{\mathbf{k}})}{\sqrt{2\Omega_K}} \\ &\times \left( \hat{b}_{\mathbf{K}, \gamma} e^{i\mathbf{K} \cdot \mathbf{x}} + \hat{b}_{\mathbf{K}, \gamma}^\dagger e^{-i\mathbf{K} \cdot \mathbf{x}} \right) \hat{a}_{\mathbf{k}}^\dagger \hat{a}_{\mathbf{k}}. \end{aligned} \quad (3.5)$$

Here, we used  $\mathcal{C} = \sqrt{16\pi c l_{\text{Pl}}} = \hbar\sqrt{16\pi c^3}/E_{\text{Pl}}$ . Moreover, the *detector pattern function*  $F_\gamma(\hat{\mathbf{K}}, \hat{\mathbf{k}})$  is defined by

$$F_\gamma(\hat{\mathbf{K}}, \hat{\mathbf{k}}) \equiv e_{ij}^\gamma[\hat{\mathbf{K}}] k_i k_j \quad (3.6)$$

which accounts for geometrical configuration of the EM-GWs system (see Eq. (7.21) of [32] for definition of the detector pattern function). If we denote by  $L$  the physical size of the EM propagation, in case of a small detector where  $KL \ll 1$ , the spatial phase factors  $e^{\pm i\mathbf{K} \cdot \mathbf{x}}$  in Eq. (3.5) are equal to unity and the Hamiltonian reduces to that of [120]. However, these factors become specially important when we consider the EM propagation through cosmological distances hence we keep them in the following. The Hamiltonian Eq. (3.5) describes the interaction between EM and GWs fields through the intensity dependent coupling (proportional to  $\hat{a}_{\mathbf{k}}^\dagger \hat{a}_{\mathbf{k}}$ ) between EM field and GWs, and is reminiscent of the opto-mechanical coupling in cavity opto-mechanics [121]. This analogy turns out to be useful in formulating quantum dynamics of the EM field.

Note that the interaction Hamiltonian (3.5) assumes the flat Minkowski spacetime as the spacetime metric. Let us justify this approximation in our cosmological context. Actually, the EM-GWs interaction occurs in the fabric of FLRW spacetime, and both fields interact with FLRW spacetime in addition to the EM-GWs interaction. For the EM field, the expansion of

the Universe leads to the EM frequency redshift according to  $\omega_k \rightarrow \omega_k/(1+z)$  with  $z$  being the redshift of the source. Moreover, the time of flight of the EM field through cosmological background must be modified, considering the source is located at a given redshift  $z$  (see App. B.3). We will come back to this point in Sec. 5.3 where we consider spatial correlations of a set of radio-quasars located at redshift range  $0.46 \leq z \leq 2.76$ . On the other hand, as it was pointed out in Sec. 2.2, when the modes re-enter the Hubble horizon and the short-wavelength regime starts, the spectral amplitude  $h(K, \eta)$  suffers a decay, as a result of the expansion of the Universe [22, 23, 98]. Thus, the decay of spectral amplitude during the EM-GWs interaction is proportional to the ratio  $\frac{a(\eta_{\text{em}})}{a(\eta_H)}$  with  $a(\eta_{\text{em}})$  and  $a(\eta_H)$  being the scale factor at emission and detection (at the present) times, so that  $\eta_{\text{int}} = \eta_H - \eta_{\text{em}}$  is the EM-GWs interaction duration. Assuming the source is located at redshift  $z$ , by definition one has  $1+z = \frac{a(\eta_H)}{a(\eta_{\text{em}})}$ . Considering the redshift range  $0 \lesssim z \lesssim 10$ , the reduction in the spectral amplitude would be less than  $\frac{a(\eta_{\text{em}})}{a(\eta_H)} = \frac{1}{1+z} \sim 10\%$ , and can be neglected. Consequently, we may proceed by considering the (flat) Minkowski spacetime as the background on which EM and GWs interplay, and eventually enter the effect of Universe expansion on the EM frequency shift as well as on the interaction time (or time of flight) of the EM source. We assume that  $h(K, \eta_H)$  and the corresponding squeezing parameters do not evolve during the interaction time  $\eta_{\text{int}}$ , and the squeezing factor is determined by Eq. (2.17) throughout the EM-GWs interaction.

With the help of Hamiltonian Eq. (3.5), we now proceed to the derivation of the Heisenberg equation of motion for the EM field operators.

### 3.2 Heisenberg equation of the EM field in the presence of GWs

To proceed, we firstly initialize the *time evolution operator* generated by the Hamiltonian Eq. (3.1). When written in the Schrödinger picture, the total Hamiltonian becomes time-independent, which let us write the time evolution operator of the system as

$$\begin{aligned} \hat{U}(\mathbf{x}, t) &= \exp\left(-\frac{i}{\hbar}\hat{H}_{\text{tot}}^{(S)}(\mathbf{x})t\right) \\ &= \exp\left(-\frac{i}{\hbar}[\hat{H}_{\text{em}}^{(0)} + \hat{H}_{\text{GWs}}^{(0)} + \hat{H}_{\text{int}}^{(S)}(\mathbf{x})]t\right) \\ &= e^{-i(\omega_k t)\hat{a}_{\mathbf{k}}^\dagger\hat{a}_{\mathbf{k}} - i\sum_\gamma \int d^3\mathbf{K}(\Omega_{Kt})\hat{b}_K^\dagger\hat{b}_K + \frac{i}{2\pi}\left(\frac{\hbar\omega_k}{E_{\text{Pl}}}\right)\sum_\gamma \int d^3\mathbf{K}\frac{F_\gamma(\hat{\mathbf{K}}, \hat{\mathbf{k}})}{K^{3/2}}(\hat{b}_K e^{i\mathbf{K}\cdot\mathbf{x}} + \hat{b}_K^\dagger e^{-i\mathbf{K}\cdot\mathbf{x}})(\Omega_{Kt})\hat{a}_{\mathbf{k}}^\dagger\hat{a}_{\mathbf{k}}}. \end{aligned} \quad (3.7)$$

In the last line, Eq. (3.2) and Eq. (3.5) are inserted. To break up  $\hat{U}$  into separate exponential factors, we follow the trick introduced in [122] for a single-mode opto-mechanical interaction, and generalize it to the case of continuum of GWs modes with a space-dependent Hamiltonian. We define the unitary operator  $\hat{T}$  as

$$\hat{T} \equiv e^{-\hat{a}_{\mathbf{k}}^\dagger\hat{a}_{\mathbf{k}}\sum_\gamma \int d^3\mathbf{K}\kappa_\gamma(\mathbf{K}, \mathbf{k})\left(\hat{b}_K^\dagger e^{-i\mathbf{K}\cdot\mathbf{x}} - \hat{b}_K e^{i\mathbf{K}\cdot\mathbf{x}}\right)}. \quad (3.8)$$

Here, for the sake of abbreviation we use the notation  $K \equiv (\mathbf{K}, \gamma)$ . Also, we have defined

$$\kappa_\gamma(\mathbf{K}, \mathbf{k}) \equiv \frac{1}{2\pi}\left(\frac{\hbar\omega_k}{E_{\text{Pl}}}\right)K^{-3/2}F_\gamma(\hat{\mathbf{K}}, \hat{\mathbf{k}}), \quad (3.9)$$

which can be interpreted as a measure of the EM-GWs coupling strength. By straightforward algebra, one may show that

$$\begin{aligned}
\hat{T}\hat{b}_K\hat{T}^\dagger &= \hat{b}_K + \hat{a}_\mathbf{k}^\dagger\hat{a}_\mathbf{k}\kappa_\gamma(\mathbf{K}, \mathbf{k})e^{-i\mathbf{K}\cdot\mathbf{x}}, \\
\hat{T}\hat{b}_K^\dagger\hat{T}^\dagger &= \hat{b}_K^\dagger + \hat{a}_\mathbf{k}^\dagger\hat{a}_\mathbf{k}\kappa_\gamma(\mathbf{K}, \mathbf{k})e^{i\mathbf{K}\cdot\mathbf{x}}, \\
\hat{T}\hat{a}_\mathbf{k}^\dagger\hat{a}_\mathbf{k}\hat{T}^\dagger &= \hat{a}_\mathbf{k}^\dagger\hat{a}_\mathbf{k},
\end{aligned} \tag{3.10}$$

which is a generalization of the result of [123] to the case of detector of arbitrary size, for which  $KL \sim 1$ . For a unitary operator  $\hat{T}$  and a given function  $\hat{f}(\{\hat{X}_i\})$  of some operators  $\hat{X}_i$ , one has the property  $\hat{T}\hat{f}(\{\hat{X}_i\})\hat{T}^\dagger = \hat{f}(\{\hat{T}\hat{X}_i\hat{T}^\dagger\})$ . With the help of this property, the time evolution operator may be written as

$$\begin{aligned}
\hat{T}^\dagger \left( \hat{T}\hat{U}\hat{T}^\dagger \right) \hat{T} &= \hat{U} = e^{-i\omega_k\hat{a}_\mathbf{k}^\dagger\hat{a}_\mathbf{k}t} e^{i(\hat{a}_\mathbf{k}^\dagger\hat{a}_\mathbf{k})^2 \sum_\gamma \int d^3\mathbf{K}\kappa_\gamma^2(\mathbf{K}, \mathbf{k})(\Omega_K t)} \\
&\times e^{\hat{a}_\mathbf{k}^\dagger\hat{a}_\mathbf{k} \sum_\gamma \int d^3\mathbf{K}\kappa_\gamma(\mathbf{K}, \mathbf{k}) \left( \hat{b}_K^\dagger e^{-i\mathbf{K}\cdot\mathbf{x}} - \hat{b}_K e^{i\mathbf{K}\cdot\mathbf{x}} \right)} e^{-i \sum_\gamma \int d^3\mathbf{K}\hat{b}_K^\dagger\hat{b}_K(\Omega_K t)} \\
&\times e^{-\hat{a}_\mathbf{k}^\dagger\hat{a}_\mathbf{k} \sum_\gamma \int d^3\mathbf{K}\kappa_\gamma(\mathbf{K}, \mathbf{k}) \left( \hat{b}_K^\dagger e^{-i\mathbf{K}\cdot\mathbf{x}} - \hat{b}_K e^{i\mathbf{K}\cdot\mathbf{x}} \right)} e^{i \int d^3\mathbf{K}\hat{b}_K^\dagger\hat{b}_K(\Omega_K t)} e^{-i \int d^3\mathbf{K}\hat{b}_K^\dagger\hat{b}_K(\Omega_K t)}.
\end{aligned} \tag{3.11}$$

Terms containing  $\hat{a}_\mathbf{k}^\dagger\hat{a}_\mathbf{k}$  commute with each other, and in the last line we inserted the unit operator  $\mathcal{I} = e^{i \int d^3\mathbf{K}\hat{b}_K^\dagger\hat{b}_K(\Omega_K t)} e^{-i \int d^3\mathbf{K}\hat{b}_K^\dagger\hat{b}_K(\Omega_K t)}$ . By rearranging the terms and using the Baker–Campbell–Hausdorff formula, one may finally find the time evolution operator as

$$\hat{U}(\mathbf{x}, t) = e^{iE(t)(\hat{a}_\mathbf{k}^\dagger\hat{a}_\mathbf{k})^2} e^{\hat{a}_\mathbf{k}^\dagger\hat{a}_\mathbf{k} \sum_\gamma \int d^3\mathbf{K}\kappa(\hat{\mathbf{K}}, \hat{\mathbf{k}}) \left( \hat{b}_K^\dagger \nu_{\mathbf{K}}(\mathbf{x}, t) - \hat{b}_K \nu_{\mathbf{K}}^*(\mathbf{x}, t) \right)} e^{-i\omega_k\hat{a}_\mathbf{k}^\dagger\hat{a}_\mathbf{k}t} e^{-i \sum_\gamma \int d^3\mathbf{K}\hat{b}_K^\dagger\hat{b}_K(\Omega_K t)}. \tag{3.12}$$

In the above expression, we have defined

$$\begin{aligned}
\nu_{\mathbf{K}}(\mathbf{x}, t) &\equiv \left( 1 - e^{-i\Omega_K t} \right) e^{-i\mathbf{K}\cdot\mathbf{x}}, \\
E(t) &\equiv \sum_\gamma \int d^3\mathbf{K}\kappa_\gamma^2(\mathbf{K}, \mathbf{k}) \left( \Omega_K t - \sin(\Omega_K t) \right).
\end{aligned} \tag{3.13}$$

Note that the spatial-dependence of the time evolution operator is inherited from the spatial-dependence of the underlying GWs background, through the spatial phase factors  $e^{\pm i\mathbf{K}\cdot\mathbf{x}}$ .

With the help of  $\hat{U}(\mathbf{x}, t)$ , both Schrödinger and Heisenberg dynamics can be perused. We proceed by choosing the Heisenberg picture, where equation of motion for the EM field operators can be solved without effort, thanks to the well-established cavity opto-mechanical investigations. Time-evolution of the EM field operator  $\hat{a}_\mathbf{k}(\mathbf{x}, t)$  can be obtained from  $\hat{U}(\mathbf{x}, t)$  according to

$$\begin{aligned}
\hat{a}_\mathbf{k}(\mathbf{x}, t) &= \hat{U}^\dagger(\mathbf{x}, t)\hat{a}_\mathbf{k}\hat{U}(\mathbf{x}, t) \\
&= e^{i \sum_\gamma \int d^3\mathbf{K}\hat{b}_K^\dagger\hat{b}_K(\Omega_K t)} e^{i\omega_k\hat{a}_\mathbf{k}^\dagger\hat{a}_\mathbf{k}t} e^{-\hat{a}_\mathbf{k}^\dagger\hat{a}_\mathbf{k} \sum_\gamma \int d^3\mathbf{K}\kappa_\gamma(\mathbf{K}, \mathbf{k}) \left( \hat{b}_K^\dagger \nu_{\mathbf{K}}(\mathbf{x}, t) - \hat{b}_K \nu_{\mathbf{K}}^*(\mathbf{x}, t) \right)} e^{-iE(t)(\hat{a}_\mathbf{k}^\dagger\hat{a}_\mathbf{k})^2} \hat{a}_\mathbf{k} \\
&\times e^{iE(t)(\hat{a}_\mathbf{k}^\dagger\hat{a}_\mathbf{k})^2} e^{\hat{a}_\mathbf{k}^\dagger\hat{a}_\mathbf{k} \sum_\gamma \int d^3\mathbf{K}\kappa_\gamma(\mathbf{K}, \mathbf{k}) \left( \hat{b}_K^\dagger \nu_{\mathbf{K}}(\mathbf{x}, t) - \hat{b}_K \nu_{\mathbf{K}}^*(\mathbf{x}, t) \right)} e^{-i\omega_k\hat{a}_\mathbf{k}^\dagger\hat{a}_\mathbf{k}t} e^{-i \sum_\gamma \int d^3\mathbf{K}\hat{b}_K^\dagger\hat{b}_K(\Omega_K t)}.
\end{aligned} \tag{3.14}$$



Using the formula  $e^{\hat{A}}\hat{B}e^{-\hat{A}} = \hat{B} + [\hat{A}, \hat{B}] + \frac{1}{2!}[\hat{A}, [\hat{A}, \hat{B}]] + \dots$ , one may show that

$$\begin{aligned}
(1) \quad & e^{-iE(t)(\hat{a}_{\mathbf{k}}^\dagger \hat{a}_{\mathbf{k}})^2} \hat{a}_{\mathbf{k}} e^{iE(t)(\hat{a}_{\mathbf{k}}^\dagger \hat{a}_{\mathbf{k}})^2} = e^{2iE(t)\left(\hat{a}_{\mathbf{k}}^\dagger \hat{a}_{\mathbf{k}} + \frac{1}{2}\right)} \hat{a}_{\mathbf{k}}, \\
(2) \quad & e^{-\hat{a}_{\mathbf{k}}^\dagger \hat{a}_{\mathbf{k}} \sum_{\gamma} \int d^3 \mathbf{K} \kappa_{\gamma}(\mathbf{K}, \mathbf{k}) \left( \hat{b}_{K\nu_{\mathbf{K}}}^\dagger(\mathbf{x}, t) - \hat{b}_{K\nu_{\mathbf{K}}}^*(\mathbf{x}, t) \right)} e^{2iE(t)\left(\hat{a}_{\mathbf{k}}^\dagger \hat{a}_{\mathbf{k}} + \frac{1}{2}\right)} \hat{a}_{\mathbf{k}} e^{\hat{a}_{\mathbf{k}}^\dagger \hat{a}_{\mathbf{k}} \sum_{\gamma} \int d^3 \mathbf{K} \kappa_{\gamma}(\mathbf{K}, \mathbf{k}) \left( \hat{b}_{K\nu_{\mathbf{K}}}^\dagger(\mathbf{x}, t) - \hat{b}_{K\nu_{\mathbf{K}}}^*(\mathbf{x}, t) \right)} \\
& = e^{2iE(t)\left(\hat{a}_{\mathbf{k}}^\dagger \hat{a}_{\mathbf{k}} + \frac{1}{2}\right)} \hat{a}_{\mathbf{k}} e^{\sum_{\gamma} \int d^3 \mathbf{K} \kappa_{\gamma}(\mathbf{K}, \mathbf{k}) \left( \hat{b}_{K\nu_{\mathbf{K}}}^\dagger(\mathbf{x}, t) - \hat{b}_{K\nu_{\mathbf{K}}}^*(\mathbf{x}, t) \right)} \\
(3) \quad & e^{i\omega_{\mathbf{k}} \hat{a}_{\mathbf{k}}^\dagger \hat{a}_{\mathbf{k}} t} e^{2iE(t)\left(\hat{a}_{\mathbf{k}}^\dagger \hat{a}_{\mathbf{k}} + \frac{1}{2}\right)} \hat{a}_{\mathbf{k}} e^{\sum_{\gamma} \int d^3 \mathbf{K} \kappa_{\gamma}(\mathbf{K}, \mathbf{k}) \left( \hat{b}_{K\nu_{\mathbf{K}}}^\dagger(\mathbf{x}, t) - \hat{b}_{K\nu_{\mathbf{K}}}^*(\mathbf{x}, t) \right)} \\
& = e^{2iE(t)\left(\hat{a}_{\mathbf{k}}^\dagger \hat{a}_{\mathbf{k}} + \frac{1}{2}\right)} \hat{a}_{\mathbf{k}} e^{-i\omega_{\mathbf{k}} t} e^{\sum_{\gamma} \int d^3 \mathbf{K} \kappa_{\gamma}(\mathbf{K}, \mathbf{k}) \left( \hat{b}_{K\nu_{\mathbf{K}}}^\dagger(\mathbf{x}, t) - \hat{b}_{K\nu_{\mathbf{K}}}^*(\mathbf{x}, t) \right)}
\end{aligned}$$

Thus, Eq. (3.14) can be written as follows

$$\hat{a}_{\mathbf{k}}(\mathbf{x}, t) = e^{-\sum_{\gamma} \int d^3 \mathbf{K} \kappa_{\gamma}(\mathbf{K}, \mathbf{k}) \left( \hat{b}_{K\nu_{\mathbf{K}}}^\dagger(\mathbf{x}, t) - \hat{b}_{K\nu_{\mathbf{K}}}^*(\mathbf{x}, t) \right)} e^{2iE(t)\left(\hat{a}_{\mathbf{k}}^\dagger \hat{a}_{\mathbf{k}} + \frac{1}{2}\right)} e^{-i\omega_{\mathbf{k}} t} \hat{a}_{\mathbf{k}}. \quad (3.15)$$

where we have defined

$$\eta_{\mathbf{K}}(\mathbf{x}, t) \equiv (1 - e^{i\Omega_{\mathbf{K}} t}) e^{-i\mathbf{K} \cdot \mathbf{x}}. \quad (3.16)$$

Note that in the above equations,  $(\hat{a}_{\mathbf{k}}, \hat{a}_{\mathbf{k}}^\dagger)$  stand for the EM ladder operators at the initial moment (before the EM-GWs interaction takes place). Expression (3.15) is a generalization of the result of [122, 123] to the case of a continuum of GWs modes, where the spatial-dependence of the field operators is included, i.e., without the small detector approximation ( $KL \ll 1$ ), and with a general geometric configuration encoded in the detector pattern function  $F_{\gamma}(\hat{\mathbf{K}}, \hat{\mathbf{k}})$ .

One may identify the *displacement operator* associated to GWs of mode  $K$  as follows

$$\hat{D}_K(-\kappa_{\gamma}(\mathbf{K}, \mathbf{k})\eta_{\mathbf{K}}(\mathbf{x}, t)) \equiv \exp\left(-\kappa_{\gamma}(\mathbf{K}, \mathbf{k})\eta_{\mathbf{K}}(\mathbf{x}, t)\hat{b}_K^\dagger + \kappa_{\gamma}(\mathbf{K}, \mathbf{k})\eta_{\mathbf{K}}^*(\mathbf{x}, t)\hat{b}_K\right), \quad (3.17)$$

Now, if one formally discretizes the integration over GWs modes in Eq. (3.15) according to  $\int d^3 \mathbf{K} \rightarrow \frac{(2\pi)^3}{V} \sum_{\mathbf{K}}$ , Eq. (3.15) becomes

$$\hat{a}_{\mathbf{k}}(\mathbf{x}, t) = \left( \prod_{\gamma, \mathbf{K}} \hat{D}_K(-\kappa_{\gamma}(\mathbf{K}, \mathbf{k})\eta_{\mathbf{K}}(\mathbf{x}, t)) \right) e^{2iE(t)\left(\hat{a}_{\mathbf{k}}^\dagger \hat{a}_{\mathbf{k}} + \frac{1}{2}\right)} e^{-i\omega_{\mathbf{k}} t} \hat{a}_{\mathbf{k}}. \quad (3.18)$$

The quantity inside the braces is nothing but the tensor product of displacement operators of each GWs mode. Hence each mode interacts with the EM field independently of the other modes. The appearance of the displacement operator of the tensor field in the EM field dynamics can be justified by our intuition about the opto-mechanical system. In a cavity opto-mechanical system, a single-mode EM field couples with the vibrational mode of the end mirror of the cavity and the radiation pressure leads the mirror to vibrate. Vibration of the end mirror causes the resonant frequency of the the EM field to change as  $\omega = \frac{n\pi}{L} \rightarrow \frac{n\pi}{L+\Delta L} = \omega + \Delta\omega$ . In the EM-GWs analogous case, the strain field of GWs leads the EM frequency to change, and the appearance of the displacement operator of GWs in the evolution of the EM field can be understood from the analogy with the vibrational mode in cavity opto-mechanical system.

One interesting aspect that can be deduced from Eq. (3.18) is the *decoherence* induced by GWs, as previously studied in [95]. However, in the following, we focus on the *incoherence* of the EM field induced by GWs, e.g., the loss of spatial correlations of the EM field caused

by GWs. Before doing so, it is beneficial to separate the contribution of the opposite momenta  $\mathbf{K}$  and  $-\mathbf{K}$  in Eq. (3.18). This step makes the investigation of the two-mode squeezed PGWs easier. To separate the contribution of the opposite momenta, one may start from the interaction Hamiltonian Eq. (3.5) and rewrite it as

$$\hat{H}_{\text{int}}^{(S)}(\mathbf{x}) \equiv \hat{H}_{\text{int}}^{(S,+)}(\mathbf{x}) + \hat{H}_{\text{int}}^{(S,-)}(\mathbf{x}), \quad (3.19)$$

where  $\hat{H}_{\text{int}}^{(S,\pm)}$  are given by Eq. (3.5) with integral limits  $\mathbf{K} \in \mathfrak{R}^{3\pm}$ , respectively. In this manner, the two Hamiltonians commute,  $[\hat{H}_{\text{int}}^{(S,+)}, \hat{H}_{\text{int}}^{(S,-)}] = 0$ . One may easily check that the operator  $\hat{T}$  introduced by Eq. (3.8) can be factorized into *positive* and *negative* commuting parts,  $\hat{T} \equiv \hat{T}^{(+)} \otimes \hat{T}^{(-)}$  where  $[\hat{T}^{(+)}, \hat{T}^{(-)}] = 0$ , and each part is the same as Eq. (3.8) with the integral range  $\mathbf{K} \in \mathfrak{R}^{3\pm}$ . Similarly, the time evolution operator  $\hat{U}(\mathbf{x}, t)$  can be factorized into positive and negative parts, namely  $\hat{U} = \hat{U}^{(+)} \otimes \hat{U}^{(-)}$ . Following the same steps, one ends up with the following expression for  $\hat{a}_{\mathbf{k}}(\mathbf{x}, t)$

$$\begin{aligned} \hat{a}_{\mathbf{k}}(\mathbf{x}, t) = & \left( \prod_{\gamma, \mathbf{K} \in \mathfrak{R}^{3+}} \hat{D}_{\mathbf{K}, \gamma}(-\kappa_{\gamma}(\mathbf{K}, \mathbf{k})\eta_{\mathbf{K}}(\mathbf{x}, t)) \otimes \hat{D}_{-\mathbf{K}, \gamma}(-\kappa_{\gamma}(\mathbf{K}, \mathbf{k})\eta_{-\mathbf{K}, \gamma}(\mathbf{x}, t)) \right) \\ & \times e^{2iE(t)\left(\hat{a}_{\mathbf{k}}^{\dagger}\hat{a}_{\mathbf{k}} + \frac{1}{2}\right)} e^{-i\omega_{\mathbf{k}}t}\hat{a}_{\mathbf{k}}, \end{aligned} \quad (3.20)$$

that is direct product of  $\mathbf{K}$  and  $-\mathbf{K}$  modes, as one could expect from Eq. (3.18). With the help of Eq. (3.20), we are equipped to investigate spatial correlations of the EM field emitted from distant objects, in the presence of the two-mode squeezed PGWs background.

## 4 Loss of spatial coherence induced by two-mode squeezed PGWs

### 4.1 Spatial correlations in the presence of GWs

To investigate the effect of PGWs background on EM field spatial correlations, we first describe the experimental setup depicted in Fig. 2, which presents the physical concept of spatial correlations of the EM field, based on which the angular size of extended objects is measured.

#### 4.1.1 Configuration of a VLBI-type system

Figure 2 panel (a) shows a typical Michelson stellar interferometer setup. The EM field radiated from two distant edges of a planar source  $\sigma$  of radius  $a$  (for example a star), each of which denoted by wave vectors  $\mathbf{k}$  and  $\mathbf{k}'$ , illuminate two mirrors  $M_1$  and  $M_2$ , located at  $\mathbf{x}_1$  and  $\mathbf{x}_2$  respectively. For simplicity, we take the origin of coordinates at the center of the planar source. The signals are then combined in point  $P$  at zero difference-time (note that two paths  $\overline{M_1P}$  and  $\overline{M_2P}$  are equal). Panel (b) represents an equivalent situation where the mirrors are replaced by detectors, and the interference pattern is produced by combining the signal at the output of each detector. This is a typical VLBI configuration. In practical situation of a typical VLBI instrument, orientation of the source with respect to detector baseline makes an angle  $\vartheta_s$ , as is shown in panel (b). It causes *geometrical delay*  $\tau_g = (\mathbf{x}_1 - \mathbf{x}_2) \cdot \mathbf{k}/c$  that is often compensated in order to achieve equal-time correlations [124], so that the configuration reduces to the simplified one of panel (a) or (c), where there is no delay time. Panel (c) shows the symmetric configuration, corresponding to the Michelson setup panel (a). In the figure,  $\mathbf{K} = (K, \Theta_K, \Phi_K)$  represents the GWs wave vector in polar coordinates. We assume that the planar source lies in the  $x - y$  plane, and the two detectors are symmetrically located the  $z$ -axis. The angle  $\theta$  represents the angular diameter subtended by the source, when viewed from  $M_1M_2$  on the Earth.

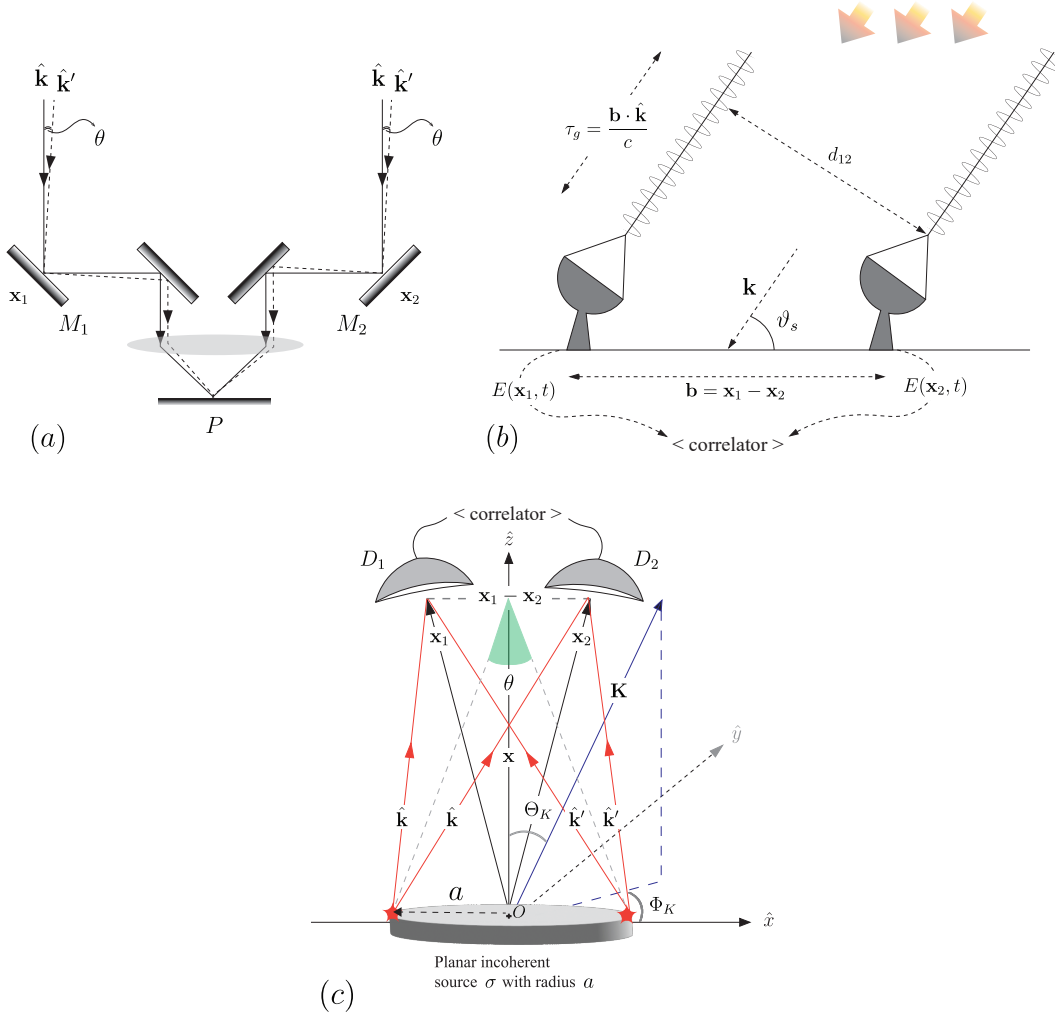


**Figure 2.** Configuration of the system. *Panel (a)*: a typical Michelson stellar interferometer which consists of two mirrors  $M_1$  and  $M_2$  located at positions  $\mathbf{x}_1$  and  $\mathbf{x}_2$ . The EM field emitted from two distant edges of an extended source  $\sigma$ , possessing wave vectors  $\mathbf{k}$  and  $\mathbf{k}'$ , illuminates the mirrors and the intensity is observed in the focal plane of a lens, at point  $P$ . *Panel (b)*: Equivalent representation in a VLBI-type configuration in which the mirrors  $M_1$  and  $M_2$  of the Michelson stellar interferometer are replaced by detectors  $D_1$  and  $D_2$ . Interference pattern is produced by beating the signals coming from the two detectors thanks to a correlator. *Panel (c)*: representation of the symmetric configuration and different physical quantities that are used in the text. The angle  $\theta$  is the angular diameter of the source as seen from the detector.

#### 4.1.2 Equal-time first-order degree of coherence $g^{(1)}(\mathbf{x}_1, t; \mathbf{x}_2, t)$

For the Michelson stellar interferometer shown in figure 1 panel (a), the expression of the intensity at point  $P$  is given by

$$I(\mathbf{x}_P, t) = \langle \hat{E}^{(-)}(\mathbf{x}_P, t) \hat{E}^{(+)}(\mathbf{x}_P, t) \rangle, \quad (4.1)$$

where the positive and negative frequency parts of the electric field at point  $P$  and time  $t$  are given by

$$\hat{E}^{(+)}(\mathbf{x}_P, t) = \hat{E}^{(+)}(\mathbf{x}_1, t - \tau_1) + \hat{E}^{(+)}(\mathbf{x}_2, t - \tau_2), \quad (4.2)$$

and its Hermitian conjugate. Here,  $\tau_i$  accounts for the time delay of the EM signal through the arm  $\overline{M_i P}$ , with  $i = 1, 2$ . In the symmetric setup one has  $\tau_1 = \tau_2$ , which is also true in VLBI measurement thanks to the geometric delay line that ensures equal time correlation. For simplicity we proceed by setting  $t - \tau_1 = t - \tau_2 \equiv t$  and we neglect the effect of the GWs background during the time delays  $\tau_i$  (since  $\tau_i \lll t$ ). Therefore,  $t$  will now refer to the time at which the EM signal arrives to the detectors.

In a first approach, we consider the simplified case where only two wave vectors  $\mathbf{k}$  and  $\mathbf{k}'$ , coming from two distant edges of the extended source, illuminate the detectors (see panel (c) of figure 2). This simplified picture lets us grasp the phenomenon of incoherence induced by PGWs, and is straightforward to be generalized to the continuum EM emission from all different parts of the extended source, with all possible wave vectors  $\mathbf{k} \in \sigma$ . Thus, the positive and negative frequency parts of the electric field at the location of each mirror are specified by

$$\hat{E}^{(+)}(\mathbf{x}_i, t) = \mathcal{E}_{\mathbf{k}} \left( \hat{a}_{\mathbf{k}}(\mathbf{x}_i, t) e^{i\mathbf{k} \cdot \mathbf{x}_i} + \hat{a}_{\mathbf{k}'}(\mathbf{x}_i, t) e^{i\mathbf{k}' \cdot \mathbf{x}_i} \right), \quad i = 1, 2 \quad (4.3)$$

and its Hermitian conjugate. Here,  $\mathcal{E}_{\mathbf{k}}$  represents the electric field amplitude of mode  $\mathbf{k}$  of the EM field and can be considered equal with  $\mathcal{E}_{\mathbf{k}'}$  without losing generality, assuming a uniform radiation intensity from the source. Moreover,  $\hat{a}_{\mathbf{k}}(\mathbf{x}_i, t)$  and  $\hat{a}_{\mathbf{k}'}(\mathbf{x}_i, t)$  denote the annihilation operators of the EM field of modes  $\mathbf{k}$  and  $\mathbf{k}'$ , respectively, and their evolution through GWs background is determined by Eq. (3.20). Plugging Eq. (4.3) into Eq. (4.2) and using Eq. (4.1), one obtains the following expression for the intensity

$$I(\mathbf{x}_P, t) = |\mathcal{E}_{\mathbf{k}}|^2 \left\{ \langle \hat{n}_{\mathbf{k}}(\mathbf{x}_1, t) \rangle + \langle \hat{n}_{\mathbf{k}'}(\mathbf{x}_1, t) \rangle + \langle \hat{n}_{\mathbf{k}}(\mathbf{x}_2, t) \rangle + \langle \hat{n}_{\mathbf{k}'}(\mathbf{x}_2, t) \rangle \right. \\ \left. + 2\Re \left[ \langle \hat{a}_{\mathbf{k}}^\dagger(\mathbf{x}_1, t) \hat{a}_{\mathbf{k}}(\mathbf{x}_2, t) \rangle e^{-i\mathbf{k} \cdot (\mathbf{x}_1 - \mathbf{x}_2)} + \mathbf{k} \longleftrightarrow \mathbf{k}' \right] \right\}, \quad (4.4)$$

where  $\hat{n}_{\mathbf{k}} = \hat{a}_{\mathbf{k}}^\dagger \hat{a}_{\mathbf{k}}$  represents the number operator of photons in mode  $\mathbf{k}$ . In Eq. (4.4), cross-correlations like  $\langle \hat{a}_{\mathbf{k}}^\dagger \hat{a}_{\mathbf{k}'} \rangle = \langle \hat{a}_{\mathbf{k}}^\dagger \rangle \langle \hat{a}_{\mathbf{k}'} \rangle$  between independent modes  $\mathbf{k}$  and  $\mathbf{k}'$  vanish, assuming that each mode of the EM field is in thermal state and  $\langle \hat{a}_{\mathbf{k}} \rangle = 0$ . The first line in Eq. (4.4) represents the contribution of each mode in the intensity at each point  $\mathbf{x}_i$ , while the second line shows the role of correlations in each mode, in the interference pattern. In absence of GWs, the annihilation operator simply reduces to the free field case,  $\hat{a}_{\mathbf{k}(\mathbf{k}')}(\mathbf{x}, t) \rightarrow e^{-i\omega_{\mathbf{k}} t} \hat{a}_{\mathbf{k}(\mathbf{k}')}$  (see Eq. (3.20)) and Eq. (4.4) recasts to the free-field expression. The quantity inside the brackets is closely related to the equal-time first-order degree of coherence defined by [125]

$$g_{\mathbf{k}}^{(1)}(\mathbf{x}_1, t; \mathbf{x}_2, t) \equiv \frac{\langle \hat{a}_{\mathbf{k}}^\dagger(\mathbf{x}_1, t) \hat{a}_{\mathbf{k}}(\mathbf{x}_2, t) \rangle}{\langle \hat{n}_{\mathbf{k}} \rangle} \quad (4.5) \\ = \prod_{\gamma, \mathbf{K} \in \mathbb{R}^{3+}} \left\langle \hat{D}_{\mathbf{K}}^\dagger(-\kappa\eta_{\mathbf{K}}(\mathbf{x}_1, t)) \hat{D}_{\mathbf{K}}(-\kappa\eta_{\mathbf{K}}(\mathbf{x}_2, t)) \right. \\ \left. \times \hat{D}_{-\mathbf{K}}^\dagger(-\kappa\eta_{-\mathbf{K}}(\mathbf{x}_1, t)) \hat{D}_{-\mathbf{K}}(-\kappa\eta_{-\mathbf{K}}(\mathbf{x}_2, t)) \right\rangle_{\hat{\rho}_{\text{GWs}}}$$

Here, the subscript  $\mathbf{k}$  is written explicitly in  $g_{\mathbf{k}}^{(1)}(\mathbf{x}_1, t; \mathbf{x}_2, t)$ . A similar expression holds for the mode  $\mathbf{k}'$ . However, as we show in App. B.1,  $g_{\mathbf{k}}^{(1)}(\mathbf{x}_1, t; \mathbf{x}_2, t)$  is identical for all EM wave vectors  $\mathbf{k}$  emitted from the source  $\sigma$  up to  $\mathcal{O}(\theta^2) \sim 10^{-16}$  (for the typical quasar considered

in this paper). Hence one may suppress the subscript  $\mathbf{k}$  and simply write  $g^{(1)}(\mathbf{x}_1, t; \mathbf{x}_2, t)$  for all modes  $\mathbf{k}$  for the sake of abbreviation. Furthermore, in the last line of Eq. (4.5), we used the expression of the ladder operators previously determined by Eq. (3.20).

The expectation value in Eq. (4.5) is generally taken over the total state  $\hat{\rho} = \hat{\rho}_{\text{GWs}} \otimes \hat{\rho}_{\mathbf{k}} \otimes \hat{\rho}_{\mathbf{k}'}$ , where  $\hat{\rho}_{\text{GWs}}$  describes the state of GWs, and  $\hat{\rho}_{\mathbf{k}}$  and  $\hat{\rho}_{\mathbf{k}'}$  stand for the state of the EM field of modes  $\mathbf{k}$  and  $\mathbf{k}'$ . One may assume the emission of distant objects to be dominated by a thermal emission with mean number of photons  $\langle \hat{n}_{\mathbf{k}} \rangle = [\exp(\hbar\omega_{\mathbf{k}}/k_{\text{B}}T) - 1]^{-1}$ . However, as it can be seen from Eq. (4.4) and (4.5), the state of the EM field does not play an important role and only the mean number of photons matters. This is one of the main features that makes spatial correlations favorable with respect to temporal correlations that drastically depend on the EM state. Thus, the degree of coherence depends *only* on the state of GWs, as indicated in Eq. (4.5). Assuming equal mean number of photons in each mode  $\mathbf{k}$  and  $\mathbf{k}'$ ,  $\langle \hat{n}_{\mathbf{k}} \rangle = \langle \hat{n}_{\mathbf{k}'} \rangle = \langle \hat{n} \rangle$ , Eq. (4.4) reduces to

$$I(\mathbf{x}_P, t) = |\mathcal{E}_{\mathbf{k}}|^2 \left\{ 4\langle \hat{n} \rangle + 2\langle \hat{n} \rangle \Re \left[ g^{(1)}(\mathbf{x}_1, t; \mathbf{x}_2, t) e^{-i\mathbf{k} \cdot (\mathbf{x}_1 - \mathbf{x}_2)} + \mathbf{k} \longleftrightarrow \mathbf{k}' \right] \right\}. \quad (4.6)$$

where  $g^{(1)}(\mathbf{x}_1, t; \mathbf{x}_2, t)$  is determined by Eq. (4.5). In absence of GWs background one has  $g^{(1)}(\mathbf{x}_1, t; \mathbf{x}_2, t) \rightarrow 1$  and Eq. (4.5) reduces to the standard interference pattern in free space (see Eq. (4.1.24) of [125]).

The presence of GWs background act as the modulating factor  $g^{(1)}(\mathbf{x}_1, t; \mathbf{x}_2, t)$ , which is a complex value function. The phase of  $g^{(1)}(\mathbf{x}_1, t; \mathbf{x}_2, t)$  physically represents a shift in the interference pattern, which is a *coherent* effect. The modulus of  $g^{(1)}(\mathbf{x}_1, t; \mathbf{x}_2, t)$  affects the visibility of the interference pattern and is dubbed as an *incoherent* effect. In the following, we compute  $g^{(1)}(\mathbf{x}_1, t; \mathbf{x}_2, t)$  in the presence of two-mode squeezed PGWs. We intentionally present the calculations step by step to show subtleties and avoid misunderstanding. App. D is devoted to the computation of  $g^{(1)}(\mathbf{x}_1, t; \mathbf{x}_2, t)$  in the presence of GWs in (i) vacuum, (ii) thermal and (iii) squeezed states. This latter step may help understand and discriminate between different mechanisms associated to different quantum states of GWs. Besides, it turns out that, as long as spatial correlations of the EM field are concerned, one may not be able to distinguish between two-mode squeezed and thermal states of GWs that possess exactly the same graviton content, since they leave almost the same footprint on the EM spatial correlations.

## 4.2 First-order degree of coherence in the presence of PGWs in two-mode squeezed state

In this section, we compute the expression of correlation function Eq. (4.5) when GWs are in the two-mode squeezed state  $|\text{TS}(\eta_H)\rangle$ , specified by Eq. (2.10). In this case one has

$$\begin{aligned} g_{\text{ts}}^{(1)}(1; 2) &= \prod_{\gamma, \mathbf{K} \in \mathbb{R}^{3+}} \langle 0_{\mathbf{K}}, 0_{-\mathbf{K}} | \hat{R}_{\mathbf{K}}^\dagger \hat{S}_{\mathbf{K}}^\dagger \hat{D}_{\mathbf{K}}^\dagger(-\kappa\eta_{\mathbf{K}}(1)) \hat{D}_{\mathbf{K}}(-\kappa\eta_{\mathbf{K}}(2)) \\ &\quad \times \hat{D}_{-\mathbf{K}}^\dagger(-\kappa\eta_{-\mathbf{K}}(1)) \hat{D}_{-\mathbf{K}}(-\kappa\eta_{-\mathbf{K}}(2)) \hat{S}_{\mathbf{K}} \hat{R}_{\mathbf{K}} | 0_{\mathbf{K}}, 0_{-\mathbf{K}} \rangle. \end{aligned} \quad (4.7)$$

Here, for the sake of abbreviation, we used  $\kappa$  in place of  $\kappa_\gamma(\mathbf{K}, \mathbf{k})$  and  $(1, 2)$  in place of  $(\mathbf{x}_1, t)$  and  $(\mathbf{x}_2, t)$ , respectively (note that  $\kappa_\gamma(\mathbf{K}, \mathbf{k}) = \kappa_\gamma(-\mathbf{K}, \mathbf{k})$  for real polarization tensors). The opposite momenta  $\mathbf{K}$  and  $-\mathbf{K}$  are independent in the half Fourier space  $\mathbb{R}^{3+}$ , consequently their associated displacement operators commute. Using the multiplication property of the

displacement operator,  $\hat{D}^\dagger(\alpha)\hat{D}(\beta) = e^{-i\Im(\alpha\beta^*)}\hat{D}(\beta - \alpha)$ , one has

$$\hat{D}_{\mathbf{K}}^\dagger(-\kappa\eta_{\mathbf{K}}(1))\hat{D}_{\mathbf{K}}(-\kappa\eta_{\mathbf{K}}(2)) = e^{-i\kappa^2\Im(\eta_{\mathbf{K}}(1)\eta_{\mathbf{K}}^*(2))}\hat{D}_{\mathbf{K}}(\kappa[\eta_{\mathbf{K}}(1) - \eta_{\mathbf{K}}(2)]). \quad (4.8)$$

together with a similar expression for  $-\mathbf{K}$ . Here, we remind that  $\Im$  stands for the imaginary part. Thus, Eq. (4.7) can be written as

$$\begin{aligned} g_{\text{ts}}^{(1)}(1; 2) &= e^{-i\sum_\gamma \int_{\mathbf{K} \in \mathbb{R}^3} \kappa^2 \Im(\eta_{\mathbf{K}}(1)\eta_{\mathbf{K}}^*(2))} \prod_{\gamma, \mathbf{K} \in \mathbb{R}^{3+}} \langle 0_{\mathbf{K}}, 0_{-\mathbf{K}} | \hat{R}_{\mathbf{K}}^\dagger \hat{S}_{\mathbf{K}}^\dagger \hat{D}_{\mathbf{K}}(\kappa[\eta_{\mathbf{K}}(1) - \eta_{\mathbf{K}}(2)]) \\ &\quad \times \hat{D}_{-\mathbf{K}}(\kappa[\eta_{-\mathbf{K}}(1) - \eta_{-\mathbf{K}}(2)]) \hat{S}_{\mathbf{K}} \hat{R}_{\mathbf{K}} | 0_{\mathbf{K}}, 0_{-\mathbf{K}} \rangle. \end{aligned} \quad (4.9)$$

The two-mode squeezing operator  $\hat{S}_{\mathbf{K}}$  and the rotation operator  $\hat{R}_{\mathbf{K}}$  involve opposite modes  $\mathbf{K}$  and  $-\mathbf{K}$ , so in order to write Eq. (4.9) in a separated form, we use the following identities

$$\begin{aligned} \hat{R}_{\mathbf{K}}^\dagger \hat{S}_{\mathbf{K}}^\dagger \hat{D}_{\mathbf{K}}(-\kappa\eta_{\mathbf{K}}) \hat{S}_{\mathbf{K}} \hat{R}_{\mathbf{K}} &= \hat{D}_{\mathbf{K}}(-\kappa\eta_{\mathbf{K}} u_K^*) \otimes \hat{D}_{-\mathbf{K}}(\kappa\eta_{\mathbf{K}}^* v_K), \\ \hat{R}_{\mathbf{K}}^\dagger \hat{S}_{\mathbf{K}}^\dagger \hat{D}_{-\mathbf{K}}(-\kappa\eta_{-\mathbf{K}}) \hat{S}_{\mathbf{K}} \hat{R}_{\mathbf{K}} &= \hat{D}_{-\mathbf{K}}(-\kappa\eta_{-\mathbf{K}} u_K^*) \otimes \hat{D}_{\mathbf{K}}(\kappa\eta_{-\mathbf{K}}^* v_K). \end{aligned} \quad (4.10)$$

where  $(u_K, v_K)$  are defined by Eq. (2.13). Note that the quantities related to the PGWs are evaluated at the present time  $\eta_H$ , however, we suppress  $\eta_H$  for the sake of abbreviation. With the help of Eq. (4.10), Eq. (4.9) can be written as follows

$$\begin{aligned} g_{\text{ts}}^{(1)}(1; 2) &= e^{-i\sum_\gamma \int_{\mathbf{K} \in \mathbb{R}^3} \kappa^2 \Im(\eta_{\mathbf{K}}(1)\eta_{\mathbf{K}}^*(2))} \quad (4.11) \\ &\quad \times \prod_{\gamma, \mathbf{K} \in \mathbb{R}^{3+}} \langle 0_{\mathbf{K}} | \hat{D}_{\mathbf{K}}^\dagger(-\kappa u_K^*[\eta_{\mathbf{K}}(1) - \eta_{\mathbf{K}}(2)]) \hat{D}_{\mathbf{K}}(-\kappa v_K[\eta_{-\mathbf{K}}^*(1) - \eta_{-\mathbf{K}}(2)]) | 0_{\mathbf{K}} \rangle \\ &\quad \times \langle 0_{-\mathbf{K}} | \hat{D}_{-\mathbf{K}}^\dagger(\kappa v_K[\eta_{\mathbf{K}}^*(1) - \eta_{\mathbf{K}}^*(2)]) \hat{D}_{-\mathbf{K}}(\kappa u_K^*[\eta_{-\mathbf{K}}(1) - \eta_{-\mathbf{K}}(2)]) | 0_{\mathbf{K}} \rangle \\ &= e^{-i\sum_\gamma \int_{\mathbf{K} \in \mathbb{R}^3} \kappa^2 \Im(\eta_{\mathbf{K}}(1)\eta_{\mathbf{K}}^*(2))} \\ &\quad \times \prod_{\gamma, \mathbf{K} \in \mathbb{R}^{3+}} \left\langle -\kappa u_K^*[\eta_{\mathbf{K}}(1) - \eta_{\mathbf{K}}(2)] \middle| -\kappa v_K[\eta_{-\mathbf{K}}^*(1) - \eta_{-\mathbf{K}}^*(2)] \right\rangle \\ &\quad \times \left\langle \kappa v_K[\eta_{\mathbf{K}}^*(1) - \eta_{\mathbf{K}}^*(2)] \middle| \kappa u_K^*[\eta_{-\mathbf{K}}(1) - \eta_{-\mathbf{K}}(2)] \right\rangle, \end{aligned}$$

Now using the projection property of coherent states  $\langle \alpha | \alpha' \rangle = e^{-\frac{1}{2}|\alpha|^2 - \frac{1}{2}|\alpha'|^2 + \alpha^* \alpha'}$ , it follows that

$$\begin{aligned} g_{\text{ts}}^{(1)}(1; 2) &= e^{-i\sum_\gamma \int_{\mathbf{K} \in \mathbb{R}^3} \kappa^2 \Im(\eta_{\mathbf{K}}(1)\eta_{\mathbf{K}}^*(2))} \prod_{\gamma, \mathbf{K} \in \mathbb{R}^{3+}} \exp\left(-\frac{1}{2}\kappa^2(|u_K|^2 + |v_K|^2)|\eta_{\mathbf{K}}(1) - \eta_{\mathbf{K}}(2)|^2\right) \\ &\quad \times \exp\left(-\frac{1}{2}\kappa^2(|u_K|^2 + |v_K|^2)|\eta_{-\mathbf{K}}(1) - \eta_{-\mathbf{K}}(2)|^2\right) \\ &\quad \times \exp\left[\kappa^2 u_K v_K \left(\eta_{\mathbf{K}}^*(1) - \eta_{\mathbf{K}}^*(2)\right) \left(\eta_{-\mathbf{K}}^*(1) - \eta_{-\mathbf{K}}^*(2)\right) + c.c.\right] \\ &= e^{-i\sum_\gamma \int_{\mathbf{K} \in \mathbb{R}^3} \kappa^2 \Im(\eta_{\mathbf{K}}(1)\eta_{\mathbf{K}}^*(2))} \quad (4.12) \\ &\quad \times \exp\left(-\frac{1}{2} \sum_\gamma \int_{\mathbf{K} \in \mathbb{R}^3} d^3\mathbf{K} \kappa_\gamma^2(\mathbf{K}, \mathbf{k}) \left(1 + 2|v_K|^2\right) |\eta_{\mathbf{K}}(1) - \eta_{\mathbf{K}}(2)|^2\right) \\ &\quad \times \exp\left(\sum_\gamma \int_{\mathbf{K} \in \mathbb{R}^3} d^3\mathbf{K} \kappa_\gamma^2(\mathbf{K}, \mathbf{k}) \Re\left[u_K v_K \left(\eta_{\mathbf{K}}^*(1) - \eta_{\mathbf{K}}^*(2)\right) \left(\eta_{-\mathbf{K}}^*(1) - \eta_{-\mathbf{K}}^*(2)\right)\right]\right). \end{aligned}$$



In the last equality we have transformed to the continuum notation, and used the property  $|u_K|^2 - |v_K|^2 = 1$  for two-mode squeezed states. If one resumes the calculations for GWs in vacuum state, namely  $\hat{\rho}_{\text{vac}} = \prod_K |0_K\rangle\langle 0_K|$ , it can be verified that the contribution of vacuum fluctuations are already involved in the contribution of two-mode squeezed state (see App. D.1). More precisely, one can factorize Eq. (4.12) as contribution of vacuum times a contribution due to the two-mode squeezing,

$$g_{\text{ts}}^{(1)}(\mathbf{x}_1, t; \mathbf{x}_2, t) = g_{\text{vac}}^{(1)}(\mathbf{x}_1, t; \mathbf{x}_2, t) e^{-\mathcal{D}^{\text{ts}}(\mathbf{x}_1, t; \mathbf{x}_2, t)}. \quad (4.13)$$

where  $g_{\text{vac}}^{(1)}$  and  $\mathcal{D}^{\text{ts}}$  are analyzed in the following.

#### 4.2.1 Contribution of vacuum fluctuations of GWs

The contribution of vacuum fluctuations in spatial correlations is determined by (see App. D.1 for details)

$$g_{\text{vac}}^{(1)}(\mathbf{x}_1, t; \mathbf{x}_2, t) = e^{-i\mathcal{C}^{\text{vac}}(\mathbf{x}_1, t; \mathbf{x}_2, t)} e^{-\mathcal{D}^{\text{vac}}(\mathbf{x}_1, t; \mathbf{x}_2, t)}, \quad (4.14)$$

where we have defined

$$\begin{aligned} \mathcal{C}^{\text{vac}}(\mathbf{x}_1, t; \mathbf{x}_2, t) &\equiv \sum_{\gamma} \int_{\mathbf{K} \in \mathbb{R}^3} d^3\mathbf{K} \kappa_{\gamma}^2(\mathbf{K}, \mathbf{k}) \mathcal{C}_{\mathbf{K}}^{\text{vac}}(\mathbf{x}_1, t; \mathbf{x}_2, t), \\ \mathcal{D}^{\text{vac}}(\mathbf{x}_1, t; \mathbf{x}_2, t) &\equiv \frac{1}{2} \sum_{\gamma} \int_{\mathbf{k} \in \mathbb{R}^3} d^3\mathbf{K} \kappa_{\gamma}^2(\mathbf{K}, \mathbf{k}) \mathcal{D}_{\mathbf{K}}^{\text{vac}}(\mathbf{x}_1, t; \mathbf{x}_2, t), \end{aligned} \quad (4.15)$$

together with

$$\begin{aligned} \mathcal{C}_{\mathbf{K}}^{\text{vac}}(\mathbf{x}_1, t; \mathbf{x}_2, t) &\equiv \Im \left[ \eta_{\mathbf{K}}(\mathbf{x}_1, t) \eta_{\mathbf{K}}^*(\mathbf{x}_2, t) \right] \\ &= 4 \sin^2 \left( \frac{\Omega_K t}{2} \right) \sin[\mathbf{K} \cdot (\mathbf{x}_2 - \mathbf{x}_1)] \\ \mathcal{D}_{\mathbf{K}}^{\text{vac}}(\mathbf{x}_1, t_1; \mathbf{x}_2, t_2) &\equiv |\eta_{\mathbf{K}}(\mathbf{x}_1, t) - \eta_{\mathbf{K}}(\mathbf{x}_2, t)|^2 \\ &= 16 \sin^2 \left( \frac{\Omega_K t}{2} \right) \sin^2 \left[ \frac{\mathbf{K} \cdot (\mathbf{x}_2 - \mathbf{x}_1)}{2} \right]. \end{aligned} \quad (4.16)$$

The kernels  $\mathcal{C}^{\text{vac}}(\mathbf{x}_1, t; \mathbf{x}_2, t)$  and  $\mathcal{D}^{\text{vac}}(\mathbf{x}_1, t; \mathbf{x}_2, t)$  represent the contribution of vacuum fluctuations in *coherent* and *incoherent* evolution of spatial correlations of the EM field, respectively. The evaluation of these contributions are postponed to section 5 where we define a coherence criteria based on VLBI observations.

#### 4.2.2 Contribution of gravitons in TS state

The two-point function  $\mathcal{D}^{\text{ts}}(\mathbf{x}_1, t; \mathbf{x}_2, t)$  introduced in Eq. (4.13) encapsulates the effect of gravitons in two-mode squeezed state, and is defined by

$$\begin{aligned} \mathcal{D}^{\text{ts}}(\mathbf{x}_1, t; \mathbf{x}_2, t) &\equiv \sum_{\gamma} \int d^3\mathbf{K} \kappa_{\gamma}^2(\mathbf{K}, \mathbf{k}) \left\{ |v_K(\eta_H)|^2 \mathcal{D}_{\mathbf{K}}^{\text{vac}}(\mathbf{x}_1, t; \mathbf{x}_2, t) \right. \\ &\quad \left. + \frac{1}{2} \mathcal{D}_{\mathbf{K}}^{\text{ts-corr}} \right\}. \end{aligned} \quad (4.17)$$

where  $\mathcal{D}_{\mathbf{K}}^{\text{vac}}(\mathbf{x}_1, t; \mathbf{x}_2, t)$  is already defined by Eq. (4.16). The first term in Eq. (4.17) represents the contribution of the *mean number of gravitons* in the two-mode squeezed state, since

$\bar{n}_{\text{ts}}(K) = |v_K|^2 = \sinh^2 r_K$ . The second term indicates the contribution of *correlations between gravitons* in the TS state, defined by

$$\begin{aligned} \mathcal{D}_{\mathbf{K}}^{\text{ts-corr}}(\mathbf{x}_1, t; \mathbf{x}_2, t) &= 2\Re \left[ u_K v_K \left( \eta_{\mathbf{K}}^*(\mathbf{x}_1, t) - \eta_{\mathbf{K}}^*(\mathbf{x}_2, t) \right) \left( \eta_{-\mathbf{K}}^*(\mathbf{x}_1, t) - \eta_{-\mathbf{K}}^*(\mathbf{x}_2, t) \right) \right] \\ &= \sinh 2r_K \left( 4 \sin^2 \left[ \frac{\mathbf{K} \cdot (\mathbf{x}_2 - \mathbf{x}_1)}{2} \right] \right) \\ &\times \left( \cos(2\phi_K) - 2 \cos(2\phi_K - \Omega_K t) + \cos(2\phi_K - 2\Omega_K t) \right). \end{aligned} \quad (4.18)$$

### 4.3 Characterization of different length-scales $\xi^{\text{vac}}(z)$ , $\delta^{\text{vac}}(z)$ and $\xi^{\text{ts}}(z)$

We may now identify different contributions in  $g_{\text{ts}}^{(1)}(\mathbf{x}_1, t; \mathbf{x}_2, t)$  defined by Eq. (4.13). First, the expression  $\int d^3\mathbf{K} \kappa_\gamma^2(\hat{K}, \hat{\mathbf{k}})$  that appears in Eq. (4.15) and Eq. (4.17) can be expanded as follows (see App. B.1)

$$\sum_\gamma \int_{\mathbf{K} \in \mathbb{R}^3} d^3\mathbf{K} \kappa_\gamma^2(\mathbf{K}, \mathbf{k}) = \frac{1}{(2\pi)^2} \left( \frac{\hbar\omega_k}{E_{\text{Pl}}} \right)^2 \int_0^{2\pi} d\Phi_K \int_0^\pi d\Theta_K \sin^5 \Theta_K \int_{K_E}^{K_1} \frac{dK}{K}. \quad (4.19)$$

Moreover, the quantity  $\mathbf{K} \cdot (\mathbf{x}_2 - \mathbf{x}_1)$  that appears in Eq. (4.16) and (4.18) can be simplified assuming  $Kd_{12} \ll 1$ . Basically, according to panel (c) of Fig. 2 one has  $\mathbf{K} \cdot (\mathbf{x}_2 - \mathbf{x}_1) = Kd_{12} \sin \Theta_K$ . For the largest possible interferometers on the Earth, the separation between detectors could be as long as the Earth's radius. Thus, for GWs of frequency  $\Omega_K \ll c/d_{12} \sim c/R_\oplus \sim 50$  Hz, one may safely assume  $Kd_{12} \ll 1$ . Note that, high-frequency part of the PGWs spectrum possess the lowest graviton content as implied by figure 1, and practically does not make a significant contribution in the incoherence mechanism. As a result, we may proceed assuming  $Kd_{12} \ll 1$  in our calculations (see appendix B.2).

Inserting Eq. (4.19) into Eq.(4.15) and (4.17), along with the help of Eq. (B.12), the following compact forms for the two-point functions  $\mathcal{C}^{\text{vac}}$ ,  $\mathcal{D}^{\text{vac}}$  and  $\mathcal{D}^{\text{ts}}$  outcome

$$\begin{aligned} \mathcal{C}^{\text{vac}}(\mathbf{x}_1, t; \mathbf{x}_2, t) &\equiv \left( \frac{d_{12}}{\delta^{\text{vac}}(t)} \right), \\ \mathcal{D}^{\text{vac}}(\mathbf{x}_1, t; \mathbf{x}_2, t) &\equiv \left( \frac{d_{12}}{\xi^{\text{vac}}(t)} \right)^2, \\ \mathcal{D}^{\text{ts}}(\mathbf{x}_1, t; \mathbf{x}_2, t) &\equiv \left( \frac{d_{12}}{\xi^{\text{ts}}(t)} \right)^2. \end{aligned} \quad (4.20)$$

where three length-scales  $\delta^{\text{vac}}(t)$ ,  $\xi^{\text{vac}}(t)$  and  $\xi^{\text{ts}}(t)$  are defined as follow

$$\begin{aligned} \delta^{\text{vac}}(t) &= \left[ \frac{1}{(2\pi)^2} \left( \frac{\hbar\omega_k}{E_{\text{Pl}}} \right)^2 \int_0^{2\pi} d\Phi_K \int_0^\pi d\Theta_K \sin^6 \Theta_K \int_{K_E}^{K_1} dK \left( 4 \sin^2 \left( \frac{\Omega_K t}{2} \right) \right) \right]^{-1}, \\ \xi^{\text{vac}}(t) &= \left[ \frac{1}{2(2\pi)^2} \left( \frac{\hbar\omega_k}{E_{\text{Pl}}} \right)^2 \int_0^{2\pi} d\Phi_K \int_0^\pi d\Theta_K \sin^7 \Theta_K \int_{K_E}^{K_1} dK \left( 4K \sin^2 \left( \frac{\Omega_K t}{2} \right) \right) \right]^{-1/2}, \\ \xi^{\text{ts}}(t) &\equiv \left[ \frac{1}{(2\pi)^2} \left( \frac{\hbar\omega_k}{E_{\text{Pl}}} \right)^2 \int_0^{2\pi} d\Phi_K \int_0^\pi d\Theta_K \sin^7 \Theta_K \int_{K_E}^{K_1} dK K \left\{ \bar{n}_{\text{ts}}(K) \left( 4 \sin^2 \left( \frac{\Omega_K t}{2} \right) \right) \right. \right. \\ &\quad \left. \left. + \frac{1}{2} \sinh 2r_K \left( \cos(2\phi_K) - 2 \cos(2\phi_K - \Omega_K t) + \cos(2\phi_K - 2\Omega_K t) \right) \right\} \right]^{-1/2}. \end{aligned} \quad (4.21)$$

Here, Eq. (2.13) has been used to convert  $(u_K, v_K)$  into the squeezing parameters  $(r_K, \phi_K)$ . For a time of flight which tends to zero,  $t \rightarrow 0$ , the three length-scales tend to infinity which

yields  $g_{\text{ts}}^{(1)}(\mathbf{x}_1, 0; \mathbf{x}_2, 0) \rightarrow 1$ , as one expects. On the other hand, due to interaction with GWs background during the time of flight  $t$ , these length-scales find finite values and may be small enough to affect VLBI coherence measurements, as we are going to investigate in section 5. While the effect of vacuum fluctuations is unavoidable and always exists, the effect of two-mode squeezed gravitons depends crucially on the squeezing amplitude  $r_K$ , so on the graviton creation in the expanding Universe.

Combining Eq. (4.14) and Eq. (4.20), the contribution of two-mode squeezed state of gravitons on the *coherent* and *incoherent* dynamics of spatial correlations can be written as

$$g_{\text{ts}}^{(1)}(\mathbf{x}_1, t; \mathbf{x}_2, t) = e^{-i\left(\frac{d_{12}}{\delta^{\text{vac}}(t)}\right)} e^{-\left(\frac{d_{12}}{\xi^{\text{vac}}(t)}\right)^2} e^{-\left(\frac{d_{12}}{\xi^{\text{ts}}(t)}\right)^2}. \quad (4.22)$$

Therefore, Eq. (4.22) implies that in general, three different mechanisms can be identified : (i) a coherent dynamic that originates only from vacuum fluctuations, (ii) an incoherent mechanism originated from vacuum fluctuations that may ruin the visibility and (iii) an amplified incoherent dynamics stemming from highly-populated two-mode squeezed PGWs. By accounting the similar contribution of mode  $\mathbf{k}'$ , the explicit form of the interference pattern Eq. (4.6) can now be written as

$$I(\mathbf{x}_P, t) = 4\langle n_{\mathbf{k}} \rangle |\mathcal{E}_{\mathbf{k}}|^2 \left\{ 1 + e^{-\left(\frac{d_{12}}{\xi^{\text{vac}}(t)}\right)^2} e^{-\left(\frac{d_{12}}{\xi^{\text{ts}}(t)}\right)^2} \cos \left[ \frac{(\mathbf{k} - \mathbf{k}')(\mathbf{x}_1 - \mathbf{x}_2)}{2} + \frac{d_{12}}{\delta^{\text{vac}}(t)} \right] \right. \\ \left. \times \cos \left[ \frac{(\mathbf{k} + \mathbf{k}')(\mathbf{x}_1 - \mathbf{x}_2)}{2} + \frac{d_{12}}{\delta^{\text{vac}}(t)} \right] \right\}. \quad (4.23)$$

which explicitly shows the coherent and incoherent contributions of GWs. While the effect of  $\delta^{\text{vac}}(t)$  is to *shift* the interference pattern, the effect of  $\xi^{\text{vac}}(t)$  and  $\xi^{\text{ts}}(t)$  appears as the *blurring* of the visibility. The two-mode squeezed state does not add a coherent dynamic in addition to the vacuum one, since one considers a squeezed vacuum and there can not be any extra coherent dynamic over the pure vacuum contribution.

Note that Eq. (4.23) represents the evolution of spatial correlations of the EM field emitted from two distant edges of a planar source, denoted by the wave vectors  $\mathbf{k}$  and  $\mathbf{k}'$ . The generalization to the continuum EM modes, that is to say a summation over all the wave vectors  $\mathbf{k}$  leaving the source, is straightforward and leads the interference pattern  $\cos \left[ \frac{(\mathbf{k} - \mathbf{k}')(\mathbf{x}_1 - \mathbf{x}_2)}{2} + \frac{d_{12}}{\delta^{\text{vac}}(t)} \right] \cos \left[ \frac{(\mathbf{k} + \mathbf{k}')(\mathbf{x}_1 - \mathbf{x}_2)}{2} + \frac{d_{12}}{\delta^{\text{vac}}(t)} \right]$  to be replaced by the van Citter-Zernike correlations  $j(\mathbf{x}_1, \mathbf{x}_2)$ , as investigated in appendix C. Hence, the intensity  $I(\mathbf{x}_P, t)$  given by Eq. (4.23) is replaced by following general expression

$$I(\mathbf{x}_P, t) = 2I \left( 1 + \Re \left[ g_{\text{ts}}^{(1)}(\mathbf{x}_1, t; \mathbf{x}_2, t) j(\mathbf{x}_1, \mathbf{x}_2) \right] \right). \quad (4.24)$$

where  $j(\mathbf{x}_1, \mathbf{x}_2)$  is called the mutual intensity that bears spatial correlations, in absence of GWs background, and is described in the following.

## 5 Implication of PGWs background on VLBI measurements

In this section, we discuss how the van Citter-Zernike correlations are affected by the presence of quantum GWs. We then define a coherence criteria based on the van Citter-Zernike theorem and realize it with the help of the angular size-redshift  $\theta - z$  measurements made by VLBI means. As we shall see, the coherence criteria leads to a stringent constraint on the tensor-to-scalar ratio.

### 5.1 van Citter-Zernike theorem and Very Long Baseline Interferometry (VLBI)

In this section, we first ignore the presence of GWs background and describe the way VLBI method measures the angular size of an object by exploiting the coherence length of a distant source. In this case, the van Citter-Zernike theorem expresses the field correlations at two points in space, generated by a spatially-incoherent, quasi-monochromatic, planar source, according to [18]

$$j(\mathbf{x}_1, \mathbf{x}_2) = \frac{2J_1(\nu)}{\nu}. \quad (5.1)$$

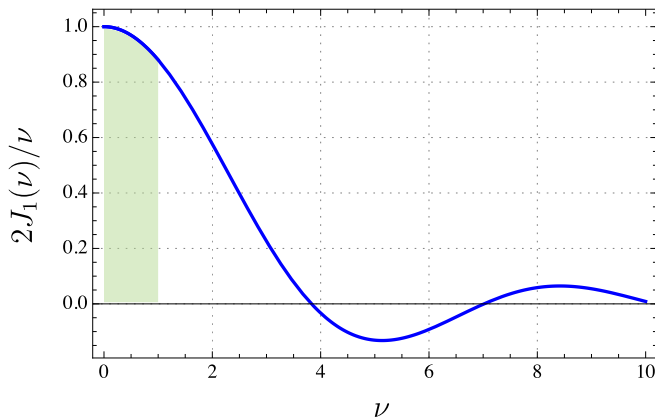


**Figure 3.** The mutual intensity  $j(\mathbf{x}_1, \mathbf{x}_2) = 2J_1(\nu)/\nu$  versus the dimensionless parameter  $\nu = k \left(\frac{a}{x}\right) d_{12}$ . The colored region corresponds to the coherence length  $0 \leq d_{12} \leq 2/k\theta$  where correlations decrease from unity to a value of 0.88. The mutual intensity vanishes for the first time for  $\nu \simeq 3.83$ .

Here,  $j(\mathbf{x}_1, \mathbf{x}_2)$  is called *mutual intensity* or *visibility*, and expresses the equal-time spatial correlations of EM field at two points  $\mathbf{x}_1$  and  $\mathbf{x}_2$ . In Eq. (5.1),  $\nu = k \left(\frac{a}{x}\right) d_{12}$  with  $k$  being the central wave number of the quasi-monochromatic radiation,  $a$  the radius of the planar source  $\sigma$  and  $x$  its distance to the Earth. The function  $j(\mathbf{x}_1, \mathbf{x}_2)$  is plotted in Fig. 3 versus the dimensionless parameter  $\nu$ . Starting by complete coherence  $j(\mathbf{x}_1, \mathbf{x}_2) = 1$  at zero separation distance, correlations decrease steadily by increasing the distance between the detectors from  $d_{12} = 0$  to  $d_{12} = (3.83)k^{-1}(x/a)$  where complete incoherence  $j(\mathbf{x}_1, \mathbf{x}_2) = 0$  happens for the first time. Then, the correlation increases again slightly, before vanishing for the second time. Practically, a drop from unity, which does not exceed about 12%, is not regarded as very significant [18]. This happens when  $\nu < 1$ , i.e., for a separation

$$d_{12} < \frac{1}{k} \left(\frac{x}{a}\right) = \frac{2}{k\theta}, \quad (5.2)$$

when correlations get a value 0.88. In the last equality, we replaced the ratio  $a/x$  by  $\theta/2$  which is the angular diameter subtended by the source, when viewed from the Earth (see panel (c) of figure 2). Thus, *in the far zone and close to the direction normal to the source plane and parallel to it, the light produced by a spatially incoherent, quasi-monochromatic, uniform, circular source of radius  $a$  is approximately coherent over a circular area whose diameter is  $\sim \frac{2}{k\theta}$*  (see chapter 4 of [18]). Hence, one may regard the separation length  $d_{\text{coh}} \equiv 2/(k\theta)$  as

a threshold of coherence. For our purposes, we define the dimensionless *coherence parameter* as

$$\alpha_{\text{coh}} \equiv \log(kd_{\text{coh}}) = \log_{10} \left( \frac{2}{\theta} \right), \quad (5.3)$$

We remind that  $d_{12}$  is the transverse coherence length, namely the projected baseline of the VLBI apparatuses. For the typical VLBI setup presented in panel (b) of figure 2, one has  $d_{12} = b \sin \theta_s = \frac{2}{k\theta}$ , where  $\mathbf{b} = \mathbf{x}_1 - \mathbf{x}_2$  denotes the baseline and  $\theta_s$  stands for the angle between the line of sight and the baseline of the interferometer. In the symmetric configuration (panel (c) of figure 2),  $d_{12} = b = |\mathbf{x}_1 - \mathbf{x}_2|$  corresponding to  $\theta_s = 90^\circ$ . In practice, by varying the separation  $\mathbf{b}$  between two telescopes, one monitors the variation of the visibility which gives rise to the measurement of the angular size of the source. Successful measurement of the angular size of distant objects based on visibility implies that the correlation length of the source is at least equal to the projected baseline of the VLBI instrument.

## 5.2 The visibility $\mathcal{V}(\mathbf{x}_P, t)$ in the presence of GWs and definition of incoherence parameter $\alpha^{\text{ts}}(z)$

The presence of GWs can significantly change the visibility of a VLBI measurement given by Eq. (5.1). To understand what happens for the visibility, it is required to generalize the investigation presented in section 4 to the case that the contribution of all wave vectors  $\mathbf{k}$  leaving the source  $\sigma$  is accounted in the intensity  $I(\mathbf{x}_P, t)$  (see App. C). Therefore, the generalized expression of the intensity is determined by Eq. (4.24).

Technically, the visibility at point  $\mathbf{x}_P$  is define as [125]

$$\mathcal{V}(\mathbf{x}_P, t) \equiv \frac{I_{\text{max}}(\mathbf{x}_P, t) - I_{\text{min}}(\mathbf{x}_P, t)}{I_{\text{max}}(\mathbf{x}_P, t) + I_{\text{min}}(\mathbf{x}_P, t)}, \quad (5.4)$$

where  $I_{\text{max}}$  and  $I_{\text{min}}$  stand for the maximum and minimum of the intensity, respectively. Plugging Eq. (4.22) and (4.24) into Eq. (5.4) yields the following expression for the visibility

$$\mathcal{V}(\mathbf{x}_P, t) = \left( \frac{2J_1(\nu)}{\nu} \right) e^{-\left( \frac{d_{12}}{\xi^{\text{vac}}(t)} \right)^2} e^{-\left( \frac{d_{12}}{\xi^{\text{ts}}(t)} \right)^2} \cos \left( \frac{d_{12}}{\delta^{\text{vac}}(t)} \right). \quad (5.5)$$

As before,  $\nu = kd_{12}\theta/2$ . Thus, the presence of PGWs may significantly change the interference pattern. Due to negligibly small coupling strength  $(\hbar\omega_k/E_{\text{P1}})^2 \lll 1$ , both coherent and incoherent dynamics induced by vacuum, that is to say the terms containing  $\delta^{\text{vac}}(t)$  and  $\xi^{\text{vac}}(t)$ , are too feeble to be sensed. For optical field of frequency  $\sim 10^{15}$  Hz, one has  $(\hbar\omega_k/E_{\text{P1}})^2 \sim 10^{-58}$ , thus  $\delta^{\text{vac}}(t), \xi^{\text{vac}}(t) \rightarrow \infty$ , which implies that the vacuum fluctuations of GWs make no change in the visibility. Hence, the effect of two-mode squeezed PGWs appears only as a decaying exponential  $e^{-(d_{12}/\xi^{\text{ts}})^2}$  in the van Citter-Zernike correlations. To quantify the incoherence induced by PGWs and compare it with observational measurements, we define *incoherence parameters* as follows

$$\begin{aligned} \alpha^{\text{vac}}(z) &\equiv \log(k\xi^{\text{vac}}(z)) \\ \alpha^{\text{ts}}(z) &\equiv \log(k\xi^{\text{ts}}(z)), \end{aligned} \quad (5.6)$$

which are dimensionless quantities independent from the EM frequency (see definitions Eq. (4.21)). These parameters contain the blurring of the interference pattern induced by quantum fluctuations of GWs and two-mode squeezed PGWs, respectively. Here, we have implicitly replaced

the time of flight  $t$  with the redshift  $z$ , since we aim at considering objects located at cosmological distances. The relation between the time of flight and the redshift in the flat  $\Lambda$ CDM model is provided in appendix B.3.

If the PGWs background is too strong so that  $\xi^{\text{ts}}(z)$  exceeds the transverse coherence length  $d_{12} = 2/(k\theta)$ , it renders the observation of the interference pattern and the measurement of the angular size of the source almost impossible. This will constitute a coherence criteria, which can be written as  $d_{12} < \xi^{\text{ts}}(z)$ , or equivalently  $kd_{12} < k\xi^{\text{ts}}(z)$ . In terms of the incoherence parameter, the coherence criteria is identified by

$$\alpha_{\text{coh}} < \alpha^{\text{ts}}(z) \quad \Rightarrow \quad \alpha^{\text{ts}}(z) > \log\left(\frac{2}{\theta}\right) \quad (5.7)$$

In the following, VLBI  $\theta - z$  data of quasars observed at redshift range  $0.46 \leq z \leq 2.73$  are used to realize the coherence criteria Eq. (5.7), and consequently infer the tensor-to-scalar ratio  $r_{k_0}$ .

### 5.3 VLBI measurement of the angular size of standard ruler

The angular size-redshift relation for an object of metric size  $\ell_m$  in the flat  $\Lambda$ CDM model (neglecting the radiation fractional energy density  $\Omega_r$ ) is given by [111]

$$\theta(z) = \frac{\ell_m H_0 (1+z)}{c} \left( \int_0^z \frac{dz'}{\sqrt{\Omega_m (1+z')^3 + (1-\Omega_m)}} \right)^{-1}, \quad (5.8)$$

where  $\Omega_m \sim 0.3$  and  $\Omega_\Lambda \sim 0.7$  denote the fractional matter and dark energy densities, respectively [105]. Combining Eq. (5.3) and Eq. (5.8) for the cosmological model of  $\theta(z)$ , the coherence parameter is identified by

$$\alpha_{\text{coh}}(z) \equiv \log\left(\frac{2}{\theta(z)}\right). \quad (5.9)$$

Recently, a set of 120 milliarcsec. compact radio sources representing intermediate-luminosity quasars covering the redshift range  $0.46 \leq z \leq 2.76$  has been investigated to check the possibility of using them as independent cosmological probes. These quasars observed at 2.29 GHz show negligible dependence on redshift and intrinsic luminosity, and thus represent a fixed comoving-length of standard ruler. It is indeed found that compact structure in the intermediate-luminosity radio quasars could serve as a standard cosmological ruler and could thus provide valuable sources of angular diameter distances at high redshifts ( $z \sim 3.0$ ) [90]. This new approach is recently used to demonstrate that using these standard rulers could be helpful in understanding the current cosmological issues concerning the Hubble tension and cosmic curvature tension [92, 126], even if the precision is not yet sufficient compared to other standard ruler (CMB acoustic peak or baryon acoustic oscillations). What makes the use of these objects significant for us lies in the fact that these observations are made based on the VLBI technique, i.e., spatial correlations in the light coming from very distant radio quasars, observed on the Earth.

Using a compilation of angular size-redshift data for ultra-compact radio sources from a well-known VLBI survey, the linear size of this standard ruler turns out to be  $\ell_m = 11.03 \pm 0.25$  pc, which is the typical radius at which AGN jets become opaque at the observed frequency  $\omega_k \sim 2$  GHz. Here, we make use of the sample of 120 radio-quasars described in



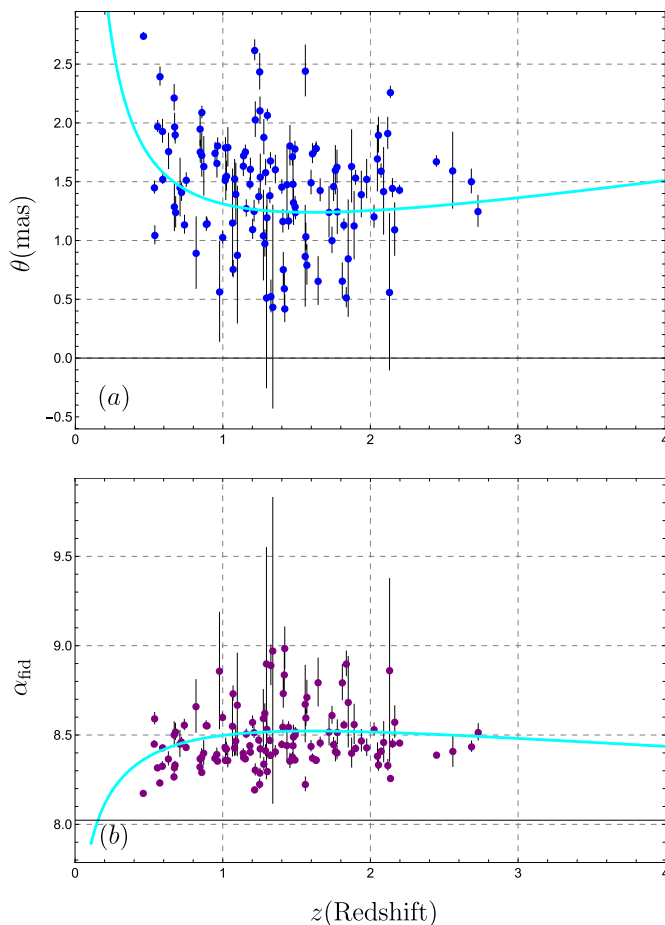


**Figure 4.** *Panel (a):* the scatter plot of angular sizes  $\theta$  of 120 compact radio quasars based on the data given in Table. 1 of Cao et al [90]. The cyan line represents the fit  $\theta(z)$  as given by Eq. (5.8) with a standard ruler given by  $\ell_m = 11.03$  pc [92], as computed for a flat  $\Lambda$ CDM model with  $H_0 = 67.4$  km s $^{-1}$  Mpc $^{-1}$  and  $\Omega_m = 0.3$  (adopted from the Planck results [105]). *Panel (b):* purple points show the coherence parameter  $\alpha_{\text{coh}}$  based on  $\theta - z$  data given in panel (a), and the cyan curve is a representation of the coherence parameter  $\alpha_{\text{coh}}(z) = \log\left(\frac{2}{\theta(z)}\right)$  corresponding to panel (a).

[90, 91, 127]. The scatter diagram of the observed angular size for 120 radio quasars is shown in panel (a) of figure. 4. In this figure, the cyan line corresponds to fiducial  $\Lambda$ CDM model for  $\theta(z)$ , given by Eq. (5.8), with  $H_0 = 67.4$  km s $^{-1}$  Mpc $^{-1}$  and  $\Omega_m = 0.3$  adopted from the Planck results [105]. Moreover, the linear size of the standard ruler  $\ell_m = 11.03$  pc is adopted [92]. Panel (b) of figure 4 is a representation of the coherence parameter  $\alpha_{\text{coh}} = \log\left(\frac{2}{\theta(z)}\right)$  and the fit in cyan considering each quasar to be a standard ruler of size  $\ell_m = 11.03$  pc.

In the rest of the paper, we use the coherence criteria Eq. (5.7) in order to put constraint on the PGWs parameters, specially the tensor-to-scalar ratio  $r_{k_0}$ .

#### 5.4 VLBI constraint on tensor-to-scalar ratio $r_{k_0}$

We first examine the incoherence induced by vacuum fluctuations, given by the first equation in Eq. (5.6). With the help of Eq. (4.21) and Eq. (B.15),  $\alpha^{\text{vac}}(z)$  can be written as follows

$$\begin{aligned} \alpha^{\text{vac}}(z) = & \log \left( \left[ \frac{1}{2(2\pi)^2} \left( \frac{\hbar c}{E_{\text{Pl}}(1+z)} \right)^2 \int_0^{2\pi} d\Phi_K \int_0^\pi d\Theta_K \sin^7 \Theta_K \right. \right. \\ & \left. \left. \times \int_{K_E}^{K_1} dK \left( 4K \sin^2 \left( \frac{\Omega_K t(z)}{2} \right) \right) \right]^{-1/2} \right). \end{aligned} \quad (5.10)$$

where  $\omega_k \rightarrow \omega_k/(1+z)$  is substituted to account for the gravitational redshift of the EM frequency during its journey to the Earth (see Sec. 3.1). The plot of  $\alpha^{\text{vac}}(z)$  is represented in figure 5, panel (a) versus the time-of-flight in  $(H_0 t)$  scale, and in panel (b) versus the redshift  $z$ . As one expects, it starts from high values at small  $(H_0 t)$  (remind that  $\alpha^{\text{vac}} \rightarrow \infty$  when  $t \rightarrow 0$ ), decreases monotonically to get stabilize at a value of  $\alpha^{\text{vac}} \sim 61$  at large time-of-flight  $H_0 t \gtrsim 1$ , namely  $t \gtrsim H_0^{-1}$ , which is as long as the age of the Universe. At low redshift (corresponding to small  $t$ ),  $\alpha^{\text{vac}}(z)$  decreases with increasing  $z$ . It reaches to the minimal value of  $\sim 61$  at  $z \sim 0.6$  and starts growing with increasing  $z$ . Comparing  $\alpha^{\text{vac}}(z)$  with the fit of  $\alpha_{\text{coh}}(z) = \log \left( \frac{2}{\theta(z)} \right)$  which is shown by cyan curve in panel (b) of figure 4, one might check that  $\alpha^{\text{vac}} \gg \alpha_{\text{coh}}$ , or equivalently  $\xi^{\text{vac}} \gg d_{\text{coh}}$ . More precisely, it can be deduced that  $\frac{\xi^{\text{vac}}}{d_{12}} \Big|_{z \gtrsim 1} \sim e^{52.2} \sim 10^{22}$ . As a result, the blurring effect caused by vacuum fluctuations of GWs is not detectable by VLBI means.

On the other hand, the incoherence induced by two-mode squeezed PGWs is encapsulated in  $\alpha^{\text{ts}}(z)$  given by the second equation in Eq. (5.7). To visualize the behaviour, we first assume that the modes are highly-squeezed, i.e.,  $r_K \gg 1$ . Thus, one has  $\bar{n}_{\text{ts}}(K) = \sinh^2 r_K \simeq e^{2r_K}/4$  and  $\sinh 2r_K \simeq e^{2r_K}/2$ . One then gets for this highly-squeezed PGWs

$$\begin{aligned} \alpha^{\text{ts}}(z) = & \log \left( \left[ \frac{1}{(2\pi)^2} \left( \frac{\hbar c}{E_{\text{Pl}}(1+z)} \right)^2 \int_0^{2\pi} d\Phi_K \int_0^\pi d\Theta_K \sin^7 \Theta_K \int_{K_E}^{K_1} dK \left( \frac{K e^{2r_K}}{4} \right) \right. \right. \\ & \left. \left. \times 8 \sin^2 \left( \frac{\Omega_K t(z)}{2} \right) \sin^2 \left( \frac{\Omega_K t(z) - 2\phi_K(\eta_H)}{2} \right) \right]^{-1/2} \right). \end{aligned} \quad (5.11)$$

In comparison with  $\alpha^{\text{vac}}(z)$ , not only the incoherence mechanism is amplified as a result of high number of gravitons (implied by  $e^{2r_K}/4$  factor), but also the time behaviour is modified by the appearance of the new oscillating factor  $\sin^2 \left( \frac{\Omega_K t(z) - 2\phi_K(\eta_H)}{2} \right)$ . Generally, for a given value of the redshift  $z$ , the term  $\Omega_K t(z) = 2\phi_K(\eta_H)$  happening for some specific values of  $\Omega_K$ , leads the oscillating factor to vanish, so the contribution of those modes in integration. As a result,  $\alpha^{\text{ts}}$  might take a larger value. In this way, the incoherence induced by two-mode squeezed PGWs may get attenuated as a result of non-vanishing  $\phi_K$ . However, in the following discussion, we assume  $\phi_K = 0$  which allows the contribution of all PGWs modes in the integral Eq. (5.11) to be accounted, hence leads to the most-stringent upper bound on tensor-to-scalar ratio. Thus, incorporating  $\phi_K \neq 0$  may relieve the following constraint. For vanishing squeezing phase  $\phi_K = 0$ , Eq. (5.11) further reduces to

$$\begin{aligned} \alpha_{\phi_K=0}^{\text{ts}}(z) = & \log \left( \left[ \frac{1}{(2\pi)^2} \left( \frac{\hbar c}{E_{\text{Pl}}(1+z)} \right)^2 \int_0^{2\pi} d\Phi_K \int_0^\pi d\Theta_K \sin^7 \Theta_K \right. \right. \\ & \left. \left. \times \int_{K_E}^{K_1} dK \left( \frac{K e^{2r_K}}{4} \right) 8 \sin^4 \left( \frac{\Omega_K t(z)}{2} \right) \right]^{-1/2} \right). \end{aligned} \quad (5.12)$$

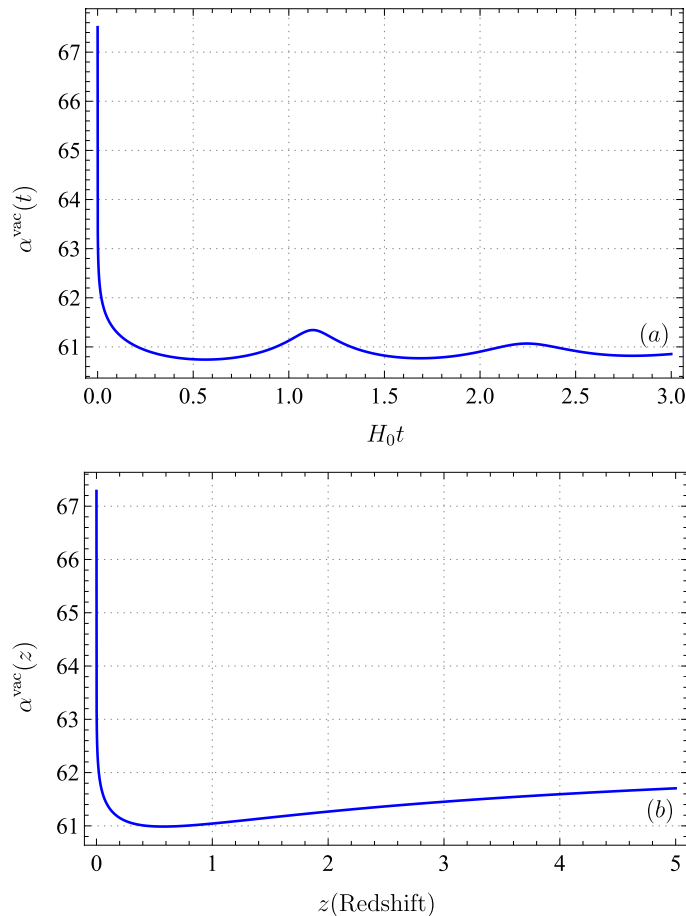


**Figure 5.** *Panel (a):* the incoherence parameter  $\alpha^{\text{vac}}(t)$  versus the time-of-flight in  $(H_0 t)$  scale; *Panel (b):* the incoherence parameter  $\alpha^{\text{vac}}(z)$  versus redshift  $z$ , based on Eq. (5.10).

Fig. 6 shows the plot of  $\alpha_{\phi_K=0}^{\text{ts}}(z)$  versus redshift, based on Eq. (5.12). Here, the expression Eq. (2.17) for  $e^{r_K(\eta_H)}$  has been used, where  $\beta_s = 1$  and  $T_{\text{reh}} = 10^8$  Gev are fixed and different values of  $\beta$  and  $r_{k_0}$  are chosen. The cyan curve shows the fit of the coherence parameter  $\alpha_{\text{coh}}(z)$  for standard ruler with size  $\ell_m = 11.03$  pc. The coherence criteria  $\alpha^{\text{ts}}(z) > \alpha_{\text{coh}}(z)$  (or equivalently  $\xi^{\text{ts}} > d_{\text{coh}}$ ) is violated for the blue curve for which  $r_{k_0} = 0.032 \sim 10^{-1.5}$ , corresponding to the combination of Planck with BK18 and baryon-acoustic-oscillation [128]. Green curve corresponds to a reduced tensor-to-scalar ratio  $r_{k_0} = 10^{-7}$ , where the coherence criteria is met. In this case, changing  $\beta = -2$  to  $\beta = -1.9$  shifts up the curve only slightly, as shown by the dashed-green curve. Generally, reducing and increasing the tensor-to-scalar ratio  $r_{k_0}$  drastically shifts the curve  $\alpha^{\text{ts}}(z)$  up and down, respectively, while changing  $\beta$  shifts the curves only slightly. Since  $e^{2r_K} \propto A^2 \propto r_{k_0}$  (see Eq. (2.17) and (2.18)), Eq. (4.21) implies that  $\xi^{\text{ts}} \propto r_{k_0}^{-1/2}$ . Hence, this scaling implies that a reduction of the tensor-to-scalar ratio leads the incoherence length  $\xi^{\text{ts}}(z)$  to increase, since PGWs leave a smaller effect on spatial correlations of the EM field.

Note that, here we use the coherence criteria  $\xi^{\text{ts}} > d_{\text{coh}}$ , which implies the criteria  $e^{-\left(\frac{d_{\text{coh}}}{\xi^{\text{ts}}}\right)^2} > e^{-1}$  on the visibility. However, one could define a slightly stronger coherence

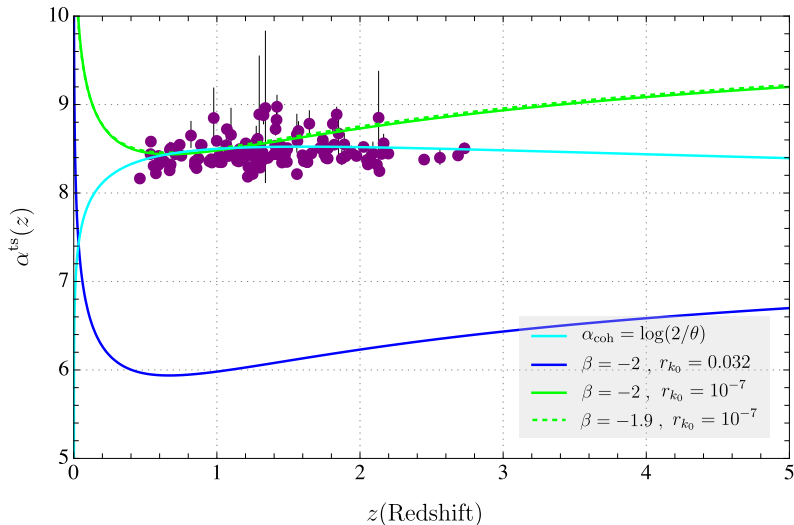


**Figure 6.** The incoherence parameter  $\alpha^{\text{ts}}(z)$  versus redshift  $z$ , based on Eq. (5.12). The blue curve corresponds to  $\beta = -2$  and  $r_{k_0} = 0.032 \sim 10^{-1.5}$  coming from the combination of Planck with BK18 and baryon-acoustic-oscillation [128]. The green and dashed curves correspond to  $\beta = -2, r_{k_0} = 10^{-7}$  and  $\beta = -1.9, r_{k_0} = 10^{-7}$ , respectively. The purple points show  $\alpha_{\text{coh}}(z)$  based on the measured  $\theta - z$  using VLBI, and the cyan curve represents  $\alpha_{\text{coh}}(z)$  based on Eq. (5.9) for standard ruler with size  $\ell_m = 11.03$  pc. The green curve respects the coherence criteria Eq. (5.7), i.e.,  $\alpha^{\text{ts}}(z) > \alpha_{\text{coh}}(z)$  or equivalently  $\xi^{\text{ts}} > d_{\text{coh}}$ . This puts the upper limit  $r_{k_0} \lesssim 10^{-7}$  on the tensor-to-scalar ratio.

criteria such that the visibility reaches 1%, i.e.,  $e^{-\left(\frac{d_{\text{coh}}}{\xi^{\text{ts}}}\right)^2} > 10^{-2}$ . In this case, one has  $\xi^{\text{ts}} > d_{\text{coh}}/\sqrt{2}$  or equivalently  $\alpha_{\text{coh}} \rightarrow \log\left(\frac{2}{\sqrt{2}\theta}\right)$ , which is smaller than  $\log\left(\frac{2}{\theta}\right)$  to some degree. In this case, the cyan curve in figure 6 slightly shifts down, giving rise to a relieved constraint on  $r_{k_0}$ .

The current constraint on the tensor-to-scalar ratio coming from the combination of Planck with BK18 and baryon-acoustic-oscillation is  $r_{k_0} < 0.032$  [128]. However, recent measurements of the European pulsar timing array (EPTA) are compatible with excessively small values  $r_{k_0} \sim 10^{-12.1}$  [129]. Figure 7 shows the 2D posteriors of the tensor-to-scalar ratio (in  $\log_{10}$ ) and the fractional energy density spectral index  $n_T$  in the PTA observations at the nanohertz working frequency [129]. The 68% and 95% credible regions are displayed. The black dashed line represents the tensor-to-scalar ratio upper bound  $r_{k_0} = 0.032 \sim 10^{-1.5}$  found by Planck combined with BK18 and baryon-acoustic-oscillation [128] assuming single-field slow-roll inflation. The solid green line corresponds to the upper bound  $r_{k_0} \sim 10^{-7}$  based on VLBI  $\theta - z$  measurement, found in this study. Consequently, the present constraint  $r_{k_0} \lesssim 10^{-7}$  based on VLBI  $\theta - z$  measurements is compatible with the inferred value from EPTA if the detected GW background is indeed the primordial GW background.

## 6 Further discussion and results

### 6.1 Implications for the slow-roll framework

We have seen that PGWs induced-incoherence may put constraint on the inflationary parameter  $r_{k_0}$  while the reheating parameters such as  $(\beta_s, \zeta_1, T_{\text{reh}})$  are not sensible by this method as described before. Although we have presented the method in a model-independent manner,

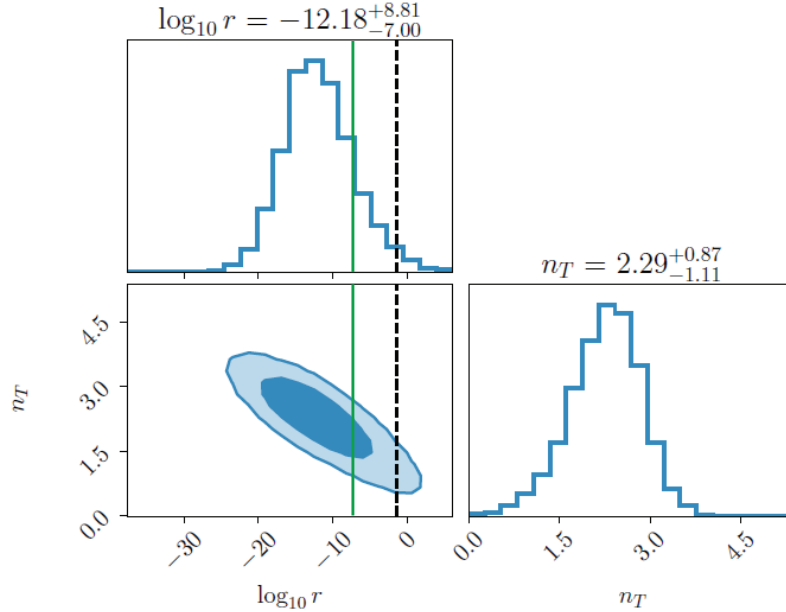


**Figure 7.** 2D posteriors of the tensor-to-scalar ratio (in  $\log_{10}$ ) and the fractional energy density spectral index  $n_T$  in the PTA observations (figure extracted from [129]). The 68% and 95% credible regions are displayed. The black dashed line represents the tensor-to-scalar ratio upper bound  $r_{k_0} = 0.032 \sim 10^{-1.5}$  found by Planck combined with BK18 and baryon-acoustic-oscillation [128] and the solid green line corresponds to the upper bound  $r_{k_0} \sim 10^{-7}$  based on VLBI  $\theta - z$  measurement, found in the present study.

specific models describing the inflationary epoch can be addressed straightforwardly. General inflationary parameters such as  $r_{k_0}$ ,  $\beta$ ,  $n_s$  and  $n_T$  are expressible in terms of the slow-roll parameters within a given inflationary model with specific potential  $V(\phi)$ . Hence, the coherence criteria based on  $\theta - z$  observations may put constraint on the model parameters. However, the stringent upper bound  $r_{k_0} \lesssim 10^{-7}$  which was obtained in a model-independent manner, holds true and implies extremely small values for the (first order) slow-roll parameter  $\epsilon_V$ .

Generally, under the first order slow-roll approximation, tensor and scalar spectral tilts are determined by  $n_T \simeq -2\epsilon_V$  and  $n_s - 1 \simeq 2\eta_V - 6\epsilon_V$ , where  $\epsilon_V$  and  $\eta_V$  are the slow-roll parameters which depend on the specific form of the inflationary potential  $V(\phi)$ . Assuming the initial tensor spectrum  $h(k_0, \eta_i) = A(k_0/K_H)^{2+\beta}$  constitutes tensor perturbation at pivot scale,  $A_T(k_0)$ , one obtains the relation  $n_T = 2\beta + 4$ [108]. Hence, a general (model-independent) results is the relation between  $\epsilon_V$  and  $\beta$  given by  $\epsilon_V = -\beta - 2$ . Note that according to definition,  $\epsilon_V > 0$  so that  $\beta < -2$ . Moreover, the single-field slow-roll inflation predicts  $r = -8n_T = 16\epsilon_V = -16(\beta + 2)$ . Hence, the constraint  $r_{k_0} \lesssim 10^{-7}$  implies upper bound on the slow-roll parameter such that  $\epsilon_V \lesssim 6.25 \times 10^{-9}$  and  $|n_T| \lesssim 1.25 \times 10^{-8}$ . Such small values for  $r_{k_0}$  and  $\epsilon_V$  are compatible with prediction of some specific inflationary models [130]. Hence, knowledge of upper bounds on slow-roll parameters based on VLBI method may rule out inflationary models or put stringent constraint on the model parameters. On the experimental side, while Planck collaboration combined with BK18 and baryon-acoustic-oscillation place a limit on the tensor-to-scalar ratio  $r_{k_0} \lesssim 0.032$  [128], recent measurements of the European pulsar timing array (EPTA) are compatible with much smaller values  $r_{k_0} \sim 10^{-12.1}$  [129]. Consequently, the constraint  $r_{k_0} \lesssim 10^{-7}$  stemming from VLBI is compatible with the possible

detection of a relic GW background with EPTA [129].

## 6.2 Comparison between different quantum states of PGWs and possible quantum-to-classical transition issue

For the sake of completeness, it is instructive to investigate the effect of GWs in other quantum states, on the spatial correlations of the EM field. Appendix D is dedicated to calculation of the incoherence parameter in the presence of vacuum fluctuations as well as thermal gravitons of GWs. Here, we emphasize on final results and conclusions:

1. *Thermal state* of GWs leads only to the blurring of the visibility, almost identical to the two-mode squeezed state. The decay of the visibility depends on the graviton number in thermal state, namely  $\bar{n}_{\text{th}}(K)$ . To evaluate the effect, we consider the same mean number of gravitons as in two-mode squeezed state,  $\bar{n}(K) \simeq e^{2r\kappa(\eta_H)}/4$ . The coherence criteria then implies a slightly relieved upper bound on tensor-to-scalar ratio,  $r_{k_0} \lesssim 10^{-6.8}$ .
2. *Squeezed state* of GWs leads only to the blurring of the visibility, almost equal to the two-mode squeezed state and thermal state, as long as they possess the same graviton content,  $\bar{n}(K) \simeq e^{2r\kappa(\eta_H)}/4$ . Although, the spatio-temporal dependence of the EM correlation function is slightly different from that of two-mode squeezed state, stemming from different correlations between gravitons in two-mode squeezed state, which are absent in (one-mode) squeezed state. Finally, the coherence criteria then implies a slightly relieved upper bound on tensor-to-scalar ratio,  $r_{k_0} \lesssim 10^{-6.8}$ , very similar to thermal GW.
3. So far, it turns out that the highly-correlated highly-populated two-mode squeezed PGWs leave the most severe effect on the phase-correlations of EM field, leading to the most stringent constraint on  $r_{k_0}$ . However, possible decoherence of PGWs may change the result. Basically, in a given decoherence schema for PGWs, it is crucial to follow the dynamics of the *mean number of gravitons* and *quantum correlations between gravitons* in the course of Universe expansion, encoded in the diagonal and off-diagonal density matrix elements  $\rho_{\text{PGWs}}^{mn}(\eta)$  in the Fock space representation. Possible decaying of the density matrix elements due to decoherence mechanism, especially in the ultra-low frequency band of PGWs, may significantly reduce the incoherence of EM field that results in a less stringent upper bound on the tensor-to-scalar ratio  $r_{k_0}$ . In particular, decay of the diagonal elements that corresponds to decay of the mean number of gravitons, leads to weaker EM-GWs, and relieves the constraint on  $r_{k_0}$ . Hence, investigating the effect of PGWs decoherence initiated from different mechanisms on phase correlations of light deserves further study that can be addressed within the presented formalism. The main goal of the present study is to introduce and evaluate a new way to look forward quantum gravitational effects by means of the well-established VLBI techniques, and to infer the corresponding model parameters based on that [115, 131].

## 7 Summary and conclusion

In a nutshell, this work promotes the idea of using gravitational induced spatial incoherence of the EM field radiated from distant objects, as a new approach to probe the inflationary

Universe. We theoretically investigated spatial coherence of the EM field emitted from distant objects interacting with the background of primordial gravitational waves which encodes historical features of the expanding Universe in itself. It turns out that spatial correlation of the EM field, which in the absence of PGWs is simply governed by the van Citter-Zernike theorem, is modified by the presence of PGWs such that the transverse separation  $d_{12}$  between two telescopes in the VLBI can not exceed a characteristic length-scale  $\xi^{\text{ts}}(z)$  defined by Eq. (4.21), otherwise the interference vanishes. However, successful observation of the visibility pattern in VLBI experiments implies that  $\xi^{\text{ts}}$  must be larger than the projected baseline of the VLBI. A coherence criteria has been defined based on the van-Citter-Zernike theorem which relates the spatial coherence of the source,  $d_{\text{coh}}$ , to its angular size  $\theta(z)$ . We used the angular size-redshift relation  $\theta-z$  of 120 radio AGNs located at redshift range  $0.46 \leq z \leq 2.73$  to define the coherence parameter,  $\alpha_{\text{coh}}(z) \equiv \log(2/\theta(z))$  (see Eq. (5.9)), based on which the two-mode squeezed PGWs induced-incoherence can be constrained. It turns out that the coherence criteria  $\alpha^{\text{ts}}(z) > \alpha_{\text{coh}}(z)$  exerts stringent upper bound on the tensor-to-scalar ratio  $r_{k_0} \lesssim 10^{-7}$  as well as on the first-order slow-roll parameter  $\epsilon_V \lesssim 6.25 \times 10^{-9}$  under the slow-roll paradigm. Hence, it is found that the present method can be used to put constraint on specific inflationary model parameters. The aim of the present study is to highlight the capability of interferometric methods, in particular the very long baseline interferometry technique, to put constraint on the inflationary Universe by means of gravitational induced incoherence of EM field. Altogether, VLBI method seem promising to be used as an observatory to search for quantum features of spacetime.

## 8 Supplementary materials

### A PGWs spectrum and related parameters

#### A.1 Increase parameters $\zeta_E, \zeta_2, \zeta_s, \zeta_1$

In the  $\Lambda$ CDM framework, one can show that the increase parameter during  $\Lambda$ -dominated stage is given by

$$\zeta_E = 1 + z_E = (\Omega_\Lambda/\Omega_m)^{1/3} \simeq 1.33, \quad (\text{A.1})$$

given the current values  $\Omega_\Lambda \sim 0.7$  and  $\Omega_m \sim 0.3$ . Here,  $z_E$  is the redshift at the matter-dark energy equality. The increase factor at matter-radiation equality is

$$\zeta_2 = (1 + z_{\text{eq}}) \zeta_E^{-1} \simeq 2547, \quad (\text{A.2})$$

where  $z_{\text{eq}} = 3387$  [105]. The increase of scale factor during the reheating, namely  $\zeta_s$ , depends on the reheating temperature  $T_{\text{reh}}$  through [108]

$$\zeta_s = \frac{T_{\text{reh}}}{T_{\text{CMB}}(1 + z_{\text{eq}})} \left( \frac{g_{*s}}{g_{*\star}} \right)^{1/3}, \quad (\text{A.3})$$

where  $T_{\text{CMB}} = 2.348 \cdot 10^{-13}$  GeV [132]. Here,  $g_{*s}$  and  $g_{*\star}$  count the effective number of relativistic species contributing to the entropy during the reheating and recombination, respectively, and will be taken  $g_{*s} \simeq 200$  and  $g_{*\star} = 3.91$  [133], as was also employed in [108]. Moreover, under the quantum normalization condition, the increase parameter  $\zeta_1$  is expressed in terms of  $\zeta_s, \zeta_2, \zeta_E$  according to Eq. (2.19).



## A.2 Spectral amplitude of PGWs

The dimensionless *spectral amplitude* of PGWs,  $h(k, \eta)$  is usually defined by [98]

$$\int_{K_E}^{K_1} h^2(K, \eta) \frac{dK}{K} \equiv \langle \text{TS}(\eta) | \hat{h}_{ij}(\mathbf{x}, \eta_{\text{ini}}) \hat{h}^{ij}(\mathbf{x}, \eta_{\text{ini}}) | \text{TS}(\eta) \rangle, \quad (\text{A.4})$$

where the r.h.s is the variance of the field in the two-mode squeezed state and  $\hat{h}_{ij}(\mathbf{x}, \eta_{\text{ini}})$  is given by Eq. (2.9). Note that, as we discussed in Sec. (2.2), in Schrödinger picture the evolution of perturbations are included in the state of the system, while the field operator is given by its initial expression. Moreover, the lower and upper limits of the integral are considered as  $K_{\text{low}} = K_E$  and  $K_{\text{up}} = K_1$ . Inserting Eq. (2.9) into Eq. (A.4) and with the help of Eqs. (2.10 - 2.13), one may straightforwardly show that

$$h(K, \eta) = \frac{4\ell_{\text{Pl}}}{\sqrt{\pi}a(\eta)} K \left( |u_K(\eta)|^2 + |v_K(\eta)|^2 + u_K(\eta)v_K(\eta) + u_K^*(\eta)v_K^*(\eta) \right)^{1/2}. \quad (\text{A.5})$$

where the functions  $u_K(\eta)$  and  $v_K(\eta)$  are given by Eq. (2.13) with the initial conditions  $u_K(\eta_{\text{ini}}) = 1$  and  $v_K(\eta_{\text{ini}}) = 0$  [110]. Thus, using the expression Eq. (A.5), one may find the evolution of the spectral amplitude  $h(K, \eta)$  readily, as soon as the evolution of the functions  $u_K(\eta)$  and  $v_K(\eta)$  are determined. Another important application of Eq. (A.5) is to build the relationship between the squeezing parameters  $(r_k, \phi_k)$  and the spectral amplitude  $h(K, \eta)$ . Especially, by substitution of Eq. (2.13) for the functions  $u_K$  and  $v_K$  into Eq. (A.5) and assuming  $r_K \gg 1$  for super-Hubble modes ( $K \leq 2\pi\mathcal{H}$ ), one obtains the following relationship

$$h(K, \eta) = 8\sqrt{\pi} \left( \frac{\ell_{\text{Pl}}}{\ell_H} \right) \left( \frac{K}{K_H} \right) e^{r_K(\eta)} \cos \phi_K(\eta). \quad (\text{A.6})$$

Eq. (A.6) is in accordance with Eq. (31) of [22]. Note that, according to Eq. (2.14), the variable  $\phi_k$  is not an independent variable and its dynamics is determined once the dynamics of  $r_K$  is specified. Hence, the evolution of  $h(K, \eta)$  can be solely given by the evolution of the squeezing amplitude  $r_K$ . Inversely, one may obtain the approximate expression of the squeezing factor  $e^{r_K}$  from  $h(K, \eta)$  according to

$$e^{r_K(\eta)} = \frac{1}{8\sqrt{\pi}} \left( \frac{\ell_H}{\ell_{\text{Pl}}} \right) \left( \frac{K_H}{K} \right) h(K, \eta). \quad (\text{A.7})$$

in the super-Hubble regime, where the oscillatory factor  $\cos \phi_k$  tends to 1 (see Eq. (2.15)). On the other hand, one may show that  $h(K, \eta)$  is related to the Fourier field amplitude  $h_{\mathbf{K}}(\eta)$  (defined in Eq. (2.3)) by the following relation

$$h(K, \eta) = \frac{4\ell_{\text{Pl}}K}{\sqrt{\pi}} \sqrt{\frac{2K}{\hbar}} |h_{\mathbf{K}}(\eta)|. \quad (\text{A.8})$$

Note that, definition of  $h_{\mathbf{K}}(\eta)$  is occasionally different with Eq. (2.3) in a  $\sqrt{2K}$  factor. In some references, the prefactor  $1/\sqrt{2K}$  is included in the field expansion Eq. (2.3), while in others this prefactor is implied in the temporal mode functions  $h_{\mathbf{K}}^\gamma(\eta)$ . Here, we adopted the second notation. As a result of Eq. (A.8), the spectral amplitude could also be found by solving the equation of motion for  $h_{\mathbf{K}}(\eta)$  given by Eq. (2.7). Especially, one may show that during the long wavelength regime, the spectral amplitude  $h_{\mathbf{K}}(\eta)$  (and  $h(K, \eta)$ ) stay constant.

In this manner, approximate solutions for  $h(K, \eta)$  is found in super-Hubble regime. It turns out that the spectral amplitude is determined by [99]

$$h(K, \eta) = \begin{cases} A \left( \frac{K}{K_H} \right)^{2+\beta} & , \quad K \leq K_E \\ A \left( \frac{K}{K_H} \right)^{\beta-\gamma} \zeta_E^{-\frac{2+\gamma}{\gamma}} & , \quad K_E \leq K \leq K_H \\ A \left( \frac{K}{K_H} \right)^{\beta} \zeta_E^{-\frac{2+\gamma}{\gamma}} & , \quad K_H \leq K \leq K_2 \\ A \left( \frac{K}{K_H} \right)^{1+\beta} \left( \frac{K_H}{K_2} \right) \zeta_E^{-\frac{2+\gamma}{\gamma}} & , \quad K_2 \leq K \leq K_s \\ A \left( \frac{K}{K_H} \right)^{1+\beta-\beta_s} \left( \frac{K_s}{K_H} \right)^{\beta_s} \left( \frac{K_H}{K_2} \right) \zeta_E^{-\frac{2+\gamma}{\gamma}} & , \quad K_s \leq K \leq K. \end{cases} \quad (\text{A.9})$$

where the coefficient  $A$  is discussed in Sec. 2.3.

### A.3 Characteristic wave numbers $K_E, K_H, K_2, K_s$ and $K_1$

The comoving wave number at a given jointing time  $\eta_x$  is defined as  $K_x \equiv K(\eta_x) = 2\pi\mathcal{H}(\eta)$ , assuming the wave mode crosses the horizon when  $\lambda = 1/\mathcal{H}$  with  $\mathcal{H}$  being the Hubble radius (this definition for horizon-crossing is also used in [22, 104]). Thus  $K_H = 2\pi\mathcal{H}(\eta_H) = 2\pi\gamma$  is the comoving Hubble wave number. The physical wave number at the present is related to the comoving wave number  $K$  according to  $K^{\text{ph}} = K/a(\eta_H) = K/\ell_H$ . Hence,  $K_H^{\text{ph}} = 2\pi\gamma/\ell_H = 2\pi H_0/c$  with  $H_0$  being today Hubble frequency. One can show that characteristic wave numbers at different jointing points  $\eta_1, \eta_s, \eta_2$  and  $\eta_E$  are related to the increase parameters according to [98]

$$\frac{K_E}{K_H} = \zeta_E^{-\frac{1}{\gamma}} \quad , \quad \frac{K_2}{K_E} = \zeta_2^{\frac{1}{2}} \quad , \quad \frac{K_s}{K_2} = \zeta_s \quad , \quad \frac{K_1}{K_s} = \zeta_1^{\frac{1}{1+\beta_s}}. \quad (\text{A.10})$$

Similar expressions hold for the PGWs frequencies,  $\Omega_K = cK$ . Given  $H_0 = 67.4 \text{ km s}^{-1} \text{ Mpc}^{-1}$  one has  $K_H^{\text{ph}} \sim 4.52 \times 10^{-26}$ ,  $K_E^{\text{ph}} = 3.4 \times 10^{-26}$  and  $K_2 = 1.71 \times 10^{-24}$  in  $m^{-1}$  units. The values of  $K_s$  and  $K_1$ , corresponding to waves that crossed the horizon at the end of the reheating and inflationary stages respectively, are determined by  $(\zeta_s, \zeta_1, \beta_s)$ . For  $T_{\text{reh}} = 10^8 \text{ GeV}$ ,  $K_s = 7.9 \text{ m}^{-1}$  and  $K_1$  depends also on the values of  $(\beta, r_{k_0})$  through Eq. (2.19). For  $\beta = -2$  and  $r_{k_0} = 10^{-1.5}$  adopted in this study, one has  $K_1 = 0.08 \text{ m}^{-1}$ .

Basically,  $\beta_s$  and  $T_{\text{reh}}$  determine characteristic features of the expanding Universe during the reheating stage, so they only affect the frequencies  $\Omega_s$  and  $\Omega_1$ , e.g., waves re-entering the horizon during the reheating stage (see panel (a, b) of figure 1). However, the main contribution in incoherence mechanism comes from ultra-low frequency PGWs, say  $\Omega_K \leq \Omega_s$ , which possess higher squeezing amplitudes. Throughout the paper, unless it is stated, we mostly take  $\beta_s = 1$  and  $T_{\text{reh}} = 10^8 \text{ GeV}$  in our calculations.

The value of upper frequency of PGWs,  $\Omega_{K_1} = cK_1$ , depends on the choice of the increase parameter  $\zeta_1$ . Modes with frequency higher than  $\Omega_{K_1}$  has been decayed by the expansion of the universe and have not been squeezed at all. In any case, the value of  $\Omega_{K_1}$  should be below the constraint from the rate of the primordial nucleosynthesis, i.e.,  $\Omega_{K_1} \lesssim 10^{10} \text{ Hz}$  [108, 116], which is the case in our study.

## B Preliminaries for evaluation of $g_{\text{ts}}^{(1)}(\mathbf{x}_1, t, \mathbf{x}_2, t)$

### B.1 Evaluation of the integral $\int d^3\mathbf{K}\kappa_\gamma^2(\mathbf{K}, \mathbf{k})$

One of the main quantities that appear frequently in our calculations, is the expression

$$\sum_\gamma \int d^3\mathbf{K}\kappa_\gamma^2(\mathbf{K}, \mathbf{k}) \quad (\text{B.1})$$

To evaluate Eq. (B.1), we consider a surface element  $d\sigma$  that emits EM radiation in direction

$$\hat{\mathbf{k}} = (\sin \theta_{\mathbf{k}}/2 \cos \phi_{\mathbf{k}}, \sin \theta_{\mathbf{k}}/2 \sin \phi_{\mathbf{k}}, \cos \theta_{\mathbf{k}}), \quad (\text{B.2})$$

where  $0 \leq \theta_{\mathbf{k}} \leq \theta$  and  $0 \leq \phi_{\mathbf{k}} \leq 2\pi$  represent spatial angles of the EM wave vector, as shown in figure 8. One has

$$\begin{aligned} F_\gamma(\hat{\mathbf{K}}, \hat{\mathbf{k}}) &= k_i k_j e_{ij}^\gamma[\hat{\mathbf{K}}] \\ &= e_{11}^\gamma[\hat{\mathbf{K}}] \sin^2 \theta_{\mathbf{k}}/2 \cos^2 \phi_{\mathbf{k}} + e_{12}^\gamma[\hat{\mathbf{K}}] \sin^2 \theta_{\mathbf{k}}/2 \sin 2\phi_{\mathbf{k}} + e_{13}^\gamma[\hat{\mathbf{K}}] \sin \theta_{\mathbf{k}} \cos \phi_{\mathbf{k}} \\ &\quad + e_{22}^\gamma[\hat{\mathbf{K}}] \sin^2 \theta_{\mathbf{k}}/2 \sin^2 \phi_{\mathbf{k}} + e_{23}^\gamma[\hat{\mathbf{K}}] \sin \theta_{\mathbf{k}} \sin \phi_{\mathbf{k}} + e_{33}^\gamma[\hat{\mathbf{K}}] \cos^2 \theta_{\mathbf{k}}/2. \end{aligned} \quad (\text{B.3})$$

Typical angular size of distant quasars is of order  $\mathcal{O}(\theta) \sim 10^{-8}$  [90]. The quantity of interest is  $F_\gamma^2(\mathbf{K}, \mathbf{k})$ . Calculations up to  $\mathcal{O}(\theta_{\mathbf{k}}^2)$  yields

$$\begin{aligned} F_\gamma(\hat{\mathbf{K}}, \hat{\mathbf{k}}) &= e_{33}^\gamma[\hat{\mathbf{K}}] + \theta_{\mathbf{k}} \left( e_{13}^\gamma[\hat{\mathbf{K}}] \cos \phi_{\mathbf{k}} + e_{23}^\gamma[\hat{\mathbf{K}}] \sin \phi_{\mathbf{k}} \right) \\ &\quad + \frac{\theta_{\mathbf{k}}^2}{4} \left( e_{11}^\gamma[\hat{\mathbf{K}}] \cos^2 \phi_{\mathbf{k}} + e_{12}^\gamma[\hat{\mathbf{K}}] \sin 2\phi_{\mathbf{k}} + e_{22}^\gamma[\hat{\mathbf{K}}] \sin^2 \phi_{\mathbf{k}} - 2e_{33}^\gamma[\hat{\mathbf{K}}] \right). \end{aligned} \quad (\text{B.4})$$

Consequently, one has

$$\begin{aligned} F_\gamma^2(\hat{\mathbf{K}}, \hat{\mathbf{k}}) &= (e_{33}^\gamma[\hat{\mathbf{K}}])^2 + 2\theta_{\mathbf{k}} e_{33}^\gamma[\hat{\mathbf{K}}] \left( e_{13}^\gamma[\hat{\mathbf{K}}] \cos \phi_{\mathbf{k}} + e_{23}^\gamma[\hat{\mathbf{K}}] \sin \phi_{\mathbf{k}} \right) + \theta_{\mathbf{k}}^2 \left[ \left( e_{13}^\gamma[\hat{\mathbf{K}}] \cos \phi_{\mathbf{k}} + e_{23}^\gamma[\hat{\mathbf{K}}] \sin \phi_{\mathbf{k}} \right)^2 \right. \\ &\quad \left. + 2e_{33}^\gamma[\hat{\mathbf{K}}] \left( e_{11}^\gamma[\hat{\mathbf{K}}] \frac{\cos^2 \phi_{\mathbf{k}}}{4} + e_{12}^\gamma[\hat{\mathbf{K}}] \frac{\sin 2\phi_{\mathbf{k}}}{4} + e_{22}^\gamma[\hat{\mathbf{K}}] \frac{\sin^2 \phi_{\mathbf{k}}}{4} - \frac{e_{33}^\gamma[\hat{\mathbf{K}}]}{2} \right) \right]. \end{aligned} \quad (\text{B.5})$$

Hence the detector pattern function for given wave vectors  $\mathbf{k}$  and  $\mathbf{K}$ , up to  $\mathcal{O}(\theta_{\mathbf{k}}^2)$ , is determined by Eq. (B.5). According to definition of the polarization tensors  $e_{ij}^\gamma[\hat{\mathbf{K}}]$  given by Eqs. (2.5, 2.6) one has

$$\begin{cases} e_{13}^+ = -\sin \Theta_K \cos \Theta_K \cos \Phi_K \\ e_{13}^\times = \sin \Theta_K \sin \Phi_K \end{cases}, \quad \begin{cases} e_{23}^+ = -\sin \Theta_K \cos \Theta_K \sin \Phi_K \\ e_{23}^\times = -\sin \Theta_K \cos \Phi_K \end{cases}, \quad \begin{cases} e_{33}^+ = \sin^2 \Theta_K \\ e_{33}^\times = 0. \end{cases} \quad (\text{B.6})$$

Integration over the azimuthal angle  $\Phi_K$  yields

$$\int_0^{2\pi} d\Phi_K e_{13}^\gamma[\hat{\mathbf{K}}] e_{33}^\gamma[\hat{\mathbf{K}}] = 0 = \int_0^{2\pi} d\Phi_K e_{23}^\gamma[\hat{\mathbf{K}}] e_{33}^\gamma[\hat{\mathbf{K}}]. \quad (\text{B.7})$$

Thus, the contribution of the second term in Eq. (B.5) vanishes. On the other hand, the last term is proportional to  $\theta_{\mathbf{k}}^2 \sim \mathcal{O}(10^{-16})$  and can be ignored safely. Consequently, one has

$$\begin{aligned} \int_0^{2\pi} d\Phi_K \int_0^\pi d\Theta_K \sin \Theta_K F_\gamma^2(\hat{\mathbf{K}}, \hat{\mathbf{k}}) &\rightarrow \int_0^{2\pi} d\Phi_K \int_0^\pi d\Theta_K \sin \Theta_K F_+^2(\hat{\mathbf{K}}, \hat{\mathbf{k}}) \\ &= \int_0^{2\pi} d\Phi_K \int_0^\pi d\Theta_K \sin \Theta_K^5. \end{aligned} \quad (\text{B.8})$$

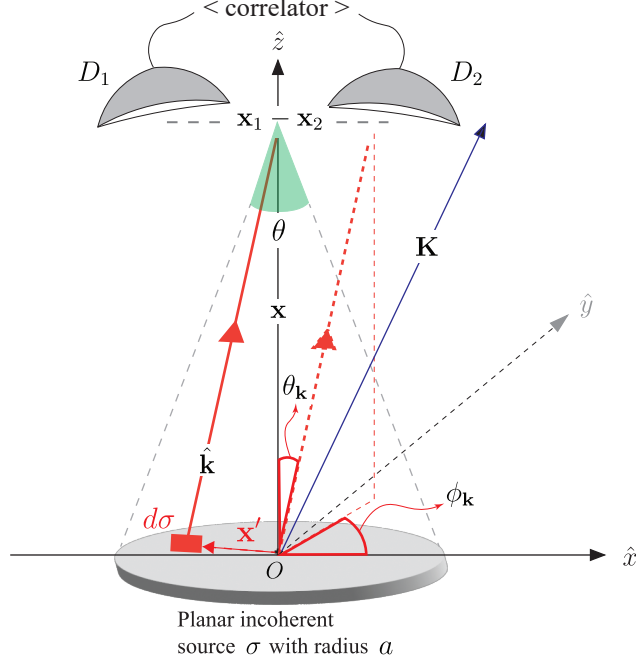


**Figure 8.** Representation of the van Citter-Zernike theorem; an infinitesimal surface element  $d\sigma$  on the planar source, located at  $\mathbf{x}'$  from the origin  $O$ , sends EM radiation with a wave vector  $\hat{\mathbf{k}} = k(\sin \theta_{\mathbf{k}}/2 \cos \phi_{\mathbf{k}}, \sin \theta_{\mathbf{k}}/2 \sin \phi_{\mathbf{k}}, \cos \theta_{\mathbf{k}})$  to the Earth. Here,  $\theta_{\mathbf{k}}$  and  $\phi_{\mathbf{k}}$  show spatial angles of the EM wave vector.

and integration over  $d^3\mathbf{K}$  is simplified as follows

$$\sum_{\gamma} \int_{\mathbf{K} \in \mathbb{R}^3} d^3\mathbf{K} \kappa_{\gamma}^2(\mathbf{K}, \mathbf{k}) = \frac{1}{(2\pi)^2} \left( \frac{\hbar\omega_{\mathbf{k}}}{E_{\text{Pl}}} \right)^2 \int_0^{2\pi} d\Phi_K \int_0^{\pi} d\Theta_K \sin^5 \Theta_K \int_{K_E}^{K_1} \frac{dK}{K}. \quad (\text{B.9})$$

## B.2 $Kd_{12} \ll 1$ approximation

Other expressions of interest are quantities containing the phase difference factor  $\mathbf{K} \cdot (\mathbf{x}_2 - \mathbf{x}_1)$ . With the help of panel(c) of figure 2, one may write

$$\begin{aligned} \hat{\mathbf{K}} \cdot \hat{\mathbf{x}}_1 &= \cos(\Theta_K + \alpha/2) = \cos \Theta_K \cos \alpha/2 - \sin \Theta_K \sin \alpha/2 \simeq \cos \Theta_K - \frac{\alpha}{2} \sin \Theta_K, \\ \hat{\mathbf{K}} \cdot \hat{\mathbf{x}}_2 &= \cos(\Theta_K - \alpha/2) = \cos \Theta_K \cos \alpha/2 + \sin \Theta_K \sin \alpha/2 \simeq \cos \Theta_K + \frac{\alpha}{2} \sin \Theta_K, \end{aligned} \quad (\text{B.10})$$

where  $\alpha \equiv d_{12}/x \ll 1$  is, by definition, the angular diameter subtended by  $d_{12}$  when viewed from the source  $\sigma$ . Moreover, one has

$$\mathbf{K} \cdot (\mathbf{x}_2 - \mathbf{x}_1) \simeq |\mathbf{K}| |\mathbf{x}_2 - \mathbf{x}_1| (\hat{\mathbf{K}} \cdot \hat{\mathbf{i}}) = K d_{12} \sin \Theta_K. \quad (\text{B.11})$$

For low-frequency part of PGWs spectrum which possess the highest graviton content and has the major incoherence effect, one may safely assume  $Kd_{12} \ll 1$ . Thus, we may use the

following approximations

$$\begin{aligned}\sin[\mathbf{K} \cdot (\mathbf{x}_2 - \mathbf{x}_1)] &\simeq \mathbf{K} \cdot (\mathbf{x}_2 - \mathbf{x}_1) = Kd_{12} \sin \Theta_K, \\ \cos[\mathbf{K} \cdot (\mathbf{x}_2 - \mathbf{x}_1)] &\simeq 1 - \frac{(\mathbf{K} \cdot (\mathbf{x}_2 - \mathbf{x}_1))^2}{2} = 1 - \frac{(Kd_{12} \sin \Theta_K)^2}{2}.\end{aligned}\quad (\text{B.12})$$

### B.3 Expression of the time of flight $t$ versus redshift $z$

Typical quasars detected by VLBI means are located at cosmological distances. Hence, it seems necessary to express physical quantities in terms of the redshift of the source,  $z$ , rather than the time of flight  $t$ . These objects are located at redshift range  $0.46 \leq z \leq 2.73$ , so during their journey to the Earth, they have been affected not only by PGWs background, but also by the expansion of the Universe. One may incorporate the Universe expansion by expressing time, distance and frequency in terms of redshift. In particular, one may replace the redshifted EM frequency according to  $\omega_k \rightarrow \omega_k/(1+z)$ . The light detected today was emitted at some earlier time, say  $t_z$ . The time of flight  $t(z)$ , i.e., the time interval between emission at time  $t_{\text{em}}$ , corresponding to the redshift  $z$ , and detection at the present time  $t_{z_H}$ , is determined by [111],

$$t(z) = t_{z_H} - t_{\text{em}} = \int_{z_H}^z \frac{dz'}{(1+z')H(z')}, \quad (\text{B.13})$$

where  $H(z')$  is the Hubble parameter at redshift  $z$  and  $z_H = 0$  is the redshift at present time. We proceed by assuming a flat Universe comprising only cold dark matter and a cosmological constant, so that  $\Omega_\Lambda + \Omega_m = 1$ . The Hubble parameter versus redshift is thus determined by

$$H(z) = H_0 \sqrt{(1 - \Omega_m) + \Omega_m(1+z)^3}. \quad (\text{B.14})$$

By plugging Eq. (B.14) into Eq. (B.13) and setting  $z_H = 0$ , the time of flight  $t(z)$  turns out

$$t(z) = H_0^{-1} \int_0^z \frac{dz'}{\sqrt{(1 - \Omega_m)(1+z')^2 + \Omega_m(1+z')^5}}, \quad (\text{B.15})$$

## C Mutual intensity of a planar source in the presence of PGWs

If one denotes by  $dI(\mathbf{x}_P, t)$  the intensity element at point  $\mathbf{x}_P$  formed by a differential surface element  $d\sigma$  located at  $\mathbf{x}'$  on the source and possessing the wave vector  $\mathbf{k}$ , Eq. (4.4) may be written as

$$\begin{aligned}dI(\mathbf{x}_P, t) &= |\mathcal{E}_{\mathbf{k}}|^2 \left\{ \langle \hat{n}_{\mathbf{k}}(\mathbf{x}_1, t) \rangle + \langle \hat{n}_{\mathbf{k}}(\mathbf{x}_2, t) \rangle + 2\Re[\langle \hat{a}_{\mathbf{k}}^\dagger(\mathbf{x}_1, t) \hat{a}_{\mathbf{k}}(\mathbf{x}_2, t) \rangle e^{-i\mathbf{k} \cdot (\mathbf{x}_1 - \mathbf{x}_2)}] \right\} \\ &\equiv dI_{\mathbf{k}}(\mathbf{x}') + dI_{\mathbf{k}}(\mathbf{x}') + 2\Re[g_{\mathbf{k}}^{(1)}(\mathbf{x}_1, t; \mathbf{x}_2, t) dI_{\mathbf{k}}(\mathbf{x}') e^{-i\mathbf{k} \cdot (\mathbf{x}_1 - \mathbf{x}_2)}].\end{aligned}\quad (\text{C.1})$$

According to Eq. (3.15), one can check that  $\langle \hat{n}_{\mathbf{k}}(\mathbf{x}, t) \rangle = \langle \hat{n}_{\mathbf{k}} \rangle$ , hence the mean number of photons is spacetime-independent, and is equal to its initial value at the emission moment. The conservation of photons propagating in GW background is a result of the adiabatic approximation  $\omega_k \ll \Omega_K$  (see [95] for details), which is also consistent with the eikonal approximation (see [134]). Thus, one may formally relate  $\langle \hat{n}_{\mathbf{k}} \rangle$  to the intensity at initial moment, by writing  $dI_{\mathbf{k}}(\mathbf{x}') \equiv |\mathcal{E}_{\mathbf{k}}|^2 \langle \hat{n}_{\mathbf{k}} \rangle$ . Now,  $dI_{\mathbf{k}}$  accounts for the contribution of the

intensity at surface element  $d\sigma$  located at  $\mathbf{x}'$  and transferred by the wave mode  $\mathbf{k}$  to the point  $\mathbf{x}_P$ . One may also define the surface intensity density  $i(\mathbf{x}')$  at the source, according to

$$i(\mathbf{x}') \equiv \frac{dI_{\mathbf{k}}(\mathbf{x}')}{d\sigma}, \quad (\text{C.2})$$

Assuming a constant intensity density over the surface of source,  $i(\mathbf{x}') \equiv cte$ , the whole intensity radiated from the source may be written as  $I \equiv \int dI_{\mathbf{k}} = \int id\sigma$ . The total intensity at point  $\mathbf{x}_P$  can now be found by integrating over all surface elements. This gives rise to

$$I(\mathbf{x}_P, t) = 2I + 2I \left[ \frac{\int_{x' \leq a} d\sigma g_{\mathbf{k}}^{(1)}(\mathbf{x}_1, t; \mathbf{x}_2, t) e^{-i\mathbf{k} \cdot (\mathbf{x}_1 - \mathbf{x}_2)}}{\int_{x' \leq a} d\sigma} \right]. \quad (\text{C.3})$$

In the next step, we use the fact that the effect of PGWs on all modes  $\mathbf{k}$  leaving the source is identical and determined by Eq. (4.22), as in case of the single-mode  $\mathbf{k}$ . Basically, according to Sec. 4.2, one may check that the wave vector  $\hat{\mathbf{k}}$  appears only in the detector pattern function through  $F_{\gamma}^2(\hat{\mathbf{k}}, \hat{\mathbf{K}})$ , which is shown to be equivalent for all wave vectors  $\mathbf{k}$  (see App. B.1). As a result, the degree of coherence  $g_{\mathbf{k}}^{(1)}(\mathbf{x}_1, t; \mathbf{x}_2, t)$  is the same for all  $\mathbf{k}$  (remind that we take the same frequency  $\omega_k = c|\mathbf{k}|$  for all EM modes). The remaining factor in Eq. (C.3) which contains the contribution of phase factors from different surface elements of the source, can be written in the following compact form

$$j(\mathbf{x}_1, \mathbf{x}_2) \equiv \frac{\int_{x' \leq a} d\sigma e^{-i\mathbf{k} \cdot (\mathbf{x}_1 - \mathbf{x}_2)}}{\int_{x' \leq a} d\sigma} \quad (\text{C.4})$$

which is nothing but the far-zone form of the van Citter-Zernike theorem, and is called the mutual intensity (see Sec. 4.4.4 of [18] for comparison). Here,  $\mathbf{x}_1$  and  $\mathbf{x}_2$  represent the relative distance between the surface element  $d\sigma$  and detector points  $P_1$  and  $P_2$ , respectively. Integration over the surface yields (see [18])

$$j(\mathbf{x}_1, \mathbf{x}_2) = \frac{2J_1(\nu)}{\nu}, \quad (\text{C.5})$$

where  $\nu = k(a/x)d_{12}$ . Consequently, the total intensity at point  $\mathbf{x}_P$  turns out as follows

$$I(\mathbf{x}_P, t) = 2I \left( 1 + \Re \left[ g^{(1)}(\mathbf{x}_1, t; \mathbf{x}_2, t) j(\mathbf{x}_1, \mathbf{x}_2) \right] \right). \quad (\text{C.6})$$

## D Loss of spatial correlations induced by GWs in vacuum, thermal and squeezed state

### D.1 Loss of spatial correlations induced by quantum fluctuations of GWs

In this section, we investigate the effect of quantum fluctuations of GWs on spatial correlations of the EM field. We may denote by  $\hat{\rho}_{\text{vac}} \equiv \prod_{\gamma, \mathbf{K} \in \mathbb{R}^{3+}} |0_{\mathbf{K}}, 0_{-\mathbf{K}}\rangle \langle 0_{\mathbf{K}}, 0_{-\mathbf{K}}|$ . As before, the expression of the intensity is determined by Eq. (4.6), while the equal-time first-order degree

of coherence is now determined by

$$\begin{aligned}
g_{\text{vac}}^{(1)}(\mathbf{x}_1, t; \mathbf{x}_2, t) &= \prod_{\gamma, \mathbf{K} \in \mathbb{R}^{3+}} \langle 0_{\mathbf{K}}, 0_{-\mathbf{K}} | \hat{D}_{\mathbf{K}}^\dagger(-\kappa\eta_{\mathbf{K}}(\mathbf{x}_1, t)) \hat{D}_{\mathbf{K}}(-\kappa\eta_{\mathbf{K}}(\mathbf{x}_2, t)) \\
&\quad \times \hat{D}_{-\mathbf{K}}^\dagger(-\kappa\eta_{-\mathbf{K}}(\mathbf{x}_1, t)) \hat{D}_{-\mathbf{K}}(-\kappa\eta_{-\mathbf{K}}(\mathbf{x}_2, t)) | 0_{\mathbf{K}}, 0_{-\mathbf{K}} \rangle \quad (\text{D.1}) \\
&= \prod_{\gamma, \mathbf{K} \in \mathbb{R}^{3+}} \langle 0_{\mathbf{K}} | \hat{D}_{\mathbf{K}}^\dagger(-\kappa\eta_{\mathbf{K}}(\mathbf{x}_1, t)) \hat{D}_{\mathbf{K}}(-\kappa\eta_{\mathbf{K}}(\mathbf{x}_2, t)) | 0_{\mathbf{K}} \rangle \\
&\quad \times \langle 0_{-\mathbf{K}} | \hat{D}_{-\mathbf{K}}^\dagger(-\kappa\eta_{-\mathbf{K}}(\mathbf{x}_1, t)) \hat{D}_{-\mathbf{K}}(-\kappa\eta_{-\mathbf{K}}(\mathbf{x}_2, t)) | 0_{-\mathbf{K}} \rangle.
\end{aligned}$$

With the help of the property  $\hat{D}^\dagger(\alpha)\hat{D}(\beta) = e^{-i\Im\alpha\beta^*}\hat{D}(\beta - \alpha)$  for displacement operator, Eq. (D.1) is rewritten as

$$\begin{aligned}
g_{\text{vac}}^{(1)}(\mathbf{x}_1, t; \mathbf{x}_2, t) &= \prod_{\gamma, \mathbf{K} \in \mathbb{R}^{3+}} \langle 0_{\mathbf{K}} | e^{-i\kappa^2\Im(\eta_{\mathbf{K}}(\mathbf{x}_1, t)\eta_{\mathbf{K}}^*(\mathbf{x}_2, t))} \hat{D}_{\mathbf{K}}(\kappa[\eta_{\mathbf{K}}(\mathbf{x}_1, t) - \eta_{\mathbf{K}}(\mathbf{x}_2, t)]) | 0_{\mathbf{K}} \rangle \quad (\text{D.2}) \\
&\quad \times \langle 0_{-\mathbf{K}} | e^{-i\kappa^2\Im(\eta_{-\mathbf{K}}(\mathbf{x}_1, t)\eta_{-\mathbf{K}}^*(\mathbf{x}_2, t))} \hat{D}_{-\mathbf{K}}(\kappa[\eta_{-\mathbf{K}}(\mathbf{x}_1, t) - \eta_{-\mathbf{K}}(\mathbf{x}_2, t)]) | 0_{-\mathbf{K}} \rangle \\
&= \prod_{\gamma, \mathbf{K} \in \mathbb{R}^{3+}} e^{-i\kappa^2\Im(\eta_{\mathbf{K}}(\mathbf{x}_1, t)\eta_{\mathbf{K}}^*(\mathbf{x}_2, t) + \eta_{-\mathbf{K}}(\mathbf{x}_1, t)\eta_{-\mathbf{K}}^*(\mathbf{x}_2, t))} \\
&\quad \times \exp\left[-\frac{1}{2}\kappa^2|\eta_{\mathbf{K}}(\mathbf{x}_1, t) - \eta_{\mathbf{K}}(\mathbf{x}_2, t)|^2\right] \exp\left[-\frac{1}{2}\kappa^2|\eta_{-\mathbf{K}}(\mathbf{x}_1, t) - \eta_{-\mathbf{K}}(\mathbf{x}_2, t)|^2\right].
\end{aligned}$$

Note that, in the above equations, we have used  $\kappa$  in place of  $\kappa_\gamma(\mathbf{K}, \mathbf{k})$  for simplicity. Moreover, from definition Eq. (3.9), one has  $\kappa_\gamma(\mathbf{K}, \mathbf{k}) = \kappa_\gamma(-\mathbf{K}, \mathbf{k})$ . Using the continuous notation, Eq. (D.2) becomes

$$\begin{aligned}
g_{\text{vac}}^{(1)}(\mathbf{x}_1, t; \mathbf{x}_2, t) &= e^{-i\sum_\gamma \int_{\mathbf{K} \in \mathbb{R}^3} d^3\mathbf{K} \kappa_\gamma^2(\mathbf{K}, \mathbf{k}) \Im(\eta_{\mathbf{K}}(\mathbf{x}_1, t)\eta_{\mathbf{K}}^*(\mathbf{x}_2, t))} \quad (\text{D.3}) \\
&\quad \times \exp\left[-\frac{1}{2}\sum_\gamma \int_{\mathbf{K} \in \mathbb{R}^3} d^3\mathbf{K} \kappa_\gamma^2(\mathbf{K}, \mathbf{k}) |\eta_{\mathbf{K}}(\mathbf{x}_1, t) - \eta_{\mathbf{K}}(\mathbf{x}_2, t)|^2\right].
\end{aligned}$$

With the help of definitions for  $\mathcal{C}_{\mathbf{K}}(\mathbf{x}_1, t; \mathbf{x}_2, t)$  and  $\mathcal{D}_{\mathbf{K}}(\mathbf{x}_1, t; \mathbf{x}_2, t)$  given by Eq. (4.16) of the text, it turns out that Eq. (D.3) is nothing but

$$g_{\text{vac}}^{(1)}(\mathbf{x}_1, t; \mathbf{x}_2, t) = e^{-i\mathcal{C}(\mathbf{x}_1, t; \mathbf{x}_2, t)} e^{-\mathcal{D}(\mathbf{x}_1, t; \mathbf{x}_2, t)}. \quad (\text{D.4})$$

already defined by Eq. (4.14).

## D.2 Loss of spatial correlations induced by thermal gravitons

Here, we consider a continuum of GWs modes, each of which possessing mean number of gravitons  $\bar{n}_{\text{th}}(K) = [\exp(\frac{\hbar\Omega_K}{k_B T}) - 1]^{-1}$ , with a hypothetical equilibrium temperature  $T$ . Finally, to evaluate the effect of thermal gravitons on spatial coherence of EM field, we assume the mean number of gravitons in thermal state be the same as in highly-squeezed PGWs, namely  $\bar{n}_{\text{th}}(K) = e^{2r_K(\eta_H)}/4$ . This way, we can compare and differentiate between the thermal and the two-mode squeezed background of PGWs. It turns out that, as long as spatial correlations of high-redshift objects matter, one may not discriminate between the highly-populated two-mode squeezed PGWs and the corresponding thermal background (possessing



the same graviton content). The continuum of thermal GWs may be described by following density matrix

$$\hat{\rho}_{\text{th}} \equiv \prod_{\gamma, \mathbf{K} \in \mathbb{R}^3} \hat{\rho}_{\text{th}, \gamma, \mathbf{K}} = \prod_{\gamma, \mathbf{K} \in \mathbb{R}^{3+}} \hat{\rho}_{\text{th}, \gamma, \mathbf{K}} \otimes \hat{\rho}_{\text{th}, \gamma, -\mathbf{K}}, \quad (\text{D.5})$$

where  $\hat{\rho}_{\text{th}, \gamma, \mathbf{K}} = \sum_{n=0}^{\infty} \frac{\bar{n}_{\text{th}}^n(K)}{1 + \bar{n}_{\text{th}}(K)^{n+1}} |n\rangle \langle n|$  denotes the density matrix of thermal state in Fock state representation [125]. In this case, the equal-time first-order degree of coherence Eq. (4.5) is given by

$$\begin{aligned} g_{\text{th}}^{(1)}(\mathbf{x}_1, t; \mathbf{x}_2, t) &= \prod_{\gamma, \mathbf{K} \in \mathbb{R}^{3+}} \langle \hat{D}_{\mathbf{K}}^\dagger(-\kappa\eta_{\mathbf{K}}(\mathbf{x}_1, t)) \hat{D}_{\mathbf{K}}(-\kappa\eta_{\mathbf{K}}(\mathbf{x}_2, t)) \rangle_{\hat{\rho}_{\text{th}, \gamma, \mathbf{K}}} \\ &\times \langle \hat{D}_{-\mathbf{K}}^\dagger(-\kappa\eta_{-\mathbf{K}}(\mathbf{x}_1, t)) \hat{D}_{-\mathbf{K}}(-\kappa\eta_{-\mathbf{K}}(\mathbf{x}_2, t)) \rangle_{\hat{\rho}_{\text{th}, \gamma, -\mathbf{K}}} \\ &= \prod_{\gamma, \mathbf{K} \in \mathbb{R}^{3+}} e^{-i\kappa^2 \Im(\eta_{\mathbf{K}}(\mathbf{x}_1, t)\eta_{\mathbf{K}}^*(\mathbf{x}_2, t))} \langle \hat{D}_{\mathbf{K}}(\kappa[\eta_{\mathbf{K}}(\mathbf{x}_1, t) - \eta_{\mathbf{K}}(\mathbf{x}_2, t)]) \rangle_{\hat{\rho}_{\text{th}, \gamma, \mathbf{K}}} \\ &\times e^{-i\kappa^2 \Im(\eta_{-\mathbf{K}}(\mathbf{x}_1, t)\eta_{-\mathbf{K}}^*(\mathbf{x}_2, t))} \langle \hat{D}_{-\mathbf{K}}(\kappa[\eta_{-\mathbf{K}}(\mathbf{x}_1, t) - \eta_{-\mathbf{K}}(\mathbf{x}_2, t)]) \rangle_{\hat{\rho}_{\text{th}, \gamma, -\mathbf{K}}} \\ &= e^{-i\sum_{\gamma} \int_{\mathbf{K} \in \mathbb{R}^3} d^3\mathbf{K} \kappa_{\gamma}^2(\mathbf{K}, \mathbf{k}) \Im(\eta_{\mathbf{K}}(\mathbf{x}_1, t)\eta_{\mathbf{K}}^*(\mathbf{x}_2, t))} \\ &\times \prod_{\gamma, \mathbf{K} \in \mathbb{R}^3} \langle \hat{D}_{\mathbf{K}}(\kappa[\eta_{\mathbf{K}}(\mathbf{x}_1, t) - \eta_{\mathbf{K}}(\mathbf{x}_2, t)]) \rangle_{\hat{\rho}_{\text{th}, \gamma, \mathbf{K}}} \langle \hat{D}_{-\mathbf{K}}(\kappa[\eta_{-\mathbf{K}}(\mathbf{x}_1, t) - \eta_{-\mathbf{K}}(\mathbf{x}_2, t)]) \rangle_{\hat{\rho}_{\text{th}, \gamma, -\mathbf{K}}}. \end{aligned} \quad (\text{D.6})$$

With the help of  $\langle \hat{D} \rangle_{\hat{\rho}_{\text{th}}} = \exp[-|\alpha|^2(\bar{n}_{\text{th}} + \frac{1}{2})]$  [125], Eq. (D.6) becomes

$$\begin{aligned} g_{\text{th}}^{(1)}(\mathbf{x}_1, t; \mathbf{x}_2, t) &= e^{-i\sum_{\gamma} \int_{\mathbf{K} \in \mathbb{R}^3} d^3\mathbf{K} \kappa_{\gamma}^2(\mathbf{K}, \mathbf{k}) \Im(\eta_{\mathbf{K}}(\mathbf{x}_1, t)\eta_{\mathbf{K}}^*(\mathbf{x}_2, t))} \\ &\times \prod_{\gamma, \mathbf{K} \in \mathbb{R}^3} \exp\left[-\kappa^2 |\eta_{\mathbf{K}}(\mathbf{x}_1, t) - \eta_{\mathbf{K}}(\mathbf{x}_2, t)|^2 (\bar{n}_{\text{th}}(K) + \frac{1}{2})\right] \\ &\times \exp\left[-\kappa^2 |\eta_{-\mathbf{K}}(\mathbf{x}_1, t) - \eta_{-\mathbf{K}}(\mathbf{x}_2, t)|^2 (\bar{n}_{\text{th}}(K) + \frac{1}{2})\right]. \end{aligned} \quad (\text{D.7})$$

In the continuous representation, Eq. (D.7) becomes

$$\begin{aligned} g_{\text{th}}^{(1)}(\mathbf{x}_1, t; \mathbf{x}_2, t) &= e^{-i\sum_{\gamma} \int_{\mathbf{K} \in \mathbb{R}^3} d^3\mathbf{K} \kappa_{\gamma}^2(\mathbf{K}, \mathbf{k}) \Im(\eta_{\mathbf{K}}(\mathbf{x}_1, t)\eta_{\mathbf{K}}^*(\mathbf{x}_2, t))} \\ &\times \exp\left[-\sum_{\gamma} \int_{\mathbf{K} \in \mathbb{R}^3} d^3\mathbf{K} \kappa_{\gamma}^2(\mathbf{K}, \mathbf{k}) |\eta_{\mathbf{K}}(\mathbf{x}_1, t) - \eta_{\mathbf{K}}(\mathbf{x}_2, t)|^2 (\bar{n}_{\text{th}}(K) + \frac{1}{2})\right] \\ &= g_{\text{vac}}^{(1)}(\mathbf{x}_1, t; \mathbf{x}_2, t) \exp\left[-\sum_{\gamma} \int_{\mathbf{K} \in \mathbb{R}^3} d^3\mathbf{K} \kappa_{\gamma}^2(\mathbf{K}, \mathbf{k}) \bar{n}_{\text{th}}(K) \mathcal{D}_{\mathbf{K}}^{\text{vac}}(\mathbf{x}, t; \mathbf{x}_2, t)\right]. \end{aligned} \quad (\text{D.8})$$

In the last equality, we have used definitions of  $\mathcal{C}_{\mathbf{K}}(\mathbf{x}_1, t; \mathbf{x}_2, t)$  and  $\mathcal{D}_{\mathbf{K}}(\mathbf{x}_1, t; \mathbf{x}_2, t)$  given by Eq. (4.16). Thus, Eq. (D.8) implies that thermal gravitons add an extra decaying behaviour to that of vacuum fluctuations. To evaluate the effect, we proceed the same procedure as Sec. 4.2.1; using Eqs. (4.16, 4.19) and with the help of  $Kd_{12} \ll 1$  approximation (see App.B.2), one may write Eq. (D.8) as follows

$$g_{\text{th}}^{(1)}(\mathbf{x}_1, t; \mathbf{x}_2, t) = g_{\text{vac}}^{(1)}(\mathbf{x}_1, t; \mathbf{x}_2, t) e^{-\left(\frac{d_{12}}{\xi^{\text{th}}(t)}\right)^2}. \quad (\text{D.9})$$

where the thermal-induced characteristic coherence length  $\xi^{\text{th}}(t)$  is defined by

$$\xi^{\text{th}}(t) = \left[ \frac{1}{(2\pi)^2} \left( \frac{\hbar\omega_k}{E_{\text{Pl}}} \right)^2 \int_0^{2\pi} d\Phi_K \int_0^\pi d\Theta_K \sin^7 \Theta_K \int_{K_E}^{K_1} dK \left( 4K \bar{n}_{\text{th}}(K) \sin^2 \left( \frac{\Omega_K t}{2} \right) \right) \right]^{-1/2} \quad (\text{D.10})$$

Thus, along with the same lines as Sec. 5.2, the incoherence parameter  $\alpha^{\text{th}}(z)$  may be defined as

$$\begin{aligned} \alpha^{\text{th}}(z) &\equiv \log_{10} (k\xi^{\text{th}}(z)) \quad (\text{D.11}) \\ &= \log_{10} \left( \left[ \frac{1}{(2\pi)^2} \left( \frac{\hbar c}{E_{\text{Pl}}(1+z)} \right)^2 \int_0^{2\pi} d\Phi_K \int_0^\pi d\Theta_K \sin^7 \Theta_K \right. \right. \\ &\quad \left. \left. \times \int_{K_E}^{K_1} dK \left( 4K \bar{n}_{\text{th}}(K) \sin^2 \left( \frac{\Omega_K t(z)}{2} \right) \right) \right]^{-1/2} \right). \end{aligned}$$

where  $t = t(z)$  is implicitly assumed (see Eq. (B.15)). To evaluate the effect of thermal gravitons, we consider the graviton content to be the same as that of TS PGWs, i.e.,  $\bar{n}_{\text{th}}(K) \sim e^{2r_K(\eta_H)}/4$ . The plot of  $\alpha^{\text{th}}(z)$  is sketched in figure 8 in red color, where the solid and dashed lines correspond to  $r_{k_0} = 10^{-2}$  and  $r_{k_0} = 10^{-7}$ , respectively. It is seen that, TS PGWs leaves a slightly sever effect on EM spatial correlations than the corresponding thermal gravitons with the same graviton content, stemming from quantum correlations between gravitons in two-mode squeezed state which are absent in thermal state. Numerical calculations implies the upper bound  $r_{k_0} \lesssim 10^{-6.8}$  corresponding to thermal state of gravitons.

### D.3 Loss of spatial correlations induced by squeezed state

In this section, we calculate incoherence induced by gravitons in squeezed state. We assume that each mode  $K$  of GWs is in its own squeezed state and that, there is no correlation between different modes. The density matrix of a continuum of GWs in squeezed state is determined by

$$\hat{\rho}_{\text{sq}} \equiv \prod_{\gamma, \mathbf{K} \in \mathbb{R}^3} \hat{\rho}_{\text{sq}, \gamma, \mathbf{K}} = \prod_{\gamma, \mathbf{K} \in \mathbb{R}^3} |\zeta_{\gamma, \mathbf{K}}\rangle \langle \zeta_{\gamma, \mathbf{K}}| = \prod_{\gamma, \mathbf{K} \in \mathbb{R}^{3+}} |\zeta_{\gamma, \mathbf{K}}, \zeta_{\gamma, -\mathbf{K}}\rangle \langle \zeta_{\gamma, \mathbf{K}}, \zeta_{\gamma, -\mathbf{K}}| \quad (\text{D.12})$$

where  $\zeta_K \equiv r_K e^{2i\phi_K}$  represents the squeezing parameter with  $(r_k, 2\phi_K)$  being the squeezing amplitude and angle, respectively. The expression of the equal-time first-order degree of coherence Eq. (4.5) is now given by

$$\begin{aligned} g_{\text{sq}}^{(1)}(\mathbf{x}_1, t; \mathbf{x}_2, t) &= \prod_{\gamma, \mathbf{K} \in \mathbb{R}^{3+}} \langle \zeta_{\gamma, \mathbf{K}} | \hat{D}_{\mathbf{K}}^\dagger(-\kappa\eta_{\mathbf{K}}(\mathbf{x}_1, t)) \hat{D}_{\mathbf{K}}(-\kappa\eta_{\mathbf{K}}(\mathbf{x}_2, t)) | \zeta_{\gamma, \mathbf{K}} \rangle \quad (\text{D.13}) \\ &\times \langle \zeta_{\gamma, -\mathbf{K}} | \hat{D}_{-\mathbf{K}}^\dagger(-\kappa\eta_{-\mathbf{K}}(\mathbf{x}_1, t)) \hat{D}_{-\mathbf{K}}(-\kappa\eta_{-\mathbf{K}}(\mathbf{x}_2, t)) | \zeta_{\gamma, -\mathbf{K}} \rangle \\ &= \prod_{\gamma, \mathbf{K} \in \mathbb{R}^{3+}} e^{-i\kappa^2 \Im(\eta_{\mathbf{K}}(\mathbf{x}_1, t) \eta_{\mathbf{K}}^*(\mathbf{x}_2, t))} \langle \zeta_{\gamma, \mathbf{K}} | \hat{D}_{\mathbf{K}}(\kappa[\eta_{\mathbf{K}}(\mathbf{x}_1, t) - \eta_{\mathbf{K}}(\mathbf{x}_2, t)]) | \zeta_{\gamma, \mathbf{K}} \rangle \\ &\times e^{-i\kappa^2 \Im(\eta_{-\mathbf{K}}(\mathbf{x}_1, t) \eta_{-\mathbf{K}}^*(\mathbf{x}_2, t))} \langle \zeta_{\gamma, -\mathbf{K}} | \hat{D}_{-\mathbf{K}}(\kappa[\eta_{-\mathbf{K}}(\mathbf{x}_1, t) - \eta_{-\mathbf{K}}(\mathbf{x}_2, t)]) | \zeta_{\gamma, -\mathbf{K}} \rangle \\ &= e^{-i\sum_\gamma \int_{\mathbf{K} \in \mathbb{R}^3} d^3\mathbf{K} \kappa_\gamma^2(\mathbf{K}, \mathbf{k}) \Im(\eta_{\mathbf{K}}(\mathbf{x}_1, t) \eta_{\mathbf{K}}^*(\mathbf{x}_2, t))} \\ &\times \prod_{\gamma, \mathbf{K} \in \mathbb{R}^3} \langle \zeta_{\gamma, \mathbf{K}} | \hat{D}_{\mathbf{K}}(\kappa[\eta_{\mathbf{K}}(\mathbf{x}_1, t) - \eta_{\mathbf{K}}(\mathbf{x}_2, t)]) | \zeta_{\gamma, \mathbf{K}} \rangle \\ &\times \langle \zeta_{\gamma, -\mathbf{K}} | \hat{D}_{-\mathbf{K}}(\kappa[\eta_{-\mathbf{K}}(\mathbf{x}_1, t) - \eta_{-\mathbf{K}}(\mathbf{x}_2, t)]) | \zeta_{\gamma, -\mathbf{K}} \rangle. \end{aligned}$$

For a given squeezed state  $|\zeta\rangle$ , it is straightforward to show that

$$\langle\zeta|\hat{D}(\alpha)|\zeta\rangle = \langle 0|\hat{S}^\dagger(\zeta)\hat{D}(\alpha)\hat{S}(\zeta)|0\rangle = \langle 0|\hat{D}(\alpha')|0\rangle = \exp\left(-\frac{1}{2}|\alpha'|^2\right), \quad (\text{D.14})$$

where  $\hat{D}(\alpha)$  and  $\hat{S}(\zeta)$  show the displacement and squeezing operators, respectively, and

$$\alpha' = \alpha \cosh r + \alpha^* e^{2i\phi} \sinh r. \quad (\text{D.15})$$

With the help of Eqs. (D.14 , D.15), Eq. (D.13) is written as the following form

$$\begin{aligned} g_{\text{sq}}^{(1)}(\mathbf{x}_1, t; \mathbf{x}_2, t) &= e^{-i\sum_\gamma \int_{\mathbf{K}\in\mathbb{R}^3} d^3\mathbf{K} \kappa_\gamma^2(\mathbf{K}, \mathbf{k}) \Im(\eta_{\mathbf{K}}(\mathbf{x}_1, t) \eta_{\mathbf{K}}^*(\mathbf{x}_2, t))} \\ &\times \prod_{\gamma, \mathbf{K}\in\mathbb{R}^3} \exp\left[-\frac{\kappa_\gamma^2}{2} |(\eta_{\mathbf{K}}(\mathbf{x}_1, t) - \eta_{\mathbf{K}}(\mathbf{x}_2, t)) \cosh r_K + (\eta_{\mathbf{K}}^*(\mathbf{x}_1, t) - \eta_{\mathbf{K}}^*(\mathbf{x}_2, t)) e^{2i\phi_K} \sinh r_K|^2\right] \\ &= e^{-i\sum_\gamma \int_{\mathbf{K}\in\mathbb{R}^3} d^3\mathbf{K} \kappa_\gamma^2(\mathbf{K}, \mathbf{k}) \Im(\eta_{\mathbf{K}}(\mathbf{x}_1, t) \eta_{\mathbf{K}}^*(\mathbf{x}_2, t))} \\ &\times \exp\left[-\frac{1}{2} \sum_\gamma \int_{\mathbf{K}\in\mathbb{R}^{3+}} \kappa_\gamma^2(\mathbf{K}, \mathbf{k}) \left\{ (1 + 2\bar{n}_{\text{sq}}(K)) \mathcal{D}_{\mathbf{K}}^{\text{vac}}(\mathbf{x}_1, t; \mathbf{x}_2, t) + \mathcal{D}_{\mathbf{K}}^{\text{sq-corr}}(\mathbf{x}_1, t; \mathbf{x}_2, t) \right\}\right], \end{aligned} \quad (\text{D.16})$$

where  $\mathcal{D}_{\mathbf{K}}^{\text{vac}}$  is defined by Eq. (4.16). Here, we have defined

$$\mathcal{D}_{\mathbf{K}}^{\text{sq-corr}}(\mathbf{x}_1, t; \mathbf{x}_2, t) \equiv \sinh 2r_K \Re\left[e^{-2i\phi_K} (\eta_{\mathbf{K}}(\mathbf{x}_1, t) - \eta_{\mathbf{K}}(\mathbf{x}_2, t))^2\right] \quad (\text{D.17})$$

which is almost similar to  $\mathcal{D}_{\mathbf{K}}^{\text{ts-corr}}(\mathbf{x}_1, t; \mathbf{x}_2, t)$  defined by Eq. (4.18) for TS state, and shows the contribution of correlations between gravitons in the squeezed state, on EM spatial incoherence. By separating the contribution of vacuum fluctuations, Eq. (D.16) recast to

$$g_{\text{sq}}^{(1)}(\mathbf{x}_1, t; \mathbf{x}_2, t) = g_{\text{vac}}^{(1)}(\mathbf{x}_1, t; \mathbf{x}_2, t) e^{-\mathcal{D}^{\text{sq}}(\mathbf{x}_1, t; \mathbf{x}_2, t)}, \quad (\text{D.18})$$

and the effect of squeezed gravitons on the EM spatial coherence is encapsulated in the two-point function

$$\begin{aligned} \mathcal{D}^{\text{sq}}(\mathbf{x}_1, t; \mathbf{x}_2, t) &\equiv \sum_\gamma \int_{\mathbf{K}\in\mathbb{R}^3} \kappa_\gamma^2(\mathbf{K}, \mathbf{k}) \left\{ \bar{n}_{\text{sq}}(K) \mathcal{D}_{\mathbf{K}}^{\text{vac}}(\mathbf{x}_1, t; \mathbf{x}_2, t) \right. \\ &\quad \left. + \frac{1}{2} \mathcal{D}_{\mathbf{K}}^{\text{sq-corr}}(\mathbf{x}_1, t; \mathbf{x}_2, t) \right\}, \end{aligned} \quad (\text{D.19})$$

With the help of definition Eq. (3.16) for  $\eta_{\mathbf{K}}(\mathbf{x}, t)$ , one has

$$\begin{aligned} \mathcal{D}_{\mathbf{K}}^{\text{sq-corr}}(\mathbf{x}_1, t_1; \mathbf{x}_2, t_2) &= \sinh 2r_K \left\{ \cos[2\phi_K + 2\mathbf{K} \cdot \mathbf{x}_1] - 2 \cos[2\phi_K + 2\mathbf{K} \cdot \mathbf{x}_1 - \Omega_K t] + \cos[2\phi_K + 2\mathbf{K} \cdot \mathbf{x}_1 - 2\Omega_K t] \right. \\ &\quad + \cos[2\phi_K + 2\mathbf{K} \cdot \mathbf{x}_2] - 2 \cos[2\phi_K + 2\mathbf{K} \cdot \mathbf{x}_2 - \Omega_K t] + \cos[2\phi_K + 2\mathbf{K} \cdot \mathbf{x}_2 - 2\Omega_K t] \\ &\quad - 2 \cos[2\phi_K + \mathbf{K} \cdot (\mathbf{x}_1 + \mathbf{x}_2)] + 2 \cos[2\phi_K + \mathbf{K} \cdot (\mathbf{x}_1 + \mathbf{x}_2) - \Omega_K t] \\ &\quad \left. + 2 \cos[2\phi_K + \mathbf{K} \cdot (\mathbf{x}_1 + \mathbf{x}_2) - \Omega_K t] - 2 \cos[2\phi_K + \mathbf{K} \cdot (\mathbf{x}_1 + \mathbf{x}_2) - 2\Omega_K t] \right\}. \end{aligned} \quad (\text{D.20})$$

We may proceed by assuming  $|\mathbf{x}_1| \simeq |\mathbf{x}_2| \simeq x$ , where  $x \equiv ct$  denotes the distance of the object to the Earth, as shown in panel (c) of figure 2. With the help of Eq. (B.10), Eq. (D.16)

becomes

$$\begin{aligned}
\mathcal{D}_{\mathbf{K}}^{\text{sq-corr}}(\mathbf{x}_1, t_1; \mathbf{x}_2, t_2) = & \sinh 2r_K \left\{ \cos[2\phi_K + 2\Omega_K t \cos \Theta_K - K d_{12} \sin \Theta_K] \right. \\
& + \cos[2\phi_K + 2\Omega_K t \cos \Theta_K + K d_{12} \sin \Theta_K] \\
& - 2 \cos[2\phi_K + 2\Omega_K t \cos \Theta_K - \Omega_K t - K d_{12} \sin \Theta_K] \\
& - 2 \cos[2\phi_K + 2\Omega_K t \cos \Theta_K - \Omega_K t + K d_{12} \sin \Theta_K] \\
& + \cos[2\phi_K + 2\Omega_K t \cos \Theta_K - 2\Omega_K t - K d_{12} \sin \Theta_K] \\
& + \cos[2\phi_K + 2\Omega_K t \cos \Theta_K - 2\Omega_K t + K d_{12} \sin \Theta_K] \\
& - 2 \cos[2\phi_K + 2\Omega_K t \cos \Theta_K] + 4 \cos[2\phi_K + 2\Omega_K t \cos \Theta_K - \Omega_K t] \\
& \left. - 2 \cos[2\phi_K + 2\Omega_K t \cos \Theta_K - 2\Omega_K t] \right\}, \tag{D.21}
\end{aligned}$$

which can be simplified to

$$\begin{aligned}
\mathcal{D}_{\mathbf{K}}^{\text{sq-corr}}(\mathbf{x}_1, t_1; \mathbf{x}_2, t_2) = & \sinh 2r_K \left( 2 \cos[2\phi_K + 2\Omega_K t \cos \Theta_K] - 4 \cos[2\phi_K + 2\Omega_K t \cos \Theta_K - \Omega_K t] \right. \\
& \left. + 2 \cos[2\phi_K + 2\Omega_K t \cos \Theta_K - 2\Omega_K t] \right) \left( \cos[K d_{12} \sin \Theta_K] - 1 \right) \\
= & - \sinh 2r_K \left( \cos[2\phi_K + 2\Omega_K t \cos \Theta_K] - 2 \cos[2\phi_K + 2\Omega_K t \cos \Theta_K - \Omega_K t] \right. \\
& \left. + \cos[2\phi_K + 2\Omega_K t \cos \Theta_K - 2\Omega_K t] \right) (K d_{12} \sin \Theta_K)^2. \tag{D.22}
\end{aligned}$$

In the last equality, we applied the  $K d_{12} \ll 1$  approximation (see App. B.2). Combining Eqs. (4.16 , D.22 , D.19), one may show that

$$\mathcal{D}_{\mathbf{K}}^{\text{sq}}(\mathbf{x}_1, t_1; \mathbf{x}_2, t_2) = \left( \frac{d_{12}}{\xi^{\text{sq}}(t)} \right)^2, \tag{D.23}$$

where the squeezed-induced incoherence length  $\xi^{\text{sq}}(t)$  is defined by

$$\begin{aligned}
\xi^{\text{sq}}(t) = & \left[ \frac{1}{(2\pi)^2} \left( \frac{\hbar\omega_k}{E_{\text{Pl}}} \right)^2 \int_0^{2\pi} d\Phi_K \int_0^\pi d\Theta_K \sin^7 \Theta_K \int_{K_E}^{K_1} dK K \left\{ \bar{n}_{\text{ts}}(K) \left( 4 \sin^2 \left( \frac{\Omega_K t}{2} \right) \right) \right. \right. \\
& - \frac{1}{2} \sinh 2r_K \left( \cos[2\phi_K + 2\Omega_K t \cos \Theta_K] - 2 \cos[2\phi_K + 2\Omega_K t \cos \Theta_K - \Omega_K t] \right. \\
& \left. \left. + \cos[2\phi_K + 2\Omega_K t \cos \Theta_K - 2\Omega_K t] \right) \right]^{-1/2}. \tag{D.24}
\end{aligned}$$

Again, one may define the incoherence parameter induced by squeezed GWs according to

$$\alpha^{\text{sq}}(z) \equiv \log_{10} (k \xi^{\text{sq}}(z)). \tag{D.25}$$

In case of a (hypothetical) highly-squeezed PGWs with the same graviton content as TS PGWs, one has  $\bar{n}_{\text{sq}}(K) \simeq e^{2r_K(\eta_H)}/4$  and  $\sinh 2r_K \simeq e^{2r_K(\eta_H)}/2$ , thus  $\alpha^{\text{sq}}(z)$  reduces to

$$\begin{aligned}
\alpha^{\text{sq}}(t) = & \log_{10} \left( \left[ \frac{1}{(2\pi)^2} \left( \frac{\hbar c}{E_{\text{Pl}}(1+z)} \right)^2 \int_0^{2\pi} d\Phi_K \int_0^\pi d\Theta_K \sin^7 \Theta_K \right. \right. \\
& \left. \left. \times \int_{K_E}^{K_1} dK \left( \frac{K e^{2r_K(\eta_H)}}{4} \right) 8 \sin^2 \left( \frac{\Omega_K t(z)}{2} \right) \cos^2 \left[ \frac{2\phi_K + 2\Omega_K t(z)(\cos \Theta_K - 1)}{2} \right] \right]^{-1/2} \right). \tag{D.26}
\end{aligned}$$

where  $t(z)$  is given by Eq. (B.15). The plot of  $\alpha^{\text{sq}}(z)$  for  $\phi_K = 0$  is shown in figure 9 with the blue and green points, corresponding to  $r_{k_0} = 0.032 \sim 10^{-1.5}$  and  $r_{k_0} = 10^{-7}$ , respectively. These points almost coincide with the red curves, corresponding to thermal GWs (see App. D.2). Again, one may see that the most sever constraint on the tensor-to-scalar ratio comes from the TS state,  $r_{k_0} \lesssim 10^{-7}$ .

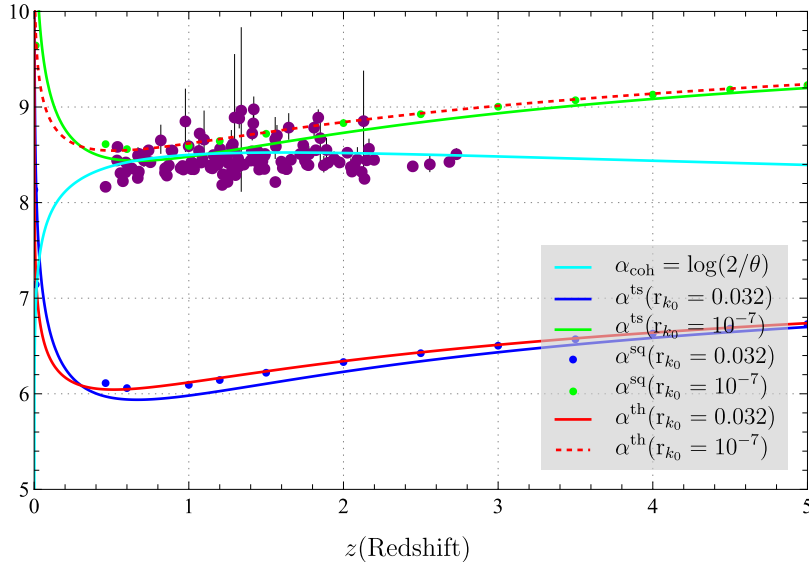


**Figure 9.** Comparison between the incoherence parameters  $\alpha^{\text{ts}}(z)$ ,  $\alpha^{\text{th}}(z)$  and  $\alpha^{\text{sq}}(z)$ , defined by Eqs. (5.8, D.11, D.26). The cyan curve corresponds to the coherence parameter  $\alpha_{\text{coh}}(z)$ . Here,  $\beta = -2, \beta_s = 1$  and  $T_{\text{reh}} = 10^8$  GeV. It can be seen that thermal and squeezed GWs leave a slightly weaker effect on the EM spatial coherence, stemming from the absence of quantum correlations between gravitons. The most stringent upper bound on tensor-to-scalar ratio comes from two-mode squeezed PGWs,  $r_{k_0} \lesssim 10^{-7}$ , while thermal and (one-mode) squeezed GWs lead to  $r_{k_0} \lesssim 10^{-6.8}$ .

## References

- [1] Peter R Saulson. *Fundamentals of interferometric gravitational wave detectors*. World Scientific, 1994.
- [2] Barry C Barish and Rainer Weiss. Ligo and the detection of gravitational waves. *Physics Today*, 52:44–50, 1999.
- [3] Li Ju, DG Blair, and Chunnong Zhao. Detection of gravitational waves. *Reports on Progress in Physics*, 63(9):1317, 2000.
- [4] Thimothée Accadia, F Acernese, M Alshourbagy, P Amico, F Antonucci, S Aoudia, N Arnaud, C Arnault, KG Arun, P Astone, et al. Virgo: a laser interferometer to detect gravitational waves. *Journal of Instrumentation*, 7(03):P03012, 2012.
- [5] David G Blair, Eric J Howell, Li Ju, and Chunnong Zhao. *Advanced gravitational wave detectors*. Cambridge University Press, 2012.
- [6] AAe Abdo, Markus Ackermann, Marco Ajello, K Asano, William B Atwood, Magnus Axelsson, Luca Baldini, Jean Ballet, Guido Barbiellini, Matthew G Baring, et al. A limit on the variation of the speed of light arising from quantum gravity effects. *Nature*, 462(7271):331–334, 2009.

- [7] Fabrizio Tamburini, Carmine Cuofano, Massimo Della Valle, and Roberto Gilmozzi. No quantum gravity signature from the farthest quasars. *Astronomy & Astrophysics*, 533:A71, 2011.
- [8] Luis J Garay. Spacetime foam as a quantum thermal bath. *Physical Review Letters*, 80(12):2508, 1998.
- [9] Achim Kempf. On the three short-distance structures which can be described by linear operators. *Reports on Mathematical Physics*, 43(1-2):171–177, 1999.
- [10] Carlo Rovelli. Loop quantum gravity. *Living reviews in relativity*, 11:1–69, 2008.
- [11] Giovanni Amelino-Camelia. Gravity-wave interferometers as probes of a low-energy effective quantum gravity. *Physical Review D*, 62(2):024015, 2000.
- [12] Richard Lieu and Lloyd W Hillman. The phase coherence of light from extragalactic sources: Direct evidence against first-order planck-scale fluctuations in time and space. *The Astrophysical Journal*, 585(2):L77, 2003.
- [13] Roberto Ragazzoni, Massimo Turatto, and Wolfgang Gaessler. The lack of observational evidence for the quantum structure of spacetime at planck scales. *The Astrophysical Journal*, 587(1):L1, 2003.
- [14] C Lämmerzahl. Interferometry as a universal tool in physics. In *Planck Scale Effects in Astrophysics and Cosmology*, pages 161–198. Springer, 2005.
- [15] Claus Lämmerzahl. The search for quantum gravity effects. *Quantum Gravity: Mathematical Models and Experimental Bounds*, pages 15–39, 2007.
- [16] Mohsen Khodadi, Kouros Nozari, Anha Bhat, and Sina Mohsenian. Probing planck-scale spacetime by cavity opto-atomic rb interferometry. *Progress of Theoretical and Experimental Physics*, 2019(5):053E03, 2019.
- [17] Y Jack Ng, Wayne A Christiansen, and Henrik van Dam. Probing planck-scale physics with extragalactic sources? *The Astrophysical Journal*, 591(2):L87, 2003.
- [18] Leonard Mandel and Emil Wolf. *Optical coherence and quantum optics*. Cambridge university press, 1995.
- [19] DH Coule. Planck scale still safe from stellar images. *Classical and Quantum Gravity*, 20(14):3107, 2003.
- [20] LP Grishchuk. Graviton creation in the early universe. *Annals of the New York Academy of Sciences*, 302(1):439–444, 1977.
- [21] LP Grishchuk. The implications of microwave background anisotropies for laser-interferometer-tested gravitational waves. *Classical and Quantum Gravity*, 14(6):1445, 1997.
- [22] Leonid P Grishchuk. Relic gravitational waves and their detection. In *Gyros, Clocks, Interferometers...: Testing Relativistic Gravity in Space*, pages 167–192. Springer, 2001.
- [23] Leonid P Grishchuk. Discovering relic gravitational waves in cosmic microwave background radiation. *General Relativity and John Archibald Wheeler*, pages 151–199, 2010.
- [24] VA Rubakov, M Verjaskin Sazhin, and AV Veryaskin. Graviton creation in the inflationary universe and the grand unification scale. *Physics Letters B*, 115(3):189–192, 1982.
- [25] R Fabbri and MD Pollock. The effect of primordially produced gravitons upon the anisotropy of the cosmological microwave background radiation. *Physics Letters B*, 125(6):445–448, 1983.
- [26] Laurence F Abbott and Mark B Wise. Constraints on generalized inflationary cosmologies. *Nuclear physics B*, 244(2):541–548, 1984.

- [27] Bruce Allen. Stochastic gravity-wave background in inflationary-universe models. *Physical Review D*, 37(8):2078, 1988.
- [28] Varun Sahni. Energy density of relic gravity waves from inflation. *Physical Review D*, 42(2):453, 1990.
- [29] Hiroyuki Tashiro, Takeshi Chiba, and Misao Sasaki. Reheating after quintessential inflation and gravitational waves. *Classical and Quantum Gravity*, 21(7):1761, 2004.
- [30] Alfredo B Henriques. The stochastic gravitational-wave background and the inflation to radiation transition in the early universe. *Classical and Quantum Gravity*, 21(12):3057, 2004.
- [31] Wen Zhao and Yang Zhang. Relic gravitational waves and their detection. *Physical Review D*, 74(4):043503, 2006.
- [32] Michele Maggiore. Gravitational waves constrained. *Nature*, 447(7145):651–652, 2007.
- [33] <http://www.ligo.caltech.edu/>.
- [34] <http://www.ligo.caltech.edu/advLIGO/>.
- [35] SJ Waldman. The advanced ligo gravitational wave detector. *arXiv preprint arXiv:1103.2728*, 2011.
- [36] <http://www.virgo.infn.it/>.
- [37] Fausto Acernese, Paolo Amico, M Al-Shourbagy, S Aoudia, S Avino, D Babusci, G Ballardín, R Barillé, F Barone, L Barsotti, et al. Status of virgo. *Classical and Quantum Gravity*, 22(18):S869, 2005.
- [38] <http://www.geo600.uni-hannover.de/geocurves/>.
- [39] Benno Willke, Peter Aufmuth, Carsten Aulbert, Stanislav Babak, Ramachandran Balasubramanian, BW Barr, S Berukoff, Sukanta Bose, G Cagnoli, Morag M Casey, et al. The geo 600 gravitational wave detector. *Classical and Quantum Gravity*, 19(7):1377, 2002.
- [40] Jérôme Degallaix, Bram Slagmolen, Chunnong Zhao, Li Ju, and David Blair. Thermal lensing compensation principle for the aciga’s high optical power test facility test 1. *General Relativity and Gravitation*, 37:1581–1589, 2005.
- [41] Pablo Barriga, Chunnong Zhao, and DG Blair. Optical design of a high power mode-cleaner for aigo. *General Relativity and Gravitation*, 37:1609–1619, 2005.
- [42] K Kuroda, on behalf of the LCGT Collaboration, et al. Status of lcgt. *Classical and Quantum Gravity*, 27(8):084004, 2010.
- [43] M Punturo, M Abernathy, F Acernese, B Allen, Nils Andersson, K Arun, F Barone, B Barr, M Barsuglia, M Beker, et al. The einstein telescope: a third-generation gravitational wave observatory. *Classical and Quantum Gravity*, 27(19):194002, 2010.
- [44] S Hild, M Abernathy, F ea Acernese, P Amaro-Seoane, N Andersson, K Arun, F Barone, B Barr, M Barsuglia, M Beker, et al. Sensitivity studies for third-generation gravitational wave observatories. *Classical and Quantum gravity*, 28(9):094013, 2011.
- [45] Shane L Larson, William A Hiscock, and Ronald W Hellings. Sensitivity curves for spaceborne gravitational wave interferometers. *Physical Review D*, 62(6):062001, 2000.
- [46] Shane L Larson, Ronald W Hellings, and William A Hiscock. Unequal arm space-borne gravitational wave detectors. *Physical Review D*, 66(6):062001, 2002.
- [47] Jeff Crowder and Neil J Cornish. Beyond lisa: Exploring future gravitational wave missions. *Physical Review D*, 72(8):083005, 2005.
- [48] Neil J Cornish and Jeff Crowder. Lisa data analysis using markov chain monte carlo methods. *Physical Review D*, 72(4):043005, 2005.



- [49] Curt Cutler and Jan Harms. Big bang observer and the neutron-star-binary subtraction problem. *Physical Review D*, 73(4):042001, 2006.
- [50] Seiji Kawamura, Takashi Nakamura, Masaki Ando, Naoki Seto, Kimio Tsubono, Kenji Numata, Ryuichi Takahashi, Shigeo Nagano, Takehiko Ishikawa, Mitsuru Musha, et al. The japanese space gravitational wave antenna—decigo. *Classical and Quantum Gravity*, 23(8):S125, 2006.
- [51] Hideaki Kudoh, Atsushi Taruya, Takashi Hiramatsu, and Yoshiaki Himemoto. Detecting a gravitational-wave background with next-generation space interferometers. *Physical Review D*, 73(6):064006, 2006.
- [52] G Hobbs. Gravitational wave detection using high precision pulsar observations. *Classical and Quantum Gravity*, 25(11):114032, 2008.
- [53] RN Manchester. The parkes pulsar timing array. *Chinese Journal of Astronomy and Astrophysics*, 6(S2):139, 2006.
- [54] Frederick A Jenet, George B Hobbs, W Van Straten, Richard N Manchester, Matthew Bailes, JPW Verbiest, Russell T Edwards, Aidan W Hotan, John M Sarkissian, and Stephen M Ord. Upper bounds on the low-frequency stochastic gravitational wave background from pulsar timing observations: Current limits and future prospects. *The Astrophysical Journal*, 653(2):1571, 2006.
- [55] Michael Kramer, DC Backer, JM Cordes, TJW Lazio, BW Stappers, and S Johnston. Strong-field tests of gravity using pulsars and black holes. *New Astronomy Reviews*, 48(11-12):993–1002, 2004.
- [56] AM Cruise. An electromagnetic detector for very-high-frequency gravitational waves. *Classical and Quantum Gravity*, 17(13):2525, 2000.
- [57] AM Cruise and Richard MJ Ingle. A correlation detector for very high frequency gravitational waves. *Classical and Quantum Gravity*, 22(10):S479, 2005.
- [58] AM Cruise and RMJ Ingle. A prototype gravitational wave detector for 100 mhz. *Classical and Quantum Gravity*, 23(22):6185, 2006.
- [59] Ming-Lei Tong and Yang Zhang. Detecting very-high-frequency relic gravitational waves by a waveguide. *Chinese Journal of Astronomy and Astrophysics*, 8(3):314, 2008.
- [60] Fang-Yu Li, Meng-Xi Tang, and Dong-Ping Shi. Electromagnetic response of a gaussian beam to high-frequency relic gravitational waves in quintessential inflationary models. *Physical Review D*, 67(10):104008, 2003.
- [61] Fangyu Li, Robert ML Baker Jr, Zhenyun Fang, Gary V Stephenson, and Zhenya Chen. Perturbative photon fluxes generated by high-frequency gravitational waves and their physical effects. *The European Physical Journal C*, 56:407–423, 2008.
- [62] ML Tong, Yang Zhang, and Fang-Yu Li. Using a polarized maser to detect high-frequency relic gravitational waves. *Physical Review D*, 78(2):024041, 2008.
- [63] Tomotada Akutsu, Seiji Kawamura, Atsushi Nishizawa, Koji Arai, Kazuhiro Yamamoto, Daisuke Tatsumi, Shigeo Nagano, Erina Nishida, Takeshi Chiba, Ryuichi Takahashi, et al. Search for a stochastic background of 100-mhz gravitational waves with laser interferometers. *Physical review letters*, 101(10):101101, 2008.
- [64] Matias Zaldarriaga and Uroš Seljak. All-sky analysis of polarization in the microwave background. *Physical Review D*, 55(4):1830, 1997.
- [65] Marc Kamionkowski, Arthur Kosowsky, and Albert Stebbins. Statistics of cosmic microwave background polarization. *Physical Review D*, 55(12):7368, 1997.

- [66] Brian Keating, Peter Timbie, Alexander Polnarev, and Julia Steinberger. Large angular scale polarization of the cosmic microwave background radiation and the feasibility of its detection. *The Astrophysical Journal*, 495(2):580, 1998.
- [67] Jonathan R Pritchard and Marc Kamionkowski. Cosmic microwave background fluctuations from gravitational waves: An analytic approach. *Annals of Physics*, 318(1):2–36, 2005.
- [68] Wen Zhao and Yang Zhang. Analytic approach to the cmb polarization generated by relic gravitational waves. *Physical Review D*, 74(8):083006, 2006.
- [69] TY Xia and Y Zhang. Approximate analytic spectra of reionized cmb anisotropies and polarization generated by relic gravitational waves. *Physical Review D*, 79(8):083002, 2009.
- [70] W Zhao and D Baskaran. Detecting relic gravitational waves in the cmb: Optimal parameters and their constraints. *Physical Review D*, 79(8):083003, 2009.
- [71] Neil Bevis, Mark Hindmarsh, Martin Kunz, and Jon Urrestilla. Fitting cosmic microwave background data with cosmic strings and inflation. *Physical Review Letters*, 100(2):021301, 2008.
- [72] Eiichiro Komatsu, J Dunkley, MR Nolta, CL Bennett, B Gold, G Hinshaw, N Jarosik, D Larson, M Limon, L Page, et al. Five-year wilkinson microwave anisotropy probe\* observations: cosmological interpretation. *The Astrophysical Journal Supplement Series*, 180(2):330, 2009.
- [73] J Dunkley, Eiichiro Komatsu, MR Nolta, DN Spergel, D Larson, G Hinshaw, L Page, CL Bennett, B Gold, N Jarosik, et al. Five-year wilkinson microwave anisotropy probe\* observations: Likelihoods and parameters from the wmap data. *The Astrophysical Journal Supplement Series*, 180(2):306, 2009.
- [74] N Jarosik, CL Bennett, J Dunkley, B Gold, MR Greason, M Halpern, RS Hill, G Hinshaw, A Kogut, Eiichiro Komatsu, et al. Seven-year wilkinson microwave anisotropy probe (wmap\*) observations: sky maps, systematic errors, and basic results. *The Astrophysical Journal Supplement Series*, 192(2):14, 2011.
- [75] Gary Hinshaw, D Larson, Eiichiro Komatsu, David N Spergel, CLaa Bennett, Joanna Dunkley, MR Nolta, M Halpern, RS Hill, N Odegard, et al. Nine-year wilkinson microwave anisotropy probe (wmap) observations: cosmological parameter results. *The Astrophysical Journal Supplement Series*, 208(2):19, 2013.
- [76] Planck Collaboration et al. The scientific programme of planck. *arXiv preprint astro-ph/0604069*, 2006.
- [77] <http://www.rssd.esa.int/index.php?project=Planck>.
- [78] A Suzuki, Peter AR Ade, Yoshiki Akiba, D Alonso, K Arnold, J Aumont, C Baccigalupi, D Barron, S Basak, S Beckman, et al. The litebird satellite mission: Sub-kelvin instrument. *Journal of Low Temperature Physics*, 193(5):1048–1056, 2018.
- [79] Michael D Niemack, Peter AR Ade, J Aguirre, F Barrientos, JA Beall, JR Bond, J Britton, HM Cho, S Das, MJ Devlin, et al. Actpol: a polarization-sensitive receiver for the atacama cosmology telescope. In *Millimeter, Submillimeter, and Far-Infrared Detectors and Instrumentation for Astronomy V*, volume 7741, pages 537–557. SPIE, 2010.
- [80] J Dunkley, A Amblard, C Baccigalupi, M Betoule, D Chuss, A Cooray, J Delabrouille, C Dickinson, G Dobler, J Dotson, et al. Prospects for polarized foreground removal. In *AIP Conference Proceedings*, volume 1141, pages 222–264. American Institute of Physics, 2009.
- [81] Marshall Harris Cohen. Introduction to very-long-baseline interferometry. *Proceedings of the IEEE*, 61(9):1192–1197, 1973.
- [82] Heino Falcke, Neil M Nagar, Andrew S Wilson, and James S Ulvestad. Radio sources in low-luminosity active galactic nuclei. ii. very long baseline interferometry detections of

compact radio cores and jets in a sample of liners. *The Astrophysical Journal*, 542(1):197, 2000.

- [83] AB Pushkarev and YY Kovalev. Milky way scattering properties and intrinsic sizes of active galactic nuclei cores probed by very long baseline interferometry surveys of compact extragalactic radio sources. *Monthly Notices of the Royal Astronomical Society*, 452(4):4274–4282, 2015.
- [84] T An, BW Sohn, and H Imai. Capabilities and prospects of the east asia very long baseline interferometry network. *Nature Astronomy*, 2(2):118–125, 2018.
- [85] JC Algaba. High-frequency very long baseline interferometry rotation measure of eight active galactic nuclei. *Monthly Notices of the Royal Astronomical Society*, 429(4):3551–3563, 2013.
- [86] Freek Roelofs, Christian M Fromm, Yosuke Mizuno, Jordy Davelaar, Michael Janssen, Ziri Younsi, Luciano Rezzolla, and Heino Falcke. Black hole parameter estimation with synthetic very long baseline interferometry data from the ground and from space. *Astronomy & Astrophysics*, 650:A56, 2021.
- [87] Raúl Carballo-Rubio, Vitor Cardoso, and Ziri Younsi. Toward very large baseline interferometry observations of black hole structure. *Physical Review D*, 106(8):084038, 2022.
- [88] DW Pesce, JA Braatz, MJ Reid, AG Riess, D Scolnic, JJ Condon, F Gao, C Henkel, CMV Impellizzeri, CY Kuo, et al. The megamaser cosmology project. xiii. combined hubble constant constraints. *The Astrophysical Journal Letters*, 891(1):L1, 2020.
- [89] CY Kuo, James A Braatz, Mark J Reid, KY Lo, James J Condon, Caterina MV Impellizzeri, and Christian Henkel. The megamaser cosmology project. v. an angular-diameter distance to ngc 6264 at 140 mpc. *The Astrophysical Journal*, 767(2):155, 2013.
- [90] Shuo Cao, Xiaogang Zheng, Marek Biesiada, Jingzhao Qi, Yun Chen, and Zong-Hong Zhu. Ultra-compact structure in intermediate-luminosity radio quasars: building a sample of standard cosmological rulers and improving the dark energy constraints up to  $z \sim 3$ . *Astronomy & Astrophysics*, 606:A15, 2017.
- [91] Tonghua Liu, Ziqiang Liu, Jiamin Wang, Shengnan Gong, Man Li, and Shuo Cao. Revisiting friedmann-like cosmology with torsion: newest constraints from high-redshift observations. *arXiv preprint arXiv:2304.06425*, 2023.
- [92] Tonghua Liu, Shuo Cao, Marek Biesiada, Yilong Zhang, and Jieci Wang. Model-independent way to determine the hubble constant and the curvature from the phase shift of gravitational waves with decigo. *The Astrophysical Journal Letters*, 965(1):L11, 2024.
- [93] IH Park, K-Y Choi, J Hwang, S Jung, DH Kim, MH Kim, C-H Lee, KH Lee, SH Oh, M-G Park, et al. Stellar interferometry for gravitational waves. *Journal of Cosmology and Astroparticle Physics*, 2021(11):008, 2021.
- [94] Michalis Lagouvardos and Charis Anastopoulos. Gravitational decoherence of photons. *Classical and Quantum Gravity*, 38(11):115012, 2021.
- [95] Fateme SHOJAEI ARANI, Malek Bagheri Harouni, Brahim Lamine, and Alain Blanchard. Sensing quantum nature of primordial gravitational waves using electromagnetic probes. *Physica Scripta*, 2023.
- [96] Brahim Lamine, Rémy Hervé, Astrid Lambrecht, and Serge Reynaud. Ultimate decoherence border for matter-wave interferometry. *Physical review letters*, 96(5):050405, 2006.
- [97] Sugumi Kanno, Jiro Soda, and Junsei Tokuda. Noise and decoherence induced by gravitons. *Physical Review D*, 103(4):044017, 2021.
- [98] Ming-Lei Tong, Yang Zhang, Wen Zhao, Jin-Zhong Liu, Cheng-Shi Zhao, and Ting-Gao Yang. Using pulsar timing arrays and the quantum normalization condition to constrain relic gravitational waves. *Classical and Quantum Gravity*, 31(3):035001, 2013.

- [99] Minglei Tong. Revisit relic gravitational waves based on the latest cmb observations. *Classical and Quantum Gravity*, 29(15):155006, 2012.
- [100] Y Zhang, ML Tong, and ZW Fu. Constraints upon the spectral indices of relic gravitational waves by ligo s5. *Physical Review D*, 81(10):101501, 2010.
- [101] Ming-Lei Tong and Yang Zhang. Relic gravitational waves with a running spectral index and its constraints at high frequencies. *Physical Review D*, 80(8):084022, 2009.
- [102] Yashar Akrami, Frederico Arroja, M Ashdown, J Aumont, Carlo Baccigalupi, M Ballardini, Anthony J Banday, RB Barreiro, Nicola Bartolo, S Basak, et al. Planck 2018 results-x. constraints on inflation. *Astronomy & Astrophysics*, 641:A10, 2020.
- [103] Alexei A Starobinsky. A new type of isotropic cosmological models without singularity. *Physics Letters B*, 91(1):99–102, 1980.
- [104] HX Miao and Yang Zhang. Analytic spectrum of relic gravitational waves modified by neutrino free streaming and dark energy. *Physical Review D*, 75(10):104009, 2007.
- [105] Planck Collaboration, N Aghanim, Y Akrami, MIR Alves, M Ashdown, J Aumont, C Baccigalupi, M Ballardini, AJ Banday, RB Barreiro, et al. Planck 2018 results. *A&A*, 641:A12, 2020.
- [106] Jerome Martin and Christophe Ringeval. First cmb constraints on the inflationary reheating temperature. *Physical Review D*, 82(2):023511, 2010.
- [107] Sean Bailly, Ki-Young Choi, Karsten Jedamzik, and Leszek Roszkowski. A re-analysis of gravitino dark matter in the constrained mssm. *Journal of High Energy Physics*, 2009(05):103, 2009.
- [108] Minglei Tong. Relic gravitational waves in the frame of slow-roll inflation with a power-law potential, and their detection. *Classical and Quantum Gravity*, 30(5):055013, 2013.
- [109] LP Grishchuk. Quantum effects in cosmology. *Classical and Quantum Gravity*, 10(12):2449, 1993.
- [110] Jérôme Martin and Vincent Vennin. Quantum discord of cosmic inflation: Can we show that cmb anisotropies are of quantum-mechanical origin? *Physical Review D*, 93(2):023505, 2016.
- [111] Viatcheslav F Mukhanov. *Physical foundations of cosmology*. Cambridge university press, 2005.
- [112] Yang Zhang, XinZhong Er, TianYang Xia, Wen Zhao, and HaiXing Miao. An exact analytic spectrum of relic gravitational waves in an accelerating universe. *Classical and Quantum Gravity*, 23(11):3783, 2006.
- [113] Ling-An Wu, HJ Kimble, JL Hall, and Huifa Wu. Generation of squeezed states by parametric down conversion. *Physical review letters*, 57(20):2520, 1986.
- [114] Girish S Agarwal. *Quantum optics*. Cambridge University Press, 2012.
- [115] Jérôme Martin, Amaury Micheli, and Vincent Vennin. Discord and decoherence. *Journal of Cosmology and Astroparticle Physics*, 2022(04):051, 2022.
- [116] Yang Zhang, Yefei Yuan, Wen Zhao, and Ying-Tian Chen. Relic gravitational waves in the accelerating universe. *Classical and Quantum Gravity*, 22(7):1383, 2005.
- [117] Nabila Aghanim, Yashar Akrami, Mark Ashdown, J Aumont, C Baccigalupi, M Ballardini, AJ Banday, RB Barreiro, N Bartolo, S Basak, et al. Planck 2018 results-vi. cosmological parameters. *Astronomy & Astrophysics*, 641:A6, 2020.
- [118] Francesco Coradeschi, Antonia Micol Frassino, Thiago Guerreiro, Jennifer Rittenhouse West, and Enrico Junior Schioppa. Can we detect the quantum nature of weak gravitational fields? *Universe*, 7(11):414, 2021.

- [119] C Anastopoulos and BL Hu. A master equation for gravitational decoherence: probing the textures of spacetime. *Classical and Quantum Gravity*, 30(16):165007, 2013.
- [120] Luca Abrahao, Francesco Coradeschi, Antonia Micol Frassino, Thiago Guerreiro, Jennifer Rittenhouse West, and Enrico Junior Schioppa. The quantum optics of gravitational waves. *Classical and Quantum Gravity*, 41(1):015029, 2023.
- [121] Markus Aspelmeyer, Tobias J Kippenberg, and Florian Marquardt. Cavity optomechanics. *Reviews of Modern Physics*, 86(4):1391, 2014.
- [122] S Bose, K Jacobs, and PL Knight. Preparation of nonclassical states in cavities with a moving mirror. *Physical Review A*, 56(5):4175, 1997.
- [123] Thiago Guerreiro. Quantum effects in gravity waves. *Classical and Quantum Gravity*, 37(15):155001, 2020.
- [124] Liju Philip. Calibration and wide field imaging with paper: a catalogue of compact sources. 2016.
- [125] Marlan O Scully and M Suhail Zubairy. Quantum optics, 1999.
- [126] Tonghua Liu, Xiyan Yang, Zisheng Zhang, Jieci Wang, and Marek Biesiada. Measurements of the hubble constant from combinations of supernovae and radio quasars. *Physics Letters B*, 845:138166, 2023.
- [127] Tonghua Liu, Shuo Cao, Shuai Ma, Yuting Liu, Chenfa Zheng, and Jieci Wang. What are recent observations telling us in light of improved tests of distance duality relation? *Physics Letters B*, 838:137687, 2023.
- [128] Matthieu Tristram, Anthony J Banday, Krzysztof M Górski, Reijo Keskitalo, CR Lawrence, Kristian Joten Andersen, R Belén Barreiro, J Borrill, LPL Colombo, HK Eriksen, et al. Improved limits on the tensor-to-scalar ratio using bicep and p l a n c k data. *Physical Review D*, 105(8):083524, 2022.
- [129] J Antoniadis, P Arumugam, S Arumugam, S Babak, M Bagchi, A-S Bak Nielsen, CG Bassa, A Bathula, A Berthereau, M Bonetti, et al. The second data release from the european pulsar timing array-iv. implications for massive black holes, dark matter, and the early universe. *Astronomy & Astrophysics*, 685:A94, 2024.
- [130] Jerome Martin, Christophe Ringeval, and Vincent Vennin. How well can future cmb missions constrain cosmic inflation? *Journal of Cosmology and Astroparticle Physics*, 2014(10):038, 2014.
- [131] CP Burgess, R Holman, Greg Kaplanek, Jérôme Martin, and Vincent Vennin. Minimal decoherence from inflation. *Journal of Cosmology and Astroparticle Physics*, 2023(07):022, 2023.
- [132] DJ Fixsen. The temperature of the cosmic microwave background. *The Astrophysical Journal*, 707(2):916, 2009.
- [133] Yuki Watanabe and Eiichiro Komatsu. Improved calculation of the primordial gravitational wave spectrum in the standard model. *Physical Review D*, 73(12):123515, 2006.
- [134] Charles W Misner, Kip S Thorne, and John Archibald Wheeler. *Gravitation*. Macmillan, 1973.